



MINISTÉRIO DA CIÊNCIA, TECNOLOGIA E INOVAÇÃO
INSTITUTO NACIONAL DE PESQUISAS ESPACIAIS

sid.inpe.br/mtc-m21b/2016/07.01.14.30-TDI

**UNCERTAINTY EVALUATION FOR IN-FLIGHT
RADIOMETRIC CALIBRATION OF EARTH
OBSERVATION SENSORS**

Cibele Teixeira Pinto

Doctorate Thesis Course Graduate
in Remote Sensing, guided by Drs.
Flávio Jorge Ponzoni, and Ruy
Morgado de Castro, approved in
july 07, 2016.

URL of the original document:

<<http://urlib.net/8JMKD3MGP3W34P/3M2724B>>

INPE
São José dos Campos
2016

PUBLISHED BY:

Instituto Nacional de Pesquisas Espaciais - INPE

Gabinete do Diretor (GB)

Serviço de Informação e Documentação (SID)

Caixa Postal 515 - CEP 12.245-970

São José dos Campos - SP - Brasil

Tel.:(012) 3208-6923/6921

Fax: (012) 3208-6919

E-mail: pubtc@inpe.br

**COMMISSION OF BOARD OF PUBLISHING AND PRESERVATION
OF INPE INTELLECTUAL PRODUCTION (DE/DIR-544):****Chairperson:**

Maria do Carmo de Andrade Nono - Conselho de Pós-Graduação (CPG)

Members:

Dr. Plínio Carlos Alvalá - Centro de Ciência do Sistema Terrestre (CST)

Dr. André de Castro Milone - Coordenação de Ciências Espaciais e Atmosféricas (CEA)

Dra. Carina de Barros Melo - Coordenação de Laboratórios Associados (CTE)

Dr. Evandro Marconi Rocco - Coordenação de Engenharia e Tecnologia Espacial (ETE)

Dr. Hermann Johann Heinrich Kux - Coordenação de Observação da Terra (OBT)

Dr. Marley Cavalcante de Lima Moscati - Centro de Previsão de Tempo e Estudos Climáticos (CPT)

Silvia Castro Marcelino - Serviço de Informação e Documentação (SID) **DIGITAL**

LIBRARY:

Dr. Gerald Jean Francis Banon

Clayton Martins Pereira - Serviço de Informação e Documentação (SID)

DOCUMENT REVIEW:

Simone Angélica Del Duca Barbedo - Serviço de Informação e Documentação (SID)

Yolanda Ribeiro da Silva Souza - Serviço de Informação e Documentação (SID)

ELECTRONIC EDITING:

Marcelo de Castro Pazos - Serviço de Informação e Documentação (SID)

André Luis Dias Fernandes - Serviço de Informação e Documentação (SID)



MINISTÉRIO DA CIÊNCIA, TECNOLOGIA E INOVAÇÃO
INSTITUTO NACIONAL DE PESQUISAS ESPACIAIS

sid.inpe.br/mtc-m21b/2016/07.01.14.30-TDI

**UNCERTAINTY EVALUATION FOR IN-FLIGHT
RADIOMETRIC CALIBRATION OF EARTH
OBSERVATION SENSORS**

Cibele Teixeira Pinto

Doctorate Thesis Course Graduate
in Remote Sensing, guided by Drs.
Flávio Jorge Ponzoni, and Ruy
Morgado de Castro, approved in
july 07, 2016.

URL of the original document:

<<http://urlib.net/8JMKD3MGP3W34P/3M2724B>>

INPE
São José dos Campos
2016

Cataloging in Publication Data

Pinto, Cibele Teixeira.

P658u Uncertainty evaluation for in-flight radiometric calibration of earth observation sensors / Cibele Teixeira Pinto. – São José dos Campos : INPE, 2016.
xxvi + 135 p. ; (sid.inpe.br/mtc-m21b/2016/07.01.14.30-TDI)

Thesis (Doctorate in Remote Sensing) – Instituto Nacional de Pesquisas Espaciais, São José dos Campos, 2016.

Guiding : Drs. Flávio Jorge Ponzoni, and Ruy Morgado de Castro.

1. Radiometric calibration. 2. Uncertainties. 3. Reflectance-based approach. 4. Cross calibration. 5. Orbital sensor. I.Title.

CDU 528.711.7:520.8.07



Esta obra foi licenciada sob uma Licença [Creative Commons Atribuição-NãoComercial 3.0 Não Adaptada](https://creativecommons.org/licenses/by-nc/3.0/).

This work is licensed under a [Creative Commons Attribution-NonCommercial 3.0 Unported License](https://creativecommons.org/licenses/by-nc/3.0/).

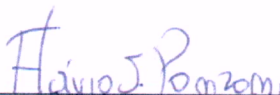
Aluno (a): **Cibele Teixeira Pinto**

Título: "UNCERTAINTY EVALUATION FOR IN FLIGHT RADIOMETRIC CALIBRATION OF EARTH OBSERVATION SENSORS".

Aprovado (a) pela Banca Examinadora em cumprimento ao requisito exigido para obtenção do Título de **Doutor(a)** em

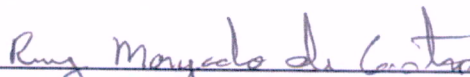
Sensoriamento Remoto

Dr. Flávio Jorge Ponzoni



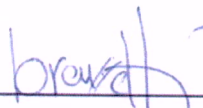
Presidente / Orientador(a) / INPE / SJCampos - SP

Dr. Ruy Morgado de Castro



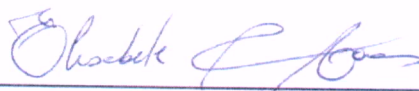
Orientador(a) / IEAv/CTA / São José dos Campos - SP

Dr. João Antonio Lorenzetti



Membro da Banca / INPE / SJCampos - SP

Dra. Elisabete Caria Moraes



Membro da Banca / INPE / SJCampos - SP

Dr. Vito Roberto Vanin



Convidado(a) / USP / São Paulo - SP

Dr. Romero da Costa Moreira



Convidado(a) / ITA / São José dos Campos - SP

Este trabalho foi aprovado por:

maioria simples

unanimidade

São José dos Campos, 07 de Julho de 2016

“Quem nunca cometeu um erro, nunca tentou algo novo.”

Albert Einstein

“Love all, trust a few, do wrong to none.”

William Shakespeare

*Dedico a meu marido, Pedro Valle,
a minha mãe, Dulce Valda e
minhas irmãs, Caroline e Cássia.*

AGRADECIMENTOS

Aos meus orientadores, Dr. Flávio Jorge Ponzoni e Dr. Ruy Morgado de Castro, pela dedicação, motivação, orientação, apoio e ensinamentos compartilhados durante o doutorado.

Agradeço ao Programa de Pós-Graduação do Instituto Nacional de Pesquisas Espaciais (INPE) e todos os professores pela oportunidade do doutorado e aprendizado valioso.

À Coordenação de Aperfeiçoamento de Pessoal de Nível Superior (CAPES), pelo auxílio financeiro.

Ao Conselho Nacional de Desenvolvimento Científico e Tecnológico (CNPQ) pela concessão de bolsa para realização do estágio nos Estados Unidos.

Ao Instituto de Estudos Avançados (IEAv), pela utilização do Laboratório de Radiometria e Caracterização de Sensores Eletro-ópticos (LaRaC).

À Sulimar Munira pela ajuda no trabalho de campo realizado no Brasil.

Agradezco a los investigadores Cristian Mattar y Andrés Santamaría Artigas de la Universidad de Chile, y Carolina Barrientos del Servicio Aerofotogramétrico de la Fuerza Aérea de Chile (SAF) por la asociación, que ha posibilitado la realización del trabajo de campo en el Desierto de Atacama en Chile.

I thank Dr. Dennis Helder for the opportunity to stay in a one year training period as a Ph.D. Visiting Research Scholar in South Dakota State University Image Processing Laboratory (SDSU IP Lab).

I thank all SDSU IP Lab researchers: David Aaron, Morakot Kaewmanee, Nischal Mishra and Larry Leigh. Special thanks to Larry for invaluable MODTRAN education.

A meu marido Pedro Valle, pelo amor, incentivo e extrema paciência, principalmente nos momentos finais do desenvolvimento deste trabalho.

A toda minha família, em especial a minha mãe, Dulce Valda, e minhas irmãs Caroline e Cássia.

ABSTRACT

The absolute radiometric calibration is a prerequisite for creating high-quality science data, and consequently, higher-level Earth observation sensors products. The radiometric calibration uncertainty is the key that describes the reliability of calibration results. The main objective of this present work was to develop a method to evaluate the uncertainties inherent in the in-flight absolute radiometric calibration of Earth observation sensors. The methodology developed and tested confirms the hypothesis that the method proposed here is compatible and comparable with other methods practiced by the international science community of satellite radiometric calibration. The uncertainties were determined for two methods of absolute radiometric calibration: reflectance-based approach and cross-calibration method. The reflectance-based approach was performed using four different reference surfaces: (a) west part of the Bahia State, Brazil; (b) Atacama Desert, Chile; (c) Algodones Dunes, USA; and (d) South Dakota State University (SDSU) site, USA. Regarding the reflectance-based approach, the main sources of uncertainty are: (a) the instruments used for the reference surface characterization; (b) atmosphere characterization parameters; (c) surface reflectance factor; and (d) radiative transfer code (MODTRAN). The spectroradiometer instrumental uncertainties in laboratory were lower than 1%. The reference panel relative uncertainties were less than 0.25%. The columnar water vapor was derived from the spectral band of the solar photometer centered on 940 nm with an uncertainty lower than 5%. The aerosol optical depth relative uncertainties ranged from 2-12% in Brazil, 1-5% in Chile, 1-11% in Algodones Dunes and less than 1.2% in SDSU site. The most important information related to the reflectance-based method is the retrieved surface reflectance factor at the time of sensor overpass the site measured in field. The relative uncertainty of the Algodones Dunes and Atacama Desert reflectance factor was lower than 5%; and the relative uncertainty of Brazil and SDSU reflectance factor ranged from 3% to 10%. The second major source of uncertainty was the accuracy of MODTRAN (2%). The final uncertainty of the TOA radiance predicted by MODTRAN in Brazil and in SDSU site was lower than 10%. The final uncertainty of the TOA radiance predicted by MODTRAN in Atacama Desert and in Algodones Dunes site was lower than 5.5%. These values are the overall total uncertainty of the reflectance-based method in the spectral range of 350 to 2400 nm. The cross-calibration between both MUX and WFI on-board CBERS-4 and the OLI on-board Landsat-8 was performed using the Libya-4 and Atacama Desert sites. During the cross-calibration it is necessary to correct the intrinsic offsets between two sensors caused by Spectral Response Function (SRF) mismatches using a spectral band adjustment factor (SBAF). Thus, one of the sources of uncertainty in the cross-calibration is the SBAF, which depend on the uncertainty of the target spectral profile and the SRF uncertainty of the two sensors. Here, the SBAF was estimated with an uncertainty lower than 2%. The overall total uncertainty achieved here with cross-calibration method using the Libya-4 and Atacama Desert sites was less than 6.5%. The dominant source of uncertainty in cross-calibration is the uncertainty associated with the sensor selected as reference. The OLI produces data calibrated to an uncertainty of less than 5% in terms of radiance. Brazil now has a quantitative indication of the quality of the absolute calibration final results. In addition, the country

now has autonomy and reliability in the data provided by sensors of national Earth observation program.

Keywords: Radiometric Calibration. Uncertainties. Reflectance-based approach. Cross-Calibration. Orbital Sensor.

AVALIAÇÃO DA INCERTEZA NA CALIBRAÇÃO RADIOMÉTRICA DE SENSORES DE OBSERVAÇÃO DA TERRA

RESUMO

A capacidade de detectar e quantificar as mudanças na superfície terrestre utilizando dados de sensoriamento remoto depende de sensores de observação da Terra que forneçam medições precisas e consistentes ao longo do tempo. Uma etapa essencial para garantir esta qualidade e consistência nos dados é a realização da calibração radiométrica absoluta, cuja confiabilidade é quantificada por meio do cálculo das incertezas envolvidas no processo. O objetivo principal deste trabalho é apresentar um método para avaliar as incertezas inerentes às missões de calibração radiométrica absoluta de sensores de observação da Terra após seu lançamento. A metodologia desenvolvida e testada confirma a hipótese de que o método proposto é compatível e comparável com outros métodos praticados pela comunidade científica internacional de calibração radiométrica de sensores abordo de satélite. As incertezas foram determinadas para dois métodos de calibração radiométrica absoluta: *reflectance-based* e calibração cruzada. O método *reflectance-based* foi realizado em quatro superfícies de referência distintas: (a) oeste do estado da Bahia, Brasil; (b) Deserto do Atacama, Chile; (c) Algodones Dunes, EUA; e (d) South Dakota State University (SDSU), EUA. As principais fontes de incerteza relacionadas ao método *reflectance-based* são: (a) os instrumentos utilizados para a caracterização da superfície de referência; (b) os parâmetros de caracterização da atmosfera; (c) o fator de reflectância da superfície; e (d) o modelo de transferência radiativa (MODTRAN). As incertezas instrumentais relacionadas ao espectrorradiômetro foram menores que 1%. As incertezas da placa de referência foram menores que 0,25%. O conteúdo de vapor d'água foi derivado da banda espectral do fotômetro solar centralizada em 940 nm com uma incerteza menor que 5%. A incerteza relativa da profundidade óptica do aerossol variou entre 2 e 12% no Brasil, 1 a 5% no Chile, 1 a 11% em Algodones Dunes e foi menor que 1,2 % na SDSU. A informação de maior importância do método *reflectance-based* é o fator de reflectância da superfície medido no momento em que o sensor sobrevoou a superfície em campo. A incerteza relativa do fator de reflectância de Algodones Dunes e do Deserto do Atacama foi menor que 5% enquanto do Brasil e na SDSU variou entre 3 e 10%. A segunda maior fonte de incerteza se referiu à precisão do MODTRAN (2%). A incerteza final da radiância no topo da atmosfera estimada pelo MODTRAN no Brasil e na SDSU foi menor que 10%. A incerteza final da radiância no topo da atmosfera estimada pelo MODTRAN no Deserto do Atacama e em Algodones Dunes foi menor que 5,5%. Esses valores correspondem à incerteza total global do método *reflectance-based* para a região espectral entre 350 e 2400 nm. A calibração cruzada dos sensores MUX e WFI a bordo do CBERS-4 com o sensor OLI a bordo do Landsat-8 foi realizada utilizando duas áreas distintas: Libya-4 e o Deserto do Atacama. Durante o processo de calibração cruzada é necessário corrigir as diferenças das funções de resposta espectral (SRF) dos dois sensores envolvidos. Essa correção é realizada mediante aplicação do fator de ajuste de banda espectral (SBAF). Assim, uma das fontes de incertezas no processo de calibração cruzada é o próprio SBAF, no qual depende da incerteza do perfil espectral do alvo e da incerteza da SRF dos dois sensores (sensor de referência e sensor a ser calibrado). Neste trabalho, o SBAF foi estimado

com uma incerteza menor que 2%. A incerteza total global no método de calibração cruzada utilizando o Deserto do Atacama e a Líbya-4 foi menor que 6,5%. A fonte de incerteza dominante na calibração cruzada é a incerteza associada ao sensor selecionado como referência. O sensor OLI produz dados calibrados de radiância com uma incerteza menor que 5%. O Brasil agora possui uma indicação quantitativa da qualidade do resultado final da calibração radiométrica absoluta. Além disso, o país também passa a possuir autonomia e confiabilidade nos dados disponibilizados por sensores do programa nacional de observação da Terra, como por exemplo, o CBERS-4.

Keywords: Calibração Radiométrica. Incertezas. *Reflectance-based*. Calibração Cruzada. Sensor Orbital.

LIST OF FIGURES

Figure 2.1. Illustrative scheme of reflectance-based approach procedures	9
Figure 2.2. Illustrative scheme of cross-calibration method procedures	18
Figure 2.3. Multispectral Camera (MUX), Wide-Field Imager (WFI) and Operational Land Imager (OLI) Spectral Response Function (SRF).....	19
Figure 2.4. Factors that influence the measurement process	22
Figure 2.5. The propagation and summarizing stages of uncertainty evaluation using Monte Carlo method to implement the propagation of distributions	28
Figure 2.6. In (a) the line fitted to the experimental points is implausible because it is inconsistent with the points and their uncertainties. In (b) the parabola fitted to the experimental points is quite feasible, which means that the quality of fit is good. In (c) the good agreement between the line fitted and the experimental points is improbable as it is incompatible with the uncertainties so great.....	32
Figure 3.1. General work flowchart.....	34
Figure 3.2. A summary of in situ results from the University of Arizona (UA), South Dakota State University (SDSU), and Goddard Space Flight Center (GSFC) for TOA spectral radiance (top left) and reflectance (top right) for OLI/Landsat-8	36
Figure 3.3. Reflectance-based approach flowchart	39
Figure 3.4. In (a) Location of the study area in Brazil; and (b) picture of the reference surface	40
Figure 3.5. In (a) Location of the study area in Chile (Atacama Desert); and (b) picture of the reference surface	42
Figure 3.6. In (a) Location of the Algodones Dunes; and (b) picture of the reference surface	43
Figure 3.7. In (a) Location of the SDSU site; and (b) picture of the reference surface.	44
Figure 3.8. Overview of the experimental setup to characterize and assess the spectroradiometer. In (a) the FieldSpec Pro ASD used in fieldwork; and (b) the FieldSpec Pro ASD belonging to the LaRaC laboratory, which remains all the time in the laboratory, therefore, is an instrument considered as a reference.....	47
Figure 3.9. Spectral reflectance of the standard panel from LaRaC.....	49
Figure 3.10. Overview of the experimental setup to characterize and assess the reference panel used in fieldwork. In (a) measurements with the FieldSpec Pro ASD used in fieldwork; and (b) measurements with the FieldSpec Pro ASD belonging to the LaRaC laboratory	49
Figure 3.11. In (a) reference surface (target) measurements collection; and (b) Spectralon panel measurements. The two pictures were taken during the	

fieldwork in Atacama Desert, Chile. The collection in the other three fieldworks (Brazil, Algodones Dunes and SDSU site) were similar	51
Figure 3.12. In (a) the sun photometer CE317/CIMEL; and (b) Automated Solar Radiometer (ASR).....	53
Figure 3.13. Solar zenith angle as a function of measuring time with the sun photometer. In (a) on 25 July 2014 in Brazil; (b) on 21 August 2014 in Atacama Desert; (c) on 9 March 2015 in Algodones Dunes; (d) on 3 September 2015 in SDSU site.....	55
Figure 3.14. Optical airmass as a function of the sun's zenith angle. In (a) on 25 July 2014 in Brazil; (b) on 21 August 2014 in Atacama Desert; (c) on 9 March 2015 in Algodones Dunes; (d) on 3 September 2015 in SDSU site	56
Figure 3.15. Optical airmass uncertainties. In (a) on 25 July 2014 in Brazil; (b) on 21 August 2014 in Atacama Desert; (c) on 9 March 2015 in Algodones Dunes; (d) on 3 September 2015 in SDSU site.....	57
Figure 3.16. Total Optical depth at 940 nm. In (a) on 25th July 2014 in Brazil; (b) on 21th August 2014 in Atacama Desert; (c) on 9th March 2015 in Algodones Dunes; (d) on 3rd September 2015 in SDSU site. The uncertainties are very small comparable with the graph scale	59
Figure 3.17. In (a) OLI/Landsat-8 image from west of Bahia State site, Brazil; (b) OLI/Landsat-8 image from Atacama Desert site, Chile; (c) MUX/CBERS-4 image from Algodones Dunes site, USA; (d) WFI/CBERS-4 image from SDSU site. The red box indicates the location of the study area	62
Figure 3.18. General work flowchart for cross-calibration	64
Figure 3.19. Location of the Libya-4 site	65
Figure 3.20. Libya-4 image from (a) OLI/Landsat-8 (b) MUX/CBERS-4 and (c) WFI/CBERS-4. The red box indicates the location of the study area .	66
Figure 3.21. Atacama Desert image from (a) OLI/Landsat-8 (b) MUX/CBERS-4 and (c) WFI/CBERS-4. The red box indicates the location of the study area .	67
Figure 3.22. Average TOA reflectance profile of 224 Hyperion/EO-1 images over Libya-4 from 2004 to 2014	69
Figure 3.23. Average TOA reflectance over Atacama Desert profile from ground measurements	70
Figure 3.24. Algodones Dunes image from (a) Hyperion/EO-1; (b) EMT+/Landsat-7; (c) MUX/CBERS-4 and (d) WFI/CBERS-4. The five red boxes indicate the location of the five ROIs	75
Figure 4.1. In (a) and (b) radiance as a function of wavelength of the FieldSpec F6426 and F18184, respectively; and (c) and (d) relative uncertainty as a function of wavelength of the FieldSpec F6426 and F18184, respectively	78
Figure 4.2. Difference between the measurements with the integrating sphere source made before and after fieldwork as a function of the wavelength. In (a)	

	with the FieldSpec F6426; and (b) with the FieldSpec F18184. The different presents in this figure are from laboratory 1 compared with laboratory 2	79
Figure 4.3.	In (a) reflectance factor of the panel reflectance used in fieldwork as a function of wavelength; and (b) uncertainties (mean standard deviation) as a function of wavelength	80
Figure 4.4.	Difference between the measurements of the reference panel reflectance made before and after fieldwork as a function of the wavelength	80
Figure 4.5.	In (a) Spectral reflectance results of the reference sites; and (b) surface coefficient of variation in percentage	81
Figure 4.6.	Langley graph on July 25 th , 2014 in Brazil site, for spectral bands of the CE317/CIMEL sun photometer	82
Figure 4.7.	Langley graph on August 21 st 2014 in Atacama Desert, Chile, for spectral bands of the CE317/CIMEL sun photometer	83
Figure 4.8.	Langley graph on March 9 th 2015 in Algodones Dunes, USA, for spectral bands of the Automated Solar Radiometer (ASR)	83
Figure 4.9.	Langley graph on September 3 th 2015 in SDSU site, USA, for spectral bands of the Automated Solar Radiometer (ASR)	83
Figure 4.10.	Modified Langley graph. In (a) on July 25 th , 2014 in Brazil site, for water band of the CE317/CIMEL sun photometer; (b) on August 21 st 2014 in Atacama Desert, Chile, for water band of the CE317/CIMEL sun photometer; (c) on March 9 th 2015 in Algodones Dunes, USA, for water band of the Automated Solar Radiometer (ASR); and (d) on September 3 th 2015 in SDSU site, USA, for water band of the Automated Solar Radiometer (ASR)	92
Figure 4.11.	TOA radiance uncertainty predicted by MODTRAN. In (a) on July 25 th , 2014 in Brazil site; (b) on August 21 st 2014 in Atacama Desert, Chile; (c) on March 9 th 2015 in Algodones Dunes, USA; and (d) on September 3 th 2015 in SDSU site	94
Figure 4.12.	TOA radiance predicted by MODTRAN and its final relative uncertainty (in percentage)	95
Figure 4.13.	Comparison of radiance/reflectance reported by OLI/andsat-8 and radiance/reflectance predicted with the reflectance-based approach. The error bars in this graph are the uncertainties of OLI/andsat-8 sensor (5% in radiance and 3% in reflectance)	98
Figure 4.14.	Simulated reflectance factor histogram for the spectral blue band and for Libya-4 site. In (a) and (b) sensor OLI/Landsat-8 with maximum and minimum correlation, respectively; (d) and (d) sensor MUX/CBERS-4 with maximum and minimum correlation, respectively; (e) and (f) sensor WFI/CBERS-4 with maximum and minimum correlation, respectively. 103	

Figure 4.15. Simulated SBAF histogram used to compensate the MUX/CBERS-4 TOA reflectance to match OLI/Landsat-8 TOA reflectance. In (a) Libya-4 site with maximum correlation; (b) Libya-4 site with minimum correlation; (c) Atacama Desert site with maximum correlation; (d) Atacama Desert site with minimum correlation.....	106
Figure 4.16. Simulated SBAF histogram used to compensate the WFI/CBERS-4 TOA reflectance to match OLI/Landsat-8 TOA reflectance. In (a) Libya-4 site with maximum correlation; (b) Libya-4 site with minimum correlation; (c) Atacama Desert site with maximum correlation; (d) Atacama Desert site with minimum correlation.....	107
Figure 4.17. Radiometric calibration of MUX/CBERS-4	113
Figure 4.18. Radiometric calibration of WFI/CBERS-4	114
Figure 4.19. Gain coefficients of the MUX/CBERS-4 spectral bands	116
Figure 4.20. Gain coefficients of the WFI/CBERS-4 spectral bands	116
Figure 4.21. TOA reflectance comparison between ETM+/Landsat-7 and MUX/CBERS-4 and WFI/CBERS-4 after application of the SBAF.....	117

LIST OF TABLES

Table 2.1. Value of the coverage factor and the level of confidence assuming a normal distribution.....	26
Table 3.1. Technical characteristics of the sensor OLI on-board Landsat-8	35
Table 3.2. Technical characteristics of the sensors MUX/WFI/CBERS-4.....	38
Table 3.3. Summary of the dates of the four calibration campaigns using the reflectance-based approach.....	45
Table 3.4. Lamps settings in the integrating sphere source	47
Table 3.5. Reflectance factor measurements local time, fieldwork dates and test site layout. In gray are highlighted the dates which the satellite overpassed the region (calibration dates)	52
Table 3.6. Atmospheric measurements schedule, Julian day, and the day angle. In gray are highlighted the dates which the satellite overpassed the region (calibration dates)	54
Table 3.7. The region of interest (ROI) related to each test site.....	61
Table 3.8. Metadata of scenes used for MUX/WFI/CBERS-4 and OLI/Landsat-8 cross-calibration.....	66
Table 3.9. Solar Exoatmospheric spectral irradiances ($E_{SUN\lambda}$) for MUX/CBERS-4, WFI/CBERS-4 and OLI/Landsat-8 spectral bands.....	72
Table 3.10. Metadata of scenes used for MUX/CBERS-4 and WFI/CBERS-4 validation	74
Table 4.1. Total optical depth, τ_{λ} , and calibration constant, $V_{0,\lambda}$ of the CE317/CIMEL in measurements performed in Brazil site	84
Table 4.2. Total optical depth, τ_{λ} , and calibration constant, $V_{0,\lambda}$ of the CE317/CIMEL in measurements performed at Atacama Desert site in Chile.....	85
Table 4.3. Total optical depth, τ_{λ} , and calibration constant, $V_{0,\lambda}$ of the Automated Solar Radiometer (ASR) in measurements performed at Algodones Dunes site in USA	86
Table 4.4. Total optical depth, τ_{λ} , and calibration constant, $V_{0,\lambda}$ of the Automated Solar Radiometer (ASR) in measurements performed at SDSU site in USA.....	86
Table 4.5. Rayleigh scattering, $\tau_{Rayleigh}$, and aerosol optical depth, $\tau_{Aerosol}$, of the CE317/CIMEL in measurements performed in Brazil site.....	88
Table 4.6. Rayleigh scattering, $\tau_{Rayleigh}$, and aerosol optical depth, $\tau_{Aerosol}$, of the CE317/CIMEL in measurements performed at Atacama Desert site in Chile	89
Table 4.7. Rayleigh scattering, $\tau_{Rayleigh}$, and aerosol optical depth, $\tau_{Aerosol}$, of the Automated Solar Radiometer (ASR) in measurements performed at Algodones Dunes site in USA	90

Table 4.8. Rayleigh scattering, $\tau_{Rayleigh}$, and aerosol optical depth, $\tau_{Aerosol}$, of the Automated Solar Radiometer (ASR) in measurements performed at SDSU site in USA.....	90
Table 4.9. Horizontal Visibility, VIS , and the aerosol optical depth at 550 nm, $\tau_{Aerosol,550nm}$	91
Table 4.10. Water vapor column abundance, W	93
Table 4.11. TOA radiance predicted by MODTRAN and from image of the OLI/Landsat-8 using Brazil and Atacama Desert sites. In this table is also presented the percent difference (see Equation 4.1) and the residue (the difference between the predicted value and the observed value)	96
Table 4.12. TOA reflectance predicted by MODTRAN and from image of the OLI/Landsat-8 using Brazil and Atacama Desert sites. In this table is also presented the percent difference (see Equation 4.1) and the residue (the difference between the predicted value and the observed value, divided by the associated uncertainty).....	97
Table 4.13. Summary of reflectance-based approach results for MUX/CBERS-4 using Algodones Dunes site	100
Table 4.14. Summary of reflectance-based approach results for WFI/CBERS-4 using Algodones Dunes and SDSU sites.....	100
Table 4.15. Radiometric calibration coefficient G (coefficient gain) of MUX/CBERS-4 and WFI/CBERS-4 using Algodones Dunes site	101
Table 4.16. Average MUX/CBERS-4, WFI/CBERS-4 and OLI/Landsat-8 simulated reflectance for Libya-4 site.....	104
Table 4.17. Average MUX/CBERS-4, WFI/CBERS-4 and OLI/Landsat-8 simulated reflectance factor for Atacama Desert site.....	105
Table 4.18. SBAF and its uncertainty used to compensate the MUX/CBERS-4 TOA reflectance to match OLI/Landsat-8 TOA reflectance	107
Table 4.19. SBAF and its uncertainty used to compensate the WFI/CBERS-4 TOA reflectance to match OLI/Landsat-8 TOA reflectance	108
Table 4.20. Summary of cross-calibration results for MUX/CBERS-4 using Libya-4 Dunes and Atacama Desert sites.....	109
Table 4.21. Summary of cross-calibration results for WFI/CBERS-4 using Libya-4 Dunes and Atacama Desert sites.....	110
Table 4.22. Radiometric calibration coefficient G (coefficient gain) of MUX/CBERS-4 and WFI/CBERS-4 I using Libya-4 and Atacama Desert sites.....	111
Table 4.23. Linear fits results corresponding to the plots shows in Figure 4.17 and Figure 4.18.....	114
Table 4.24. Landsat-7 and CBERS-4 percentage difference in TOA reflectance of the five ROIs.....	118

LIST OF ABBREVIATIONS

AOD	Aerosol Optical Depth
ASD	Analytical Spectral Devices
ASR	Automated Solar Radiometer
CBERS	China Brazil Earth Resources Satellite
CEOS	Committee on Earth Observation Satellite
CV	Coefficient of Variation
DN	Digital Number
ETM+	Enhanced Thematic Mapper Plus
FOV	Field of View
FWHM	Full Width at Half Maximum
GUM	Guide to the Expression of Uncertainty in Measurement
IEAv	Instituto de Estudos Avançados
INPE	National Institute for Space Research
ISO	International Organization for Standardization
LaRaC	Laboratório de Radiometria e Caracterização de Sensores Eletroóptico
MODTRAN	Moderate Resolution Atmospheric Radiance and Transmittance Model
MUX	Multispectral Camera
OLI	Operational Land Imager
PDF	Probability Density Function
PICS	Pseudo Invariant Calibration Sites
RF	Reflectance Factor
ROI	Region of Interest
SBAF	Spectral Band Adjustment Factor
SDSU	South Dakota State University
SRF	Spectral Response Function
TOA	Top-of-Atmosphere
USGS	United States Geological Survey
VIS	Horizontal Visibility
WFI	Wide-Field Imager
WGCV	Working Group on Calibration and Validation

LIST OF SIMBOLS

α	Ångström's exponent
β	Ångström's turbidity parameter
G	Coefficient gain
χ^2	Chi-square
<i>offset</i>	Coefficient bias
R^2	Coefficient of Determination
da	Day Angle
d	Earth-Sun Distance
h	Flight Altitude
E	Irradiance
J	Julian Day
E_0	Mean Exoatmospheric Solar Irradiance
m	Optical Airmass
∂	Partial Derivative
p	Pixel Dimension
ρ_{TOA}	Reflectance Planetary Top-of-Atmosphere
P_0	Pressure at Sea Level
L	Radiance
χ_{red}^2	Reduced Chi-square
ρ	Reflectance
θ	Solar Zenith Angle
V	Sun Photometer Output
P	Surface Pressure
τ	Total Optical Depth
T	Transmittance
σ	Uncertainty
W	Water Vapor Content
λ	Wavelength

CONTENTS

1 INTRODUCTION	1
1.1. Objective.....	4
2 THEORETICAL BACKGROUND	7
2.1. Reflectance-Based Approach	8
2.1.1. Surface Reflectance	10
2.1.2. Atmospheric Characterization	11
2.1.3. Radiative Transfer Code.....	14
2.1.4. Image Analysis and Calibration Coefficients.....	15
2.2. Cross-Calibration Method	16
2.2.1. Spectral Response Function	18
2.2.2. Spectral Band Adjustment Factor.....	19
2.2.3. Image Pair.....	21
2.3. Evaluation of Uncertainties	22
2.3.1. ISO-GUM Method	23
2.3.2. Monte Carlo Simulation Method.....	27
2.4. Fitting.....	29
3 MATERIAL AND METHODS	33
3.1. Earth Observation Sensors: OLI/Landsat-8 and MUX/WFI/CBERS-4.....	34
3.2. Reflectance-Based Approach	38
3.2.1. Test Sites Overview.....	39
3.2.2. Laboratory Measurements	45
3.2.3. Field Measurements	50
3.2.4. Radiative Transfer Code.....	60
3.2.5. Image Analysis and Calibration Coefficients.....	61
3.3. Cross-Calibration Method	64
3.3.1. Test Sites Overview.....	65
3.3.2. Image Pair.....	66
3.3.3. Image Processing.....	67
3.3.4. Spectral Band Adjustment Factor.....	68
3.3.5. Image Analysis and Calibration Coefficients.....	71
3.4. Validation of the MUX/WFI/CBERS-4 Radiometric Calibration Coefficients.....	73

4 RESULTS AND DISCUSSION	77
4.1. Reflectance-Based Approach	77
4.1.1. Laboratory Measurements	77
4.1.2. Field Measurements	80
4.1.3. MODTRAN	93
4.1.4. OLI/Landsat-8 Radiometric Calibration.....	96
4.1.5. MUX/WFI/CBERS-4 Radiometric Calibration	99
4.2. Cross-Calibration Method	101
4.2.1. Spectral Band Adjustment Factor.....	102
4.2.2. MUX/WFI/CBERS-4 Radiometric Calibration	109
4.3. Combination of Techniques	112
4.4. Validation of the MUX/WFI/CBERS-4 Radiometric Calibration Coefficients ...	116
5 CONCLUSIONS AND RECOMMENDATIONS	121
REFERENCES	127

1 INTRODUCTION

The development of Earth observation sensors (orbital and airborne) has allowed conducting numerous studies involving the Earth's natural resources. However, the capacity to detect and to quantify changes on the Earth's environment depends on sensors that provide calibrated and consistent data of the Earth's surface features through time (BIGGAR et al., 1994; CHANDER et al., 2009). High degree of reliability in the sensor absolute radiometric calibration is indispensable to use the data for quantitative investigations, i.e. radiometric calibration is essential in approaches where it is necessary inferring the geophysical and biophysical properties of the objects.

Data from Earth observation sensors are stored as digital numbers (DN). Absolute radiometric calibration enables the conversion of image DN's to physical units, such as radiance. It can be performed prior to sensor launching (pre-flight calibration) or/and throughout the sensor's lifetime (in-flight calibration). Pre-flight calibration is performed in laboratory under controlled conditions (temperature, humidity, pressure, etc.). In general, for the electromagnetic spectrum region from 400 to 2500 nm (visible, near-infrared and mid-infrared), an integrating sphere source is used as a calibration standard (CHEN, 1997; AVELISIO et al., 2007). The calibration of a sensor system running in the thermal spectrum region can be performed using a large-area blackbody as a reference source (CHEN, 1997). The pre-flight calibration allows testing the system sensor to ensure it operates properly before being integrated into the launch vehicle (THOME et al., 1997). However, the sensor launching stresses and the rigors of the space environment may significantly affect the pre-flight absolute radiometric calibration of the sensor (HELDER et al., 2013).

The in-flight calibration helps to understand the sensor's behavior on-orbit throughout the sensor's operating lifetime. It can be performed using an internal calibration source (on-board calibration) and/or by acquiring radiance measurements from the Earth's surface (vicarious calibration). In-flight on-board calibration is conducted by an internal calibration system using artificial or natural light sources (DUAN et al., 2013). The common on-board reference sources used for system sensors operating in the solar reflective spectrum are lamps and solar diffusers. On-board blackbodies are used to calibrate the thermal spectral bands. Some satellite sensors, such as MODIS (Moderate

Resolution Imaging Spectroradiometer), ASTER (Advanced Spaceborne Thermal Emission and Reflection Radiometer) and the sensors on-board Landsat satellites series have been assembled with internal calibration systems (XIONG et al., 2007; THOME et al., 1998; MARKHAM et al., 2001). However, it is possible that degradation of the internal calibration system may occur over sensor's operating lifetime. In addition, some Earth observation sensors do not have on-board calibrators. Thus, in instances when internal calibration systems are not reliable or are absent, vicarious calibration method arises as an alternative.

Vicarious calibration is a technique that attempts to predict the radiance at the sensor, i.e. top-of-atmosphere (TOA) radiance, over a selected test site on the Earth's surface. It has become widely adopted as the means to provide independent assurance of the quality of remotely sensed data (DINGUIRARD e SLATER, 1999; BIGGAR et al., 2003; THOME et al. 2008). This current work focuses on the two most common vicarious calibration methods: (a) reflectance-based approach; and (b) cross-calibration method. The reflectance-based approach requires ground reflectance (or radiance) and atmospheric measurements coincident with the sensor overpass over a selected surface. The in-situ measurements are used as input into a radiative transfer code that predicts TOA radiance, which is compared to the radiance reported by the sensor system. The radiometric calibration coefficients of the sensor are determined from this comparison. The reflectance-based approach was effectively implemented by several research groups and applied to several Earth observing sensors such as ETM+/Landsat-7, OLI/Landsat-8, ASTER/Terra and Hyperion/EO-1 (THOME, 2001; CZAPLA-MYERS et al., 2015; THOME et al., 2008; MCCORKEL et al., 2013).

Cross-calibration is a method where the response of a sensor is compared with the response of another one that has a better known radiometric calibration (well-understood and well-calibrated sensor), via near-simultaneous imaging of a common ground target. Although more complex due to variables such as coincident acquisition times, viewing and illumination geometries, and spectral coverage differences, the method is one of the most important techniques able to tie sensors onto a common radiometric scale (CHANDER et al., 2013a). The cross-calibration emerges as an alternative method and/or supplement to lower costs in implementation of

calibration. Unlike reflectance-based approach, the cross-calibration does not involve laborious and intensive ground measurements with expensive and sensitive radiometric equipment. Thus, it is interesting to include alternatives to absolute calibration methods to minimize costs and maximize the frequency of sensor systems calibration.

It is important to emphasize that confidence in a measured value requires a quantitative report of its quality, being necessary the evaluation of the uncertainty associated with the value (PINTO et al., 2016a). This procedure is essential because during the absolute calibration of the sensors, either by the reflectance-based method or by the cross-calibration, various measurements and analysis are performed, which results should be as reliable as possible. The ground radiometric measurements from the surface, the atmospheric measurements and the determination of calibration coefficients are incomplete unless accompanied by a statement of their uncertainties. The radiometric calibration uncertainty is a key in reliability of calibration results. Without calculating the uncertainty involved in the process, measurement results cannot be compared, either among themselves or with reference values given in a specification or standard (JCGM, 2008a; PONZONI et al., 2015).

In Brazil, activities involving the absolute radiometric calibration of satellite sensors started in the 2000s. Since then, it is considered that there was a significant advance in knowledge on the subject. However, Brazil calibration studies have focused only on reflectance-based method and, therefore, the cross-calibration has been underexplored in the country. Besides, it is important to note that until the end of 2009 all the radiometric calibration tasks were carried out without uncertainties estimations (LAMPARELLI et al. 2003; PONZONI et al., 2006; PONZONI et al., 2008). From 2010 some works began to be performed taking into account the uncertainties, as described by Pinto (2011) and Pinto et al. (2012). Despite this substantial progress, it has not been developed and applied a methodology to assess the uncertainties taking into account all stages of a complete absolute calibration mission. Therefore, it is necessary to improve the current calibration methods, including uncertainties estimations in both measurements and procedures. The relative little knowledge about the cross-calibration procedure and the lack of uncertainties estimation associated with

the absolute calibration procedures compromises the reliability of the data provided, for example, by the China-Brazil Environmental Resources Satellite program (CBERS).

In this context, this thesis proposes a methodology for evaluating the uncertainty in the in-flight absolute radiometric calibration of Earth observation sensors. This present work is structured as follows. **Section 2** presents a theoretical background, including a review of the both calibration methods utilized (reflectance-based approach and cross-calibration method) and both methods to evaluate uncertainties (classical method and the Monte Carlo Simulation). **Section 3** describes the three optical sensors used to evaluate the methodology (OLI/Landsat-8 and MUX/WFI/CBERS-4) and how it was performed the radiometric calibration using both reflectance-based approach and cross-calibration method. The results and discussions are presented in **section 4**. Finally, in **section 5**, conclusions and recommendations remarks are addressed.

1.1. Objective

The general objective of the present work was to develop a methodology to evaluate the uncertainties inherent in the in-flight absolute radiometric calibration of Earth observation sensors. The main idea is to identify the relationship between the uncertainties caused by various factors and the overall uncertainty. The uncertainties involved in the calibration procedure were quantified by combining two uncertainty evaluation methods: classical and Monte Carlo methods. The analyses of the uncertainties were carried out in the region of the visible, near-infrared and short wave-infrared of the electromagnetic spectrum, between 350 and 2400 nm. Furthermore, the methodology for assessing uncertainties proposed in this present work was applied for both absolute radiometric calibration methods: reflectance-based approach and cross-calibration method.

The working hypothesis was that this new methodology is compatible with other methods practiced by the international science community of satellite radiometric calibration and it will allow Brazil to have a quantitative indication of the absolute calibration final results.

The specific objectives were to:

- ✓ Identify the main sources of uncertainty in the reflectance-based approach and cross-calibration method;
- ✓ Evaluate the suitability of two sites located in South America (Chile and Brazil) to be used as a reference surfaces for calibration of Earth observation sensors purposes;
- ✓ Evaluate the potential of the Monte Carlo simulation method as an alternative and complementary to the method traditionally used to estimate the uncertainty in the absolute radiometric calibration;
- ✓ Perform the radiometric calibration of the Operational Land Imager (OLI) on-board Landsat-8 and compare the results with those obtained with other teams that carry out the calibration of Landsat series;
- ✓ Describe the complete procedure to perform the absolute radiometric calibration of the sensors Multispectral Camera (MUX) and Wide Field Imager (WFI) on-board CBERS-4;
- ✓ Estimate, along its associated uncertainties, the absolute radiometric calibration coefficients for the sensors MUX and WFI on-board CBERS-4, which allows converting the digital numbers from the image data to useful quantities such as radiance.

2 THEORETICAL BACKGROUND

Data from Earth observation sensors are stored as digital numbers (DN). The goal of absolute radiometric calibration is to determine the radiometric coefficients that will convert the DNs from an image in a physical quantity, such as radiance. In general, there is a linear relationship between the DN and radiance response described by (CHANDER et al., 2009):

$$L_{\lambda} = \left(\frac{L \max_{\lambda} - L \min_{\lambda}}{DN \max_{\lambda} - DN \min_{\lambda}} \right) \times (DN_{\lambda} - DN \min_{\lambda}) + L \min_{\lambda} \quad (2.1)$$

where: λ is the wavelength; L_{λ} is the spectral radiance at the sensor's aperture in units of $[W/(m^2 \cdot sr \cdot \mu m)]$; DN is the digital number from the image; $DN \max_{\lambda}$ and $DN \min_{\lambda}$ are, respectively, the maximum and minimum digital number value that the sensor is able to register; and $L \max_{\lambda}$ and $L \min_{\lambda}$ are, respectively, the maximum and minimum radiance value that the sensor can measure. The $L \max_{\lambda}$ and $L \min_{\lambda}$ values are the radiometric coefficients. For sensors quantized in 8 bits, as observed at ETM+ (Enhanced Thematic Mapper Plus) on-board Landsat-7, for example, $DN \max$ and $DN \min$ values are 255 and 0, respectively.

Equation 2.1, which relates the radiance with DN , can also be written as:

$$L_{\lambda} = G_{\lambda} \times DN_{\lambda} + offset_{\lambda} \quad (2.2)$$

where:

$$G_{\lambda} = \frac{L \max_{\lambda} - L \min_{\lambda}}{DN \max_{\lambda} - DN \min_{\lambda}} \quad (2.3)$$

$$offset_{\lambda} = L \min_{\lambda} - \left(\frac{L \max_{\lambda} - L \min_{\lambda}}{DN \max_{\lambda} - DN \min_{\lambda}} \right) \times DN \min_{\lambda} \quad (2.4)$$

where: G is the coefficient gain in units of $[W/(m^2 \cdot sr \cdot \mu m)]$; and $offset$ is the coefficient bias in units of $[W/(m^2 \cdot sr \cdot \mu m)]$.

The TOA (top-of-atmosphere) reflectance of the Earth is computed according to the equation (TEILLET et al., 2001; TEILLET et al., 2006; CHANDER et al., 2009):

$$\rho_{TOA,\lambda} = \frac{\pi \times L_{\lambda} \times d^2}{E_{0,\lambda} \times \cos \theta} \quad (2.5)$$

where: $\rho_{TOA,\lambda}$ is the planetary top-of-atmosphere (TOA) reflectance [unitless]; π is a mathematical constant [unitless]; $E_{0,\lambda}$ is the mean exoatmospheric solar irradiance [$W/(m^2 \cdot \mu m)$]; d is the Earth-Sun distance [astronomical units]; and θ is the solar zenith angle.

After algebraic manipulation of **Equation 2.2** and **Equation 2.5**:

$$\rho_{TOA,\lambda} = \frac{\pi \times d^2 \times (G_{\lambda} \times ND_{\lambda} + offset_{\lambda})}{E_{0,\lambda} \times \cos \theta} \quad (2.6)$$

Several in-flight radiometric calibration methods have been proposed for Earth observation sensors (SLATER et al., 1987; DINGUIRARD and SLATER, 1999; PINTO et al., 2013a). Perhaps, the two most common methods of in-flight calibration are: reflectance-based approach and cross-calibration method described, respectively, in **section 2.1** and **section 2.2**.

2.1. Reflectance-Based Approach

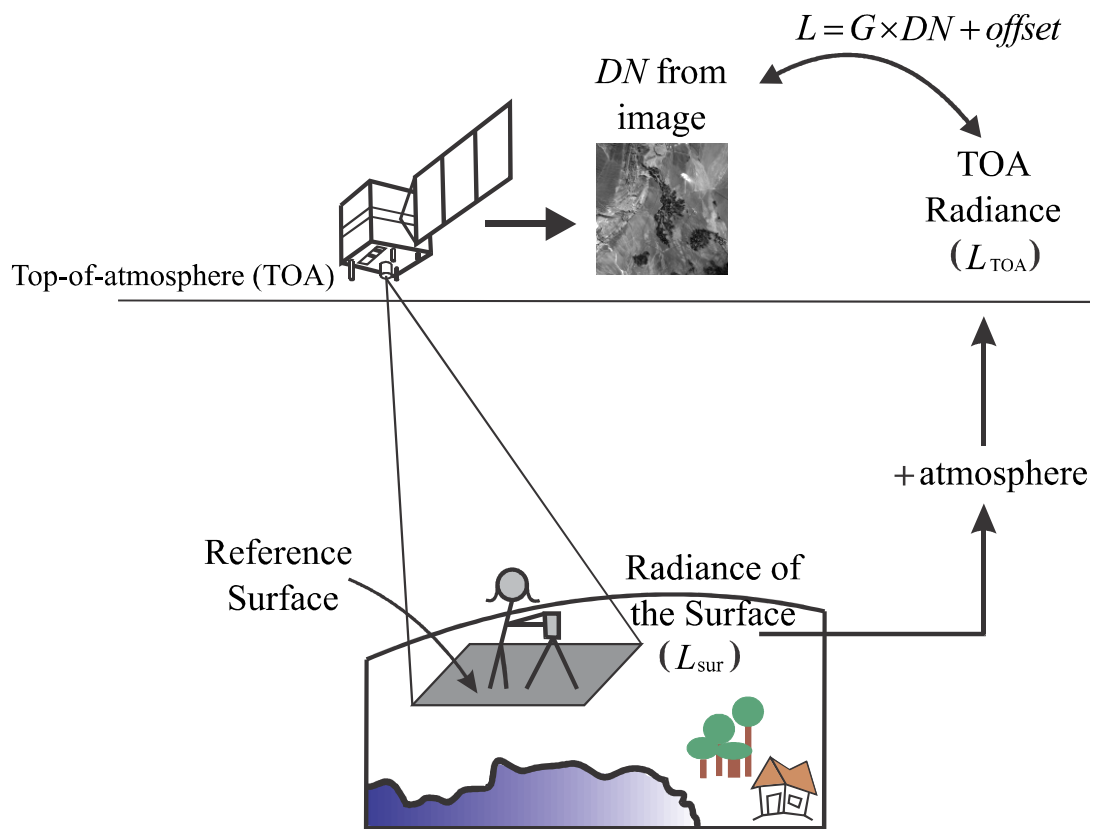
The first and most critical stage of the reflectance-based calibration method is choosing a reference surface with specific, uniform and stable characteristics (SCOTT et al., 1996), which can be divided into two groups: (a) characteristics related to atmospheric and geographic issues, i.e., the region must have low cloudiness rates, high altitude and be flat; and (b) the physical characteristics, such as high reflectance values, isotropy and uniformity over a desired spectral range, should be stable over time. Furthermore, it is also desirable that the surface be easily accessible.

In fact, any Earth's surface can be used in reflectance-based approach, i.e., it is not mandatory that the surface actually presents all the characteristics mentioned above. The key is to know the surface reflectance (or surface radiance), which can be obtained, for

example, in areas covered by vegetation that are considered "non-ideal" due to seasonal changes. The primary idea behind these characteristics is to get closer to the ideal case of “zero atmosphere” by maximizing the reference surface signal due to directly reflected solar irradiance (MCCORKEL et al., 2013). Therefore, these “ideal” characteristics facilitate the measurements, calculations and possibly reduce uncertainties, increasing the reliability performing the calibration procedures.

The reflectance-based approach requires an accurate field radiometric measurement concurrent with the overpass of the sensor (THOME et al., 2004). The ground based radiometric measurements involve two distinct types of measurements: one for determination of the surface radiance (or reflectance) and the other to characterize the atmosphere. The data derived from ground measurements are used as input in a radiative transfer code to predict the radiance/reflectance values at sensor level (top-of-atmosphere radiance). These results are then compared to the digital number reported by the sensor to provide a set of bias and gains for the sensor bands (radiometric calibration coefficients). In **Figure 2.1** is illustrated the reflectance-based approach process.

Figure 2.1. Illustrative scheme of reflectance-based approach procedures.



Looking at **Figure 2.1** it is possible to notice some significant factors of reflectance-based approach: reflectance (or radiance) measurement of the selected surface as a reference, atmosphere characterization technique to "add" the atmosphere to data measured on the field and the sensor image that will be used for comparison. In the next four sections are described each of these factors.

2.1.1. Surface Reflectance

Reflectance is the ratio of the total amount of electromagnetic radiation (EM) reflected by a surface to the total amount of EM incident on the surface (MILTON, 1987). However, reflectance cannot be measured directly, because the infinitesimal elements of the solid angle do not include measurable amounts of radiant flux (SCHAEPMAN-STRUB et al., 2006). Thus, due to technical difficulties measuring reflectance in either field measurements or laboratory, the reflectance factor (RF) is the equivalent used in practice (MILTON, 1987). This quantity is the ratio of spectral radiance reflected from a sample (target) to the spectral radiance that would be reflected by a perfect diffuse Lambertian surface, under the same geometric conditions, according to **Equation 2.7** (MILTON, 1987). The term reflectance is often used in a general sense. In practice, a perfectly reflecting panel does not exist; therefore, a correction is made to account for the spectral reflectance panel.

$$RF_{target}(\theta_i, \phi_i, \theta_r, \phi_r, \lambda) = \frac{L_{target}(\theta_r, \phi_r, \theta_i, \phi_i, \lambda)}{L_{panel}(\theta_i, \phi_i, \lambda)} \times k_\lambda \quad (2.7)$$

where: L_{target} is the radiance of the target; L_{panel} is the radiance of the reference panel under the same specified conditions of illumination and viewing; λ is the wavelength; θ is the angle from the vertical (zenith angle); ϕ is the angle measured in the horizontal plane (azimuth angle); the subscripts i and r denote incident and reflected rays, respectively; k_λ is the panel correction factor (usually determined in the laboratory).

One of the objectives during ground radiometric measurements is to characterize the reflectance of the reference surface (**Equation 2.7**). Therefore, in general, two instruments are employed: (i) radiometers or spectroradiometer; and (ii) reference panels. Radiometers and/or spectroradiometer are instruments used to quantitatively measure the intensity of electromagnetic radiation. The most popular portable

spectroradiometer applied in the field in remote sensing is the FieldSpec (ASD Inc., a PANalytical company), which operates in the spectral range from 350 through 2500 nm (ASD, 1999). Radiometric measurements of the reference surface are alternated with radiometric measurements of the reference panel. The reference panels can be manufactured from a variety of materials, such as barium sulfate (BaSO_4), magnesium oxide (MgO) or Spectralon (PINTO, 2011; LABSPHERE, 2009). Currently, Spectralon is the most frequently used for manufacturing reference panels. According to Höpe and Hauer (2010), besides good lambertian scattering behavior, the advantage over other comparable materials is its superior high reflectance even in the ultraviolet (UV) spectral region. Spectralon panels also are durable and maintain a consistent reflectance over time. In addition, Spectralon panels are weather resistant and washable, qualities well suited for reference reflectance panels (JACKSON et al., 1992).

2.1.2. Atmospheric Characterization

The atmospheric characterization data are collected at the same time as the surface reflectance measurements are performed. The atmospheric characterization can be carried out using a sun photometer (or solar radiometer). Sun photometer measurements can be used to recover atmospheric parameters, including spectral aerosol optical depth, water vapor, sky radiance distributions and ozone amount (ROLLIN, 2000). The sun photometer generates a digital output signal that is linearly proportional to the solar irradiance. This can be modeled according to the Beer-Lambert-Bouguer attenuation law (SCHMID and WEHRLI, 1995; ROLLIN, 2000; PINTO et al., 2015).

$$V_\lambda = \frac{V_{0,\lambda} \times e^{-\tau_\lambda \times m}}{d^2} \quad (2.8)$$

where: V_λ is sun photometer output, proportional to the solar irradiance for the wavelength λ ; $V_{0,\lambda}$ is the calibration constant for the wavelength λ ; d is Earth-Sun distance factor in Astronomical Units; m is the relative optical airmass [unitless]; and τ_λ is the total optical depth [unitless] for the wavelength λ .

The relative optical airmass, m , can be estimated by secant of the zenith angle (θ_z) (ECHER et al., 2001), or it can be calculated more accurately according to the equation (OSTERWALD and EMERY, 2000):

$$m = \frac{P}{P_0} \times \left[\frac{1}{\cos \theta_z + 0.15 \times (93.885 - \cos \theta_z)^{-1.253}} \right] \quad (2.9)$$

where: θ_z is the solar zenith angle [degrees or radians], which can be obtained from the site latitude, longitude, and time of day; P_0 is the pressure at sea level (approximately 1013.25 hPa); and P is the surface pressure in hPa.

The Earth-Sun distance, d , varies throughout the year, then; it can be estimated using the equation (OSTERWALD and EMERY, 2000):

$$d = 1.00011 + 3.4221 \times 10^{-2} \times \cos(d_a) + 1.28 \times 10^{-3} \times \sin(d_a) + 7.19 \times 10^{-4} \times \cos(2d_a) + 7.7 \times 10^{-5} \times \sin(2d_a) \quad (2.10)$$

where: d_a is the day angle, calculated by:

$$d_a = (J - 1) \times \frac{2\pi}{365} \quad (2.11)$$

where: J is the Julian day of the year integer (or day-of-year).

To estimate the influence of the atmosphere using **Equation 2.8** it is necessary to determine $V_{0,\lambda}$ and τ_λ values. Therefore, the Langley method is used that consists in the linearization of Beer's law:

$$\ln(V_\lambda \times d^2) = \ln(V_{0,\lambda}) - m \times \tau_\lambda \quad (2.12)$$

According to this law, if a series of measurement is performed for different optical air masses and during a time period where the total optical depth remains constant, then, it is possible to estimate $V_{0,\lambda}$ and τ_λ . Langley method result is a linear fitting, where the linear coefficient is the natural logarithm of $V_{0,\lambda}$, and the slope coefficient is τ_λ .

The total optical depth, τ_λ , can be expressed by the following equation (ROLLIN, 2000; PONZONI et al., 2015; PINTO et al., 2015):

$$\tau_\lambda = \tau_{Rayleigh,\lambda} + \tau_{Aerosols,\lambda} \quad (2.13)$$

where: $\tau_{Aerosol,\lambda}$ is the aerosol optical depth; and $\tau_{Rayleigh,\lambda}$ is the optical depth due to Rayleigh scattering.

The Rayleigh component depends only on the wavelength, λ [μm], the pressure at sea level, P_0 , and the pressure at the surface level, P :

$$\tau_{Rayleigh} = \frac{0.008569 \times \lambda^{-4} (1 + 0.0113 \times \lambda^{-2} + 0.00013 \times \lambda^{-4}) \times P}{P_0} \quad (2.14)$$

According to the Ångström's turbidity formula (ROLLIN, 2000), the spectral variation of aerosol optical depth can be written as:

$$\tau_{Aerosols,\lambda} = \beta \times \lambda^{-\alpha} \quad (2.15)$$

where: α is the Ångström's exponent related to the average size distribution of the aerosols; and β is an Ångström's turbidity parameter, which is proportional to both the amount of aerosols and the horizontal visibility VIS [km] (PONZONI et al. 2015):

$$\beta = 0.613 \times e^{-\frac{VIS}{15}} \quad (2.16)$$

Absorption by water vapor is restricted to narrow spectral bands. The extraction of water vapor column abundance from sun photometer measurements usually relies on a measurement in the region of water vapor absorption around 940 nm. Then, the sun photometer spectral range centered at approximately 940 nm is used to estimate the water vapor atmospheric content. However, **Equation 2.8** is not valid throughout the spectral region of absorption by water vapor. In this case, the sun photometer output, V_{940nm} , is estimated using (HALTHORE et al., 1997):

$$V_{940nm} = \frac{V_{0,940nm} \times e^{-\tau_{940nm} \times m}}{d^2} \times T_W \quad (2.17)$$

where: V_{940nm} is the sun photometer output at 940nm; $V_{0,940nm}$ is the calibration constant at 940 nm; τ_{940nm} is the total optical depth at 940 nm; and T_W is the gaseous transmittance, which can be estimated using the following expression (PONZONI et al. 2015):

$$T_W = e^{-a \times W^b \times m^c} \quad (2.18)$$

where: W is the water vapor content (g/cm^2); and a , b and c are constants, which depend on the equipment used, b and c are approximately equal to 0.5 (ZULLO et al. 1996; HALTHORE et al., 1997)

To determine V_{940nm} and W values, the Langley Modified Method can be applied (HALTHORE et al., 1997). Thus, **Equation 2.17** can be rewritten as:

$$\ln(V_{940nm} \times d^2) + m \times \tau_{940nm} = \ln(V_{0,940nm}) - a \times W^b \times m^c \quad (2.19)$$

A plot of the left side of **Equation 2.19** against m^c yields a straight-line with the ordinate intercept equal to $\ln(V_{0,940nm})$ and the slope equal to $a \times W^b$.

2.1.3. Radiative Transfer Code

An atmospheric radiative transfer code calculates the radiative transfer of electromagnetic radiation through a planetary atmosphere. The objective is to take into account the interference of the atmosphere to radiometric values collected in the field. The data products derived from the ground measurements (the atmospheric and surface reflectance data) and geometries of the sensor/satellite and sun during the passage of the sensor over the reference surface are used as input to a radiative transfer code to predict the top of atmosphere (TOA) radiance/reflectance.

The radiative transfer codes are highly dependent on inputs parameters that consist in: (i) surface reflectance; (ii) column water vapor; (iii) column ozone; (iv) temperature profile; (v) pressure profile; (vi) aerosol properties including Ångström parameter and aerosol optical depth at 550 nm; (vii) geometry of the sensor/satellite; and (viii) geometry of the sun. An important output of the radiative transfer code is the top-of-atmosphere radiance (at-sensor radiance). This output can be averaged with the sensor Spectral Response Function (SRF) of interest to find the band-averaged radiance values.

There are several codes available that satisfy the requirements of predicting the at-sensor radiance. The radiative transfer codes most widely used in the remote sensing community are: (a) the Second Simulation of the Satellite Signal in the Solar Spectrum (6S); and (b) the Moderate Resolution Atmospheric Radiance and Transmittance Model (MODTRAN). The 6S code is an improved version of 5S (Simulation of the Satellite Signal in the Solar Spectrum), developed by the Laboratoire d'optique Atmosphérique (VERMOTE et al., 1997; VERMOTE et al., 2006). The MODTRAN was developed by Spectral Sciences Inc and the US Air Force Research Laboratory (BERK et al., 2011). It is a computationally rigorous algorithm that is used to model the spectral absorption, transmission, emission and scattering characteristics of the atmosphere. This is accomplished by modeling the atmosphere as a set of homogeneous layers (IENTILUCCI, 2007). MODTRAN operates in wavelengths extending from the thermal Infrared (IR) through the visible and into the ultraviolet (BERK et al., 2011).

2.1.4. Image Analysis and Calibration Coefficients

The last step of the reflectance-based approach is determining the calibration coefficient for each sensor spectral band by comparing the digital number (DN) output from the sensor to the predicted at sensor radiance by the radiative transfer code. The DN output is determined by averaging the output for those pixels related to the reference surface site.

In general, the output of the radiative transfer code is the top-of-atmosphere (TOA) radiance for each nanometer. Therefore, before performing this comparison, it is necessary to average the output data of the radiative transfer code with the Spectral Response Function (SRF) (see **section 2.2.1**) of the sensor to find the band averaged at-sensor radiance values at each spectral band, according to the equation:

$$L_{band} = \frac{\int_0^{\infty} L_{\lambda} \times SRF_{\lambda} d\lambda}{\int_0^{\infty} SRF_{\lambda} d\lambda} \quad (2.20)$$

where: L_{band} is the radiance in a specific band; L_{λ} is the radiance as a function of wavelength.

First, the test site on the ground is localized in the image acquired by the sensor. Then, the DN output is estimated by averaging the output for the pixels related to the sensor of the test site. Finally, this average DN is compared with the at-sensor spectral band radiance. This combination generates the radiometric calibration coefficients (gain and *offset* from **Equation 2.2**).

2.2. Cross-Calibration Method

Cross-calibration is one of the several methods used for post-launch Earth Observation Satellites sensor radiometric calibration, which permits the quantitative comparison of measurements obtained from different sensor systems. Thome et al. (2003), for example, used Railroad Valley Playa site to cross-calibrate ALI/EO-1, Hyperion/EO-1, MODIS/Terra and IKONOS with respect to ETM+/Landsat-7. Chander et al. (2004) presented the results from cross-calibration of the ETM+/Landsat-7 and ALI/EO-1 sensors using two approaches. According to Chander et al. (2013a) the cross-calibration is the least mature method of radiometric calibration but one of the most important capabilities needed to tie sensors onto a common radiometric scale.

Cross-calibration is a method where the response of one sensor is compared to the response of another sensor when both sensors are exposed to the same electromagnetic radiation level. Usually, the same radiation level is obtained using near-simultaneous imaging of a common ground target. The radiometric calibration of the reference sensor is transferred to the sensor of interest. **Equation 2.5** can be defined separately for the sensor used as reference and for the sensor to be calibrated:

$$\rho_{\lambda,ref} = \frac{\pi \cdot L_{\lambda,ref} \cdot d_{ref}^2}{[E_{SUN_{\lambda}} \cdot \cos \theta_z]_{ref}} \quad (2.21)$$

$$\rho_{\lambda,cal} = \frac{\pi \cdot L_{\lambda,cal} \cdot d_{cal}^2}{[E_{SUN_{\lambda}} \cdot \cos \theta_z]_{cal}} \quad (2.22)$$

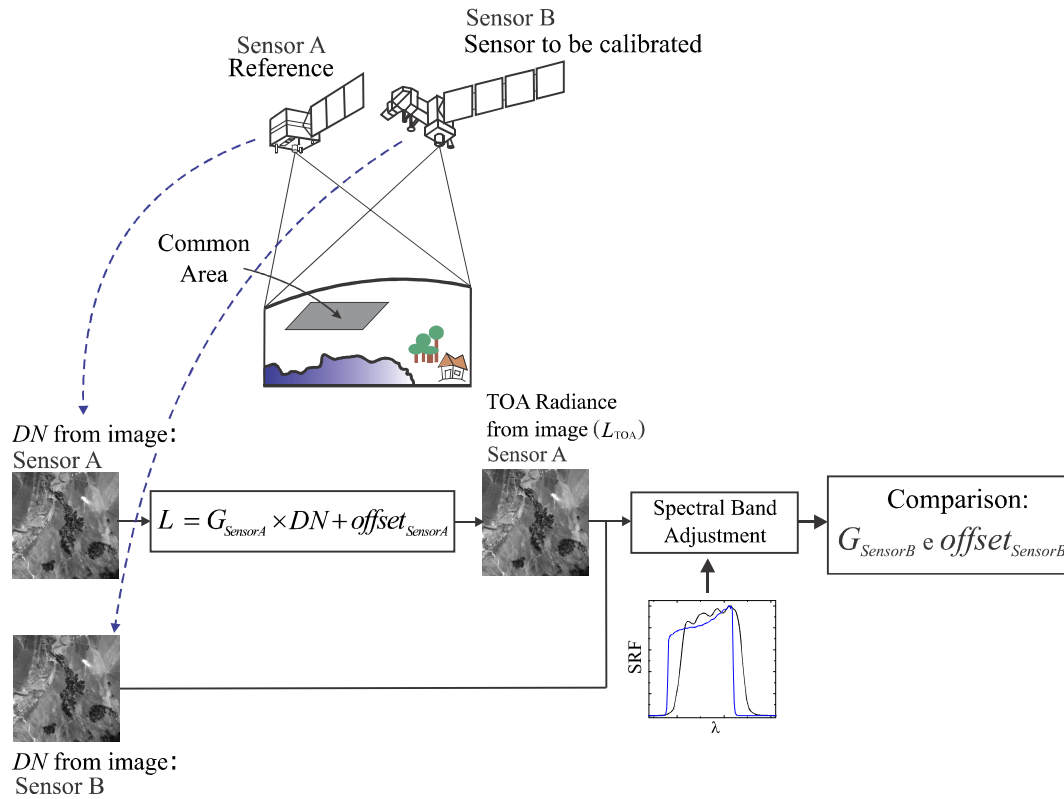
After algebraic manipulation of **Equation 2.21** and **Equation 2.22**:

$$L_{\lambda,cal} = L_{\lambda,ref} \cdot \frac{[E_{SUN_{\lambda}} \cdot \cos \theta_z]_{cal}}{[E_{SUN_{\lambda}} \cdot \cos \theta_z]_{ref}} \cdot \frac{\rho_{\lambda,cal}}{\rho_{\lambda,ref}} \cdot \frac{d_{ref}^2}{d_{cal}^2} \quad (2.23)$$

where: $\rho_{\lambda,cal}/\rho_{\lambda,ref}$ is the inverse of the Spectral Band Adjustment Factor (see **section 2.2.2**). Through this equation the radiance value of the sensor to be calibrated, $L_{\lambda,cal}$, is obtained from the reference sensor radiance, $L_{\lambda,ref}$. It is necessary to reverse **Equation 2.23** if one wants to adjust the sensor to be calibrated with respect to the reference sensor.

The first step of the cross-calibration method is obtaining the image pairs of a common ground target. Second, the digital numbers from the image of the reference sensor is converted in radiance values. Then, this radiance is compared with the digital number from the sensor image of interest. However, in general, the spectral bands differ significantly between sensors, even for bands designed to operate at the same electromagnetic spectrum region. The spectral bands provide substantially different measures that are not directly comparable since their analogous bands may have different Spectral Response Function (SRF) (TEILLET et al., 2007). The differences in spectral responses of the sensors must be quantified and compensated to avoid large uncertainties in cross-calibration results (CHANDER et al., 2013b). For this purpose, it is calculated and used the Spectral Band Adjustment Factor (SBAF). In **Figure 2.2** is illustrated the cross-calibration method procedures.

Figure 2.2. Illustrative scheme of cross-calibration method procedures.



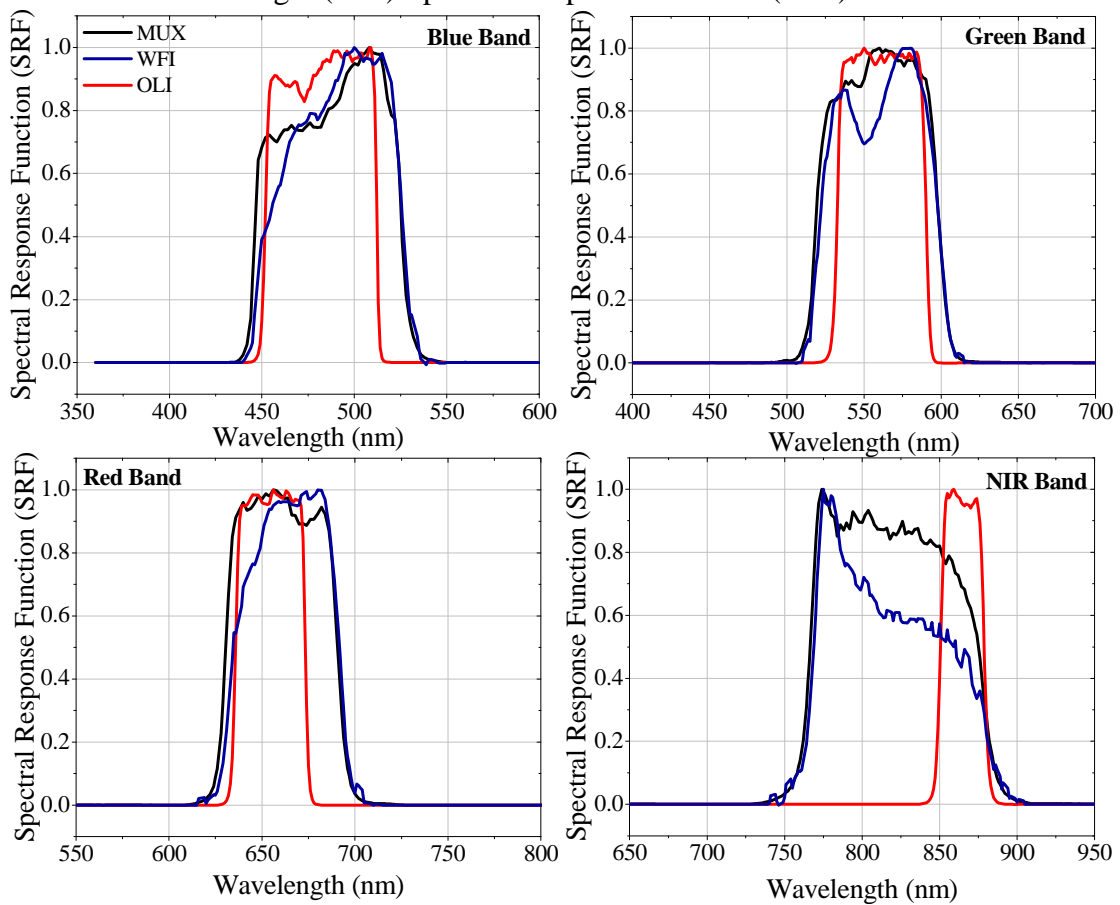
2.2.1. Spectral Response Function

Earth Observation sensors systems detect the energy (radiation) that is emitted or reflected by the object or scene being observed in certain bands of the electromagnetic spectrum. Spectral bands are often simplified in terms of Full Width at Half Maximum (FWHM) bandwidth and central wavelength that correspond to the maximum value of the response function (PINTO et al. 2009). Earth observation sensors may be designed to operate in different bands of the electromagnetic spectrum. Spectral bands operating in the visible range (400-700 nm), for example, are very common in remote sensing satellite because they support several applications (JENSEN, 2009).

The Multispectral Camera (MUX) and Wide-Field Imager (WFI) on-board CBERS-4, for example, are sensors running in four spectral bands covering the wavelength range from blue to near infrared (from 450 nm to 890 nm) (EPIPHANIO, 2011). The Operational Land Imager (OLI) on-board Landsat-8 collects data from nine spectral bands in the visible, near infrared, and short wave infrared portions of the spectrum (from 430 nm to 2300 nm) (IRONS et al., 2012). **Figure 2.3** shows the SRF profiles of

the MUX/CBERS-4, WFI/CBERS-4 and OLI/Landsat-8 sensors. The spectral bands of MUX/CBERS-4 and WFI/CBERS-4 operate in region of the electromagnetic spectrum nearby bands 2, 3, 4 and 5 of the OLI/Landsat-8 sensor. Nevertheless, the SRF of these bands are different as can be seen in **Figure 2.3**, especially in the NIR band. These differences between two sensors caused by spectral response mismatches can be compensated by using a Spectral Band Adjustment Factor (SBAF), which takes into account the spectral profile of the target and the SRF of the two sensors under study.

Figure 2.3. Multispectral Camera (MUX), Wide-Field Imager (WFI) and Operational Land Imager (OLI) Spectral Response Function (SRF).



Source: Mishra et al. (2014a).

2.2.2. Spectral Band Adjustment Factor

Multispectral remote sensing sensor systems, such as OLI/Landsat-8 and MUX/CBERS-4, measure the intensity of electromagnetic radiation in some bands of the electromagnetic spectrum. The value of the reflectance in a specific spectral band of a sensor is calculated by integrating the SRF of the sensor with the hyperspectral reflectance profile, averaged by the respective SRF:

$$\rho_{band} = \frac{\int_0^{\infty} \rho_{\lambda} \times SRF_{\lambda} d\lambda}{\int_0^{\infty} SRF_{\lambda} d\lambda} \quad (2.24)$$

where: ρ_{band} is the averaged reflectance for each spectral band of the sensor [unitless]; ρ_{λ} is the reflectance incident on the sensor at all wavelengths (hyperspectral reflectance profile) [unitless]; and SRF is the Spectral Response Function [unitless].

Looking at **Figure 2.3**, it is clear that even for the spectral bands designed to look at same region of the electromagnetic spectrum, their response can be significantly different because their analogous spectral bands have different SRF. Thus, these differences in spectral responses must be compensated when the cross-calibration method is used because the bands may respond differently to the same intensity of electromagnetic radiation. The key parameter for this compensation is the Spectral Band Adjustment Factor (SBAF). The SBAF is calculated by taking the ratio between two respective simulated reflectances from both sensors of interest according to equation (CHANDER et al., 2013b):

$$SBAF_{band} = \frac{\rho_{\lambda,ref}}{\rho_{\lambda,cal}} \quad (2.25)$$

where: $\rho_{\lambda,ref}$ and $\rho_{\lambda,cal}$ is the simulated TOA reflectance for the reference sensor and the sensor to be calibrated, respectively.

After algebraic manipulation of **Equation 2.24** and **Equation 2.25**:

$$SBAF_{band} = \frac{\int_0^{\infty} \rho_{\lambda} \times SRF_{\lambda,ref} d\lambda}{\int_0^{\infty} SRF_{\lambda,ref} d\lambda} \times \frac{\int_0^{\infty} SRF_{\lambda,cal} d\lambda}{\int_0^{\infty} \rho_{\lambda} \times SRF_{\lambda,cal} d\lambda} \quad (2.26)$$

The differences between both sensors caused by spectral response mismatches can be compensated by using a SBAF, taking into account the spectral profile of the target and the SRF of the sensors. The spectral profile is obtained by prior knowledge of the spectral signature of the target. Teillet et al. (2001), for example, used measurements of surface spectral reflectance and atmospheric aerosol optical depth available for the

Railroad Valley Playa, Nevada (RVPN) and Niobrara, Nebraska (NIOB) test sites to calculate the SBAF. For each test site, these data were used as inputs to a radiative transfer code to compute the TOA reflectance. On the other hand, Chander et al. (2013b) have applied the Hyperion/EO-1 measurements to derive the spectral signature of the target (TOA reflectance).

2.2.3. Image Pair

The basic principle (or idealized conditions) of cross-calibration is that two sensors should make identical measurements when they view the same ground target, at the same time, with the same spatial and spectral responses and the same viewing geometry (CHANDER et al. 2013c). However, all these “ideal” conditions rarely occur simultaneously, then, it is essential to apply a series of thresholds to set the measurements and adjusting the data in a comparable scale. For example, even if the same ground target is imaged at a same day by two instruments, sun-angle and off-nadir viewing geometry differences can occur between acquisitions.

Nevertheless, it is necessary to be careful when choosing the pair (or pairs) of images that will be used to perform the cross-calibration procedures. The first issue is related to the time interval between the two images. If the pair of images is acquired almost simultaneously it is possible to assume that the surface and the atmospheric conditions did not change significantly during the two image acquisitions. Teillet et al. (2001) considered this assumption to perform the cross-calibration of the sensor Thematic Mapper (TM) on-board Landsat-5 satellite (TM/Landsat-5) with the well-calibrated ETM+/Landsat-7 as a reference. This was possible because the image pairs were acquired only 10 to 30 min apart during the tandem configuration period.

The second issue is related to the type of surface chosen for calibration. In this sense, it is advisable to use images that contain spatially uniform areas and some isotropic characteristics (PINTO et al., 2013a). By choosing images with these characteristics it is not necessary to correct (or make minimal corrections) due to differences between the solar illumination geometries conditions (solar angle) and observation geometry (viewing angle) of the two sensors. Furthermore, it facilitates and possibly decreases the uncertainties in the cross-calibration procedure. Thome et al. (2003), for example, used

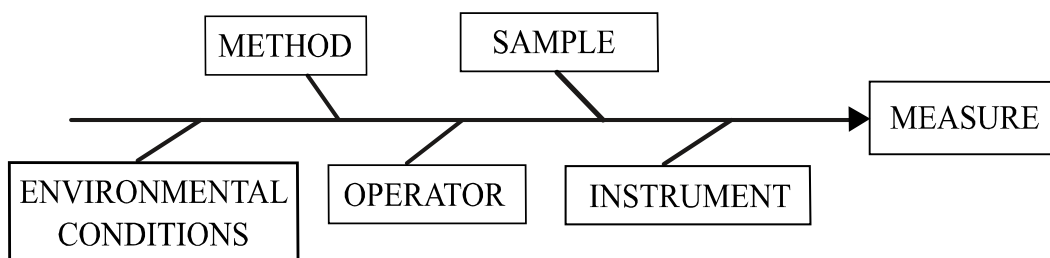
the Railroad Valley Playa in north central Nevada to calibrate the sensors on-board Earth Observer (EO-1) satellite and other Earth resources sensors taking as reference the ETM+/Landsat-7.

2.3. Evaluation of Uncertainties

Measured values are always approximate. Every measurement of physical quantities has intrinsic uncertainties in their assessments. Variability in the results of repeated measurements occurs because variables that can affect the measurement result are impractical to hold constant, even in precisely controlled conditions. Then, when reporting the measurement result of a physical quantity, it is essential giving some quantitative indication of the quality of the result (JCGM, 2008a). Therefore, the uncertainties of measurements are estimated. In metrology, “uncertainty of measurement” is a term used as a quantitative measure of accuracy.

The total uncertainty of a measurement is found by the combination of the entire contributing uncertainties component. Measurement uncertainties can be originated by the measuring instrument, by the measurement method, by the item being measured, by the environmental conditions, by the operator and by other sources. In **Figure 2.4** is presented the cause and effect diagram, showing sources of uncertainty associated with the measurement process.

Figure 2.4. Factors that influence the measurement process.



The conventional method for the uncertainties evaluation is described in the Guide to the Expression of Uncertainty in Measurement ISO (International Organization for Standardization), also known as the ISO-GUM method (ABNT and INMETRO, 2003; JCGM, 2008a). In some situations, however, the ISO-GUM method is inappropriate and an alternative approach is applying the Monte Carlo simulation method (JCGM, 2008b).

2.3.1. ISO-GUM Method

Every experimental estimation of uncertainty should take into account both, the data statistical fluctuation and the experimental aspects of the measurement. Evaluation of measurement uncertainties are classified into Type A and Type B (MENDES and ROSÁRIO, 2005; VUOLO, 1996). Type A uncertainty is estimated using statistics, usually by calculation of an estimated standard deviation from a set of repeated measurements. Quantification of other uncertainty sources requires the exercise of judgment using every relevant information available about the possible variability of the measurand (Type B - aspects of the experiment). This could be information, for example, from past experience of the measurements, from environmental conditions, from calibration certificates, from manufacturer's specifications, from published information, and from common sense. This classification of uncertainties, Type A and Type B, is done only to indicate the two different ways of evaluating uncertainty components. Such division is not intended to indicate that there is difference in the components nature. Once the uncertainties sources have been classified, Type A and Type B uncertainties are treated identically thereafter.

The measurements of physical quantities can be classified into two categories: direct and indirect measures. The direct measures are those that have been obtained directly through a measuring instrument. For example, when using a scale to measure the value of an object mass, we actually do a direct measure of its mass. Indirect measures are those that are obtained from a mathematical expression that relates the quantity of interest with other quantities, for example, the reflectance factor (see **Equation 2.7**).

In the case of direct measurements, the repeatability uncertainty is evaluated from the N replicate measurements. From these measurements it is calculated the mean value and the standard deviation of the mean, given by the standard deviation divided by the square root of the sample size, N . In most cases, the best available estimate of the expectation or expected value of a quantity that varies randomly and for which N independent observations have been obtained is the arithmetic mean. The standard deviation of the mean is the statistical uncertainty of the quantity (Type A).

On the other hand, in the indirect measurements it is applied the statistical treatment known as propagation of uncertainty. In this case, the quantity of interest is not measured directly, but it must be calculated from other quantities:

$$g = f(a, b, c, \dots) \quad (2.27)$$

where: g is the quantity of interest obtained indirectly, defined in terms of other physical quantities a, b, c, \dots , that have uncertainties associated with them.

When the input quantities from **Equation 2.27** are correlated (or dependent) the appropriate expression for the uncertainty of g is (VUOLO, 1996; JCGM, 2008a; ABNT e INMETRO, 2003; HELENE e VANIN, 1981; BEVINGTON and ROBINSON, 2003):

$$\sigma_g^2 = \left(\frac{\partial g}{\partial a}\right)^2 \times \sigma_a^2 + \left(\frac{\partial g}{\partial b}\right)^2 \times \sigma_b^2 + \left(\frac{\partial g}{\partial c}\right)^2 \times \sigma_c^2 + \dots + COV \quad (2.28)$$

where: $\frac{\partial g}{\partial a}$, $\frac{\partial g}{\partial b}$ and $\frac{\partial g}{\partial c}$ are the partial derivatives related the dependence of the quantity g relative the primary quantities a, b, c, \dots , respectively (also referred to sensitivity coefficients); $\sigma_a, \sigma_b, \sigma_c, \dots$ are the uncertainties of the primary quantities a, b, c, \dots , respectively; and COV represent the dependencies between primary quantities a, b, c, \dots :

$$COV = 2 \times \left(\frac{\partial g}{\partial a}\right) \times \left(\frac{\partial g}{\partial b}\right) \times cov_{a,b} + 2 \times \left(\frac{\partial g}{\partial a}\right) \times \left(\frac{\partial g}{\partial c}\right) \times cov_{a,c} + 2 \times \left(\frac{\partial g}{\partial b}\right) \times \left(\frac{\partial g}{\partial c}\right) \times cov_{b,c} + \dots \quad (2.29)$$

where: $cov_{a,b}, cov_{a,c}, cov_{b,c}, \dots$ are the estimated covariance associated with a and b, a and c , and b and c, \dots respectively. If the variables a, b, c, \dots are uncorrelated the covariance is equal to zero. The correlation coefficient, r , is a measure of the relative mutual dependence of two variables (a, b), equal to the ratio of their covariances ($cov_{a,b}$) to the positive square root of the product of their variances (σ_a^2 and σ_b^2):

$$r_{a,b} = \frac{cov_{a,b}}{\sqrt{\sigma_a^2 \times \sigma_b^2}} \quad (2.30)$$

The process for evaluating the uncertainties of the results of a measurement through ISO-GUM method may be summarized in eight steps as following (ABNT and INMETRO, 2003; JCGM, 2008a; PONZONI et al. 2015):

- 1) In the majority of experiments, the quantity of interest is measured indirectly according **Equation 2.27**. Then, the first step to evaluate the uncertainty is to determine the mathematical expression, which should contain all quantities that can contribute to the final uncertainty of the measurement result.
- 2) Determine the estimated value of all input quantity $a, b, c...$ from **Equation 2.27**. This estimation may be based on the statistical analysis of series of observations.
- 3) Evaluate the uncertainty of each input quantity defined in the previous step $a, b, c...$ from **Equation 2.27**. This uncertainty may be assessed by statistical analysis of a series of observations (Type A evaluation of uncertainty) or by other means (Type B evaluation of uncertainty).
- 4) Evaluate the covariances associated with all input estimates that are correlated.
- 5) Calculate the result of the measurement, that is, the estimate of the measurand, through the mathematical expression using the input quantities calculated in step 2.
- 6) The next step is to determine the final uncertainty of the measurement result using the propagation of uncertainty procedure (**Equation 2.28**). It is necessary taking into account the uncertainties and the covariance associated with the input quantities determined in step 3 and 4, respectively.
- 7) All uncertainty is associated with a confidence interval. In general, the uncertainty of the measurement result is expressed by one standard deviation (1σ), with a 68.27% confidence level, known as "standard uncertainty" (see **Table 2.1**). However, in some cases it is necessary to provide a higher confidence level. In this case it is determined the expanded uncertainty, which is obtained by multiplying the final uncertainty by a coverage factor, typically

ranging from 2 to 3. The coverage factor is dependent on the effective degrees of freedom for a confidence required of the interval. The Welch–Satterthwaite equation may be used to calculate an approximation to the effective degrees of freedom (ABNT e INMETRO, 2003; JCGM, 2008a).

Table 2.1. Value of the coverage factor and the level of confidence assuming a normal distribution.

Level of confidence (%)	Coverage factor
68.27	1.000
90.00	1.645
95.00	1.960
95.45	2.000
99.00	2.576
99.73	3.000

Source: Mendes and Rosário (2005)

- 8) Report the result of the measurement together with its final standard uncertainty or expanded uncertainty.

The CEOS (Committee on Earth Observation Satellite) Working Group on Calibration and Validation (WGCV) mission is to ensure long-term confidence in the accuracy and the quality of Earth Observation data and products and provide a forum for exchange information about calibration, validation, coordination, and cooperative activities (CEOS WGCV, 2016). CEOS WGCV has established a quality assurance strategy to facilitate interoperability of Global Earth Observations systems. This strategy is based upon a set of key operational guidelines derived from “best practices” for implementation by the community. The QA4EO (Quality Assurance Framework for Earth Observation) has been completed and endorsed by CEOS and is recommended for implementation and use throughout the GEOS community. One of the reference documents is known as “*A guide to expression of uncertainty of measurements*”, which describes briefly the ISO-GUM method (FOX, 2010).

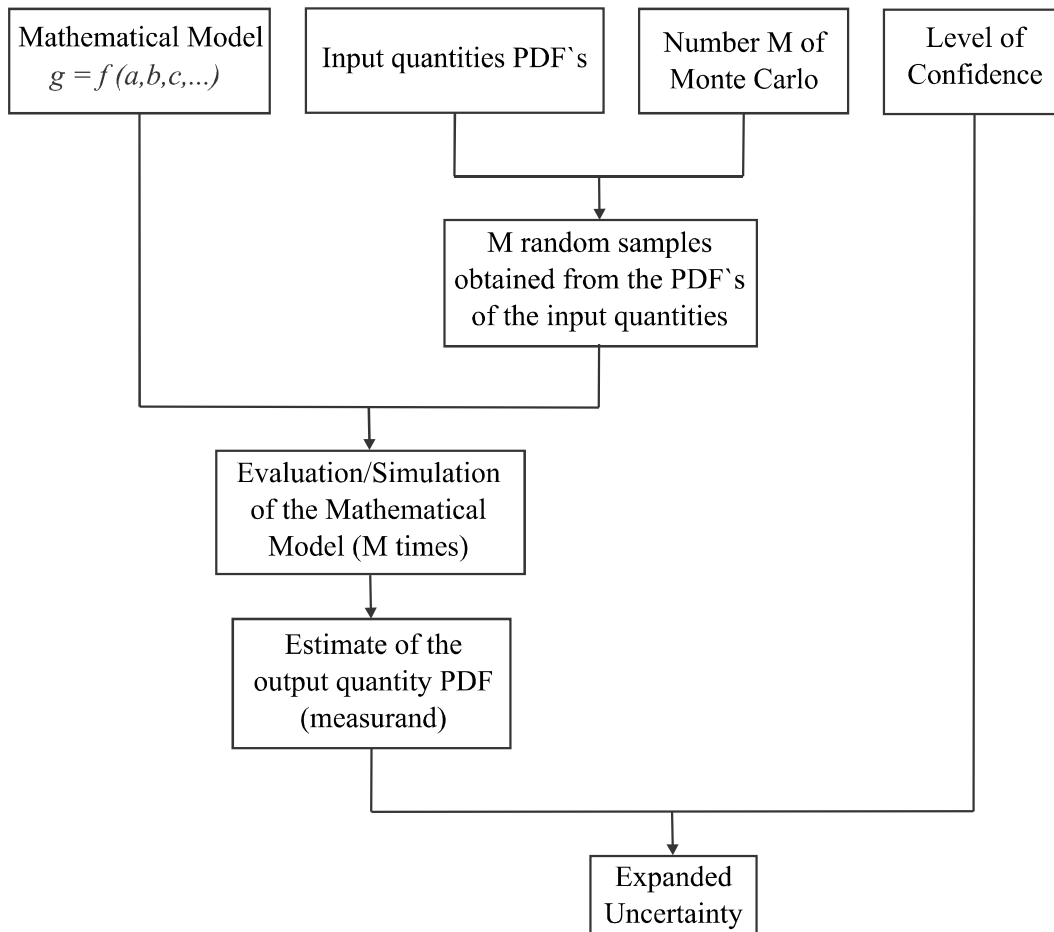
It is evident that ISO-GUM method is widely used in the calibration of the Earth observation sensors. However, there are some limitations related to the ISO-GUM uncertainty framework, like (JCGM, 2008b): (i) linearization of the model provides an inadequate representation; (ii) assumption of Gaussian distribution of the measurand; (iii) calculation of the effective degrees of freedom. Therefore, in some situations where

the model is nonlinear or complex or the model does not allow an analytical solution and/or the probability distribution of the measurand is not Gaussian, it is necessary to use alternative methods.

2.3.2. Monte Carlo Simulation Method

Currently, the Monte Carlo method is recognized as an alternative by the Joint Committee for Guides in Metrology (JCGM) of the Bureau International des Poids et Mesures (BIPM) and it was included in the GUM, since 2008 as a supplement (JCGM, 2008b). The Monte Carlo method is a computational algorithm that depends on random and repeated sampling to obtain approximate results. This method is based on random numbers generation for each primary quantity, according to their probability distribution function (PDF) and propagated through a mathematical model of measurement (BEVINGTON and ROBINSON, 2003; JCGM, 2008b; PINTO et al., 2016b). This method uses the concept of probability distributions propagation of input quantities (prior information). This propagation consists of assuming a distribution for each input quantity (uniform distribution, normal or triangular, for example). Then, these distributions are propagated M times (where M is iterations number) by a mathematical model of measurement, and a new distribution is generated as a result. Monte Carlo simulation as an implementation of the propagation of distributions is shown diagrammatically in **Figure 2.5**.

Figure 2.5. The propagation and summarizing stages of uncertainty evaluation using Monte Carlo method to implement the propagation of distributions.



Source: Adapted from JCGM (2008b).

The Monte Carlo method propagates the PDFs instead of only the uncertainties of the input quantities as performed with the traditional ISO-GUM uncertainty framework. The Monte Carlo approach is known as the propagation of distributions method and the ISO-GUM technique as the propagation of uncertainty method (**Equation 2.28**). The usual conditions for the application of the propagation law of uncertainty do not apply in the Monte Carlo simulation. In this context, the Monte Carlo is more universal than the ISO-GUM approach and, according to Cassette et al. (2015), it gives richer information than the traditional approach.

The Monte Carlo is a method widely used in metrology, but its application in absolute radiometric calibration work is relatively new. Pinto et al. (2013b), for example, applied the method to assess uncertainties in the simulation of the Tuz Gölü reflectance factor (reference surface located in Turkey) for each of the TM/Landsat-5 spectral bands.

Recently, Chen et al. (2015) used the Monte Carlo statistical method to estimate the overall absolute radiometric calibration uncertainty and to understand the relationship between the uncertainties brought on by various factors and the overall uncertainty.

2.4. Fitting

In several situations it is necessary to represent the experimental data by some functional expression. The basic problem is to find the best-fit function for an experimental data. The Method of Least Squares is probably the most popular technique to determine the best-fit to data. In this method the unknown parameters are estimated by minimizing the square of the difference between the experimental data and the fitting function, considering the uncertainty:

$$Q = \sum \left(\frac{y_i - f(x_i)}{\sigma_{y_i}} \right)^2 = \textit{minimum} \quad (2.31)$$

where: Q is the error; (x_i, y_i, σ_{y_i}) is experimental data set (x_i is the independent variable; y_i is the dependent variable, usually obtained experimentally; and σ_{y_i} is the uncertainty of y_i); and the $f(x_i)$ is the best-fit function.

In the Method of Least Squares the parameters a, b, c, \dots of the function $f(x_i)$ must be such as to minimize the error, E . Candidates for minimum point are those for which are set to zero the partial derivatives of E with respect to each of the parameters:

$$\left. \frac{\partial E}{\partial a} \right|_{\hat{a}, \hat{b}, \hat{c}, \dots} = 0 ; \left. \frac{\partial E}{\partial b} \right|_{\hat{a}, \hat{b}, \hat{c}, \dots} = 0 ; \left. \frac{\partial E}{\partial c} \right|_{\hat{a}, \hat{b}, \hat{c}, \dots} = 0 \quad (2.32)$$

This results in a system of equations that must be solved in order to find the unknowns parameters a, b, c, \dots , of the fit function $f(x_i)$. The Method of Least Squares only works with the uncertainty in the y-axis (σ_{y_i}), and the independent variable x_i is considered free of uncertainty. However, in practice the variable x_i may also have an associate uncertainty, and when it is significant, it is possible to accomplish a procedure that makes the propagation of the x-axis (σ_{x_i}) uncertainty for the y-axis (through the uncertainty propagation rules similar to those shown in **section 2.3.1**) (HELENE and VANIN, 1981).

After the function has been set, it is necessary to evaluate the fitting quality. The Goodness of Fit of a statistical model describes how well it fits into a set of observations. There are different criteria to evaluate a model fitting. The value of χ_{red}^2 (reduced chi-square), for example, can be used for this purpose. The value of χ_{red}^2 indicates the disagreement between the observed values and the values expected under a statistical model, taking into account the uncertainties.

If $f(x)$ is the fit function to a set of n data points (x_i, y_i, σ_i) , the value of χ^2 (chi-square) is defined as the following equation:

$$\chi^2 = \sum_{i=1}^n \left(\frac{y_i - f(x_i)}{\sigma_i} \right)^2 \quad (2.33)$$

where: y_i is the measurement of the quantity y , usually obtained experimentally when the quantity x is x_i ; σ_{y_i} is the uncertainty of y_i .

The χ_{red}^2 statistic is simply the chi-squared divided by the number of degrees of freedom:

$$\chi_{red}^2 = \frac{\chi^2}{\nu} \quad (2.34)$$

where: ν is the number of degrees of freedom. If n is the sample size and p is the number of parameters, then, $\nu = n - p$

A detailed interpretation of the χ_{red}^2 values can be obtained in Bevington and Robinson (2003) and Drogg (2007). In general, a “good” fitting should have value of χ_{red}^2 close to one. A “bad” fitting will present value significantly larger than one. A very low value of χ_{red}^2 has several possible meanings. It could mean, for example, that the uncertainties were over-estimated. With the experimental data of **Figure 2.6a**, a straight line can be fit, but it is clear that the line is not proper to describe such feature points. In this case, the model used should be reviewed. Another hypothesis would be the underestimation of uncertainty. In **Figure 2.6b** the fitting parabola is more feasible than the adjusted straight line in **Figure 2.6a**. In **Figure 2.6c**, the agreement between the

experimental points and the fitted line is very good; however, the fitting quality is bad. If the uncertainties are correct, the situation is quite improbable: it is extremely unlikely that the points align so well straight if the uncertainties are so great. In this case, it is much more likely that uncertainties have been over-estimated.

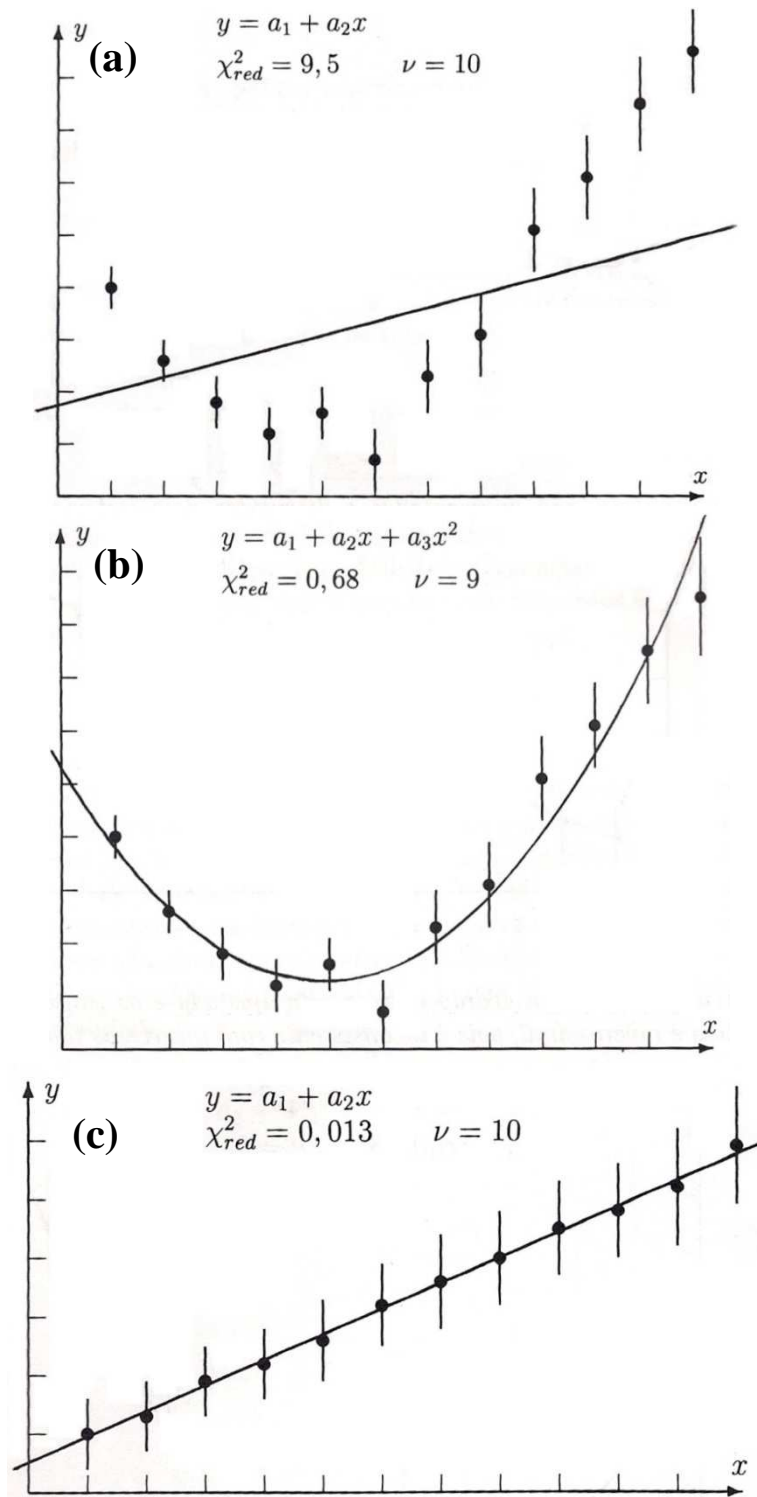
The coefficient of determination (*R*-squared) indicates the proportionate amount of variation in the response variable *y* explained by the independent variables *x* (BEVINGTON and ROBINSON, 2003). Its value is in the range from 0 to 1. An *R*-squared value of 1 indicates that 100% of the *y* variation is explained by the variability of *x*. The closer the *R*-squared is to zero, the smaller the indication that the variables are correlated. In general, the larger the *R*-squared more variability is explained by the model. Note that, unlike chi-square, the *R*-squared does not take into account the associated uncertainties. *R*-squared is the proportion of the total sum of squares explained by the model:

$$R^2 = \frac{SS_{reg}}{SS_{total}} = 1 - \frac{SS_{error}}{SS_{total}} \quad (2.35)$$

where: SS_{reg} is the regression sum of squares, also called the explained sum of squares; SS_{total} is the total sum of squares, proportional to the variance of the data; and SS_{error} is the sum of squares of error, also called the residual sum of squares. If y_i is the observed values of the dependent variable, \bar{y} is the mean of the observed data, and f_i is the fitted value, then the coefficient of determination is:

$$R^2 = \frac{\sum_{i=1}^n (f_i - \bar{y})^2}{\sum_{i=1}^n (y_i - \bar{y})^2} = 1 - \frac{\sum_{i=1}^n (y_i - f_i)^2}{\sum_{i=1}^n (y_i - \bar{y})^2} \quad (2.36)$$

Figure 2.6. In (a) the line fitted to the experimental points is implausible because it is inconsistent with the points and their uncertainties. In (b) the parabola fitted to the experimental points is quite feasible, which means that the quality of fit is good. In (c) the good agreement between the line fitted and the experimental points is improbable as it is incompatible with the uncertainties so great.



Source: Vuolo (1996).

3 MATERIAL AND METHODS

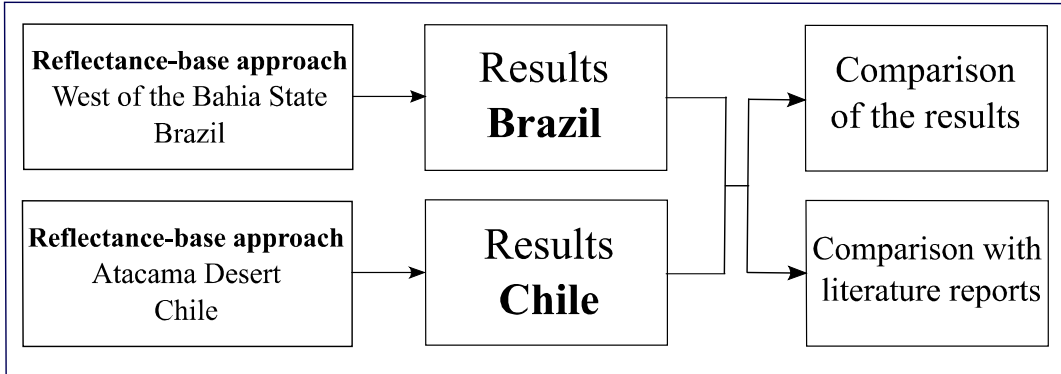
This present work aimed to develop a methodology to estimate the uncertainties inherent in the absolute radiometric calibration of Earth observation sensor after launching, in the region of the visible, near-infrared and short wave-infrared of the electromagnetic spectrum. The analysis and calculation of uncertainties were conducted for two methods of absolute calibration: reflectance-based approach and cross-calibration method.

The reflectance-based approach was performed using four different reference surfaces: (i) west part of the Bahia State, Brazil; (ii) Atacama Desert, Chile; (iii) Algodones Dunes, USA; and (iv) South Dakota State University (SDSU) site, USA. The cross-calibration method was performed using two different Earth's surfaces: (i) Libya-4, Africa; and (ii) Atacama Desert, Chile. Therefore, six independent calibrations have been performed, providing independent results that were compared in relation to the value of the radiometric calibration coefficient and the associated uncertainty. In addition, the calibration has been validated using cross-calibration techniques.

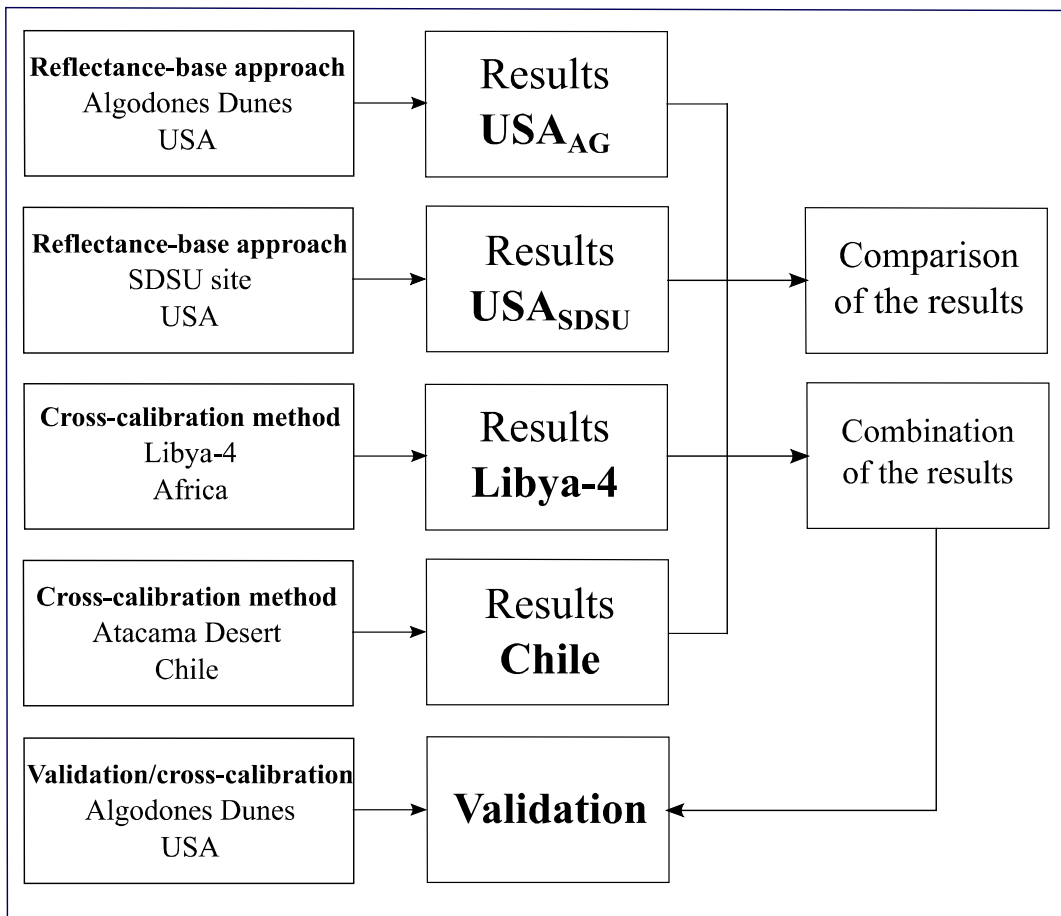
In order to assess the methodology, the OLI/Landsat-8 and MUX/WFI/CBERS-4 sensors were utilized. The reflectance-based approach calibration conducted in Brazil and in Chile occurred, respectively, on July, 2014 and August, 2014, before the launch of CBERS-4 on December 7th, 2014. Thus, the calibration using these two reference surfaces (Brazil and Chile) has been performed with OLI/Landsat-8. The other two remaining reflectance-based approach calibration in Algodones Dunes and in SDSU site, have been executed with MUX/CBERS-4 and WFI/CBERS-4. Furthermore, the two methods of cross-calibration using Libya-4 and Atacama Desert have been accomplished also with MUX/CBERS-4 and WFI/CBERS-4 sensors, taking as reference the OLI/Landsat-8 sensor. Lastly, an evaluation of radiometric consistency (validation) was performed between MUX/WFI/CBERS-4 and the well calibrated over time ETM+/Landsat-7. The general work flowchart is shown in **Figure 3.1**. In the next session some characteristics of these mentioned sensors are described.

Figure 3.1. General work flowchart.

OLI/Landsat-8



MUX and WFI/CBERS-4



3.1. Earth Observation Sensors: OLI/Landsat-8 and MUX/WFI/CBERS-4

The Landsat program provides the longest continuous space-based record of the Earth's surface. Landsat program data present a unique record of the land surface and its change over time (ROY et al., 2014). As mentioned earlier, the success of any remote sensing program depends on the knowledge of the radiometric properties of the sensor from

which the data will be available. A great example of that is the Landsat program, whose radiometric characteristics has been evaluated and updated continuously (THOME et al. 1997; MARKHAM et al., 2004; HELDER et al., 2008; CHANDER et al., 2009; MARKHAM et al., 2012; CZAPLA-MYERS et al., 2015).

The Landsat Data Continuity Mission (LDCM) was launched on February 11st, 2013 and it was renamed Landsat-8 after the transition from the National Aeronautics and Space Administration (NASA) to the United States Geological Survey (USGS) (IRONS et al., 2012). Landsat-8 is the latest platform in the 40-year Landsat series of satellites. The platform carries two sensors payloads: the Operational Land Imager (OLI), and the Thermal Infrared Sensor (TIRS). Here just OLI/Landsat-8 will be focused. The characteristics of this sensor are summarized in **Table 3.1**.

Table 3.1. Technical characteristics of the sensor OLI on-board Landsat-8.

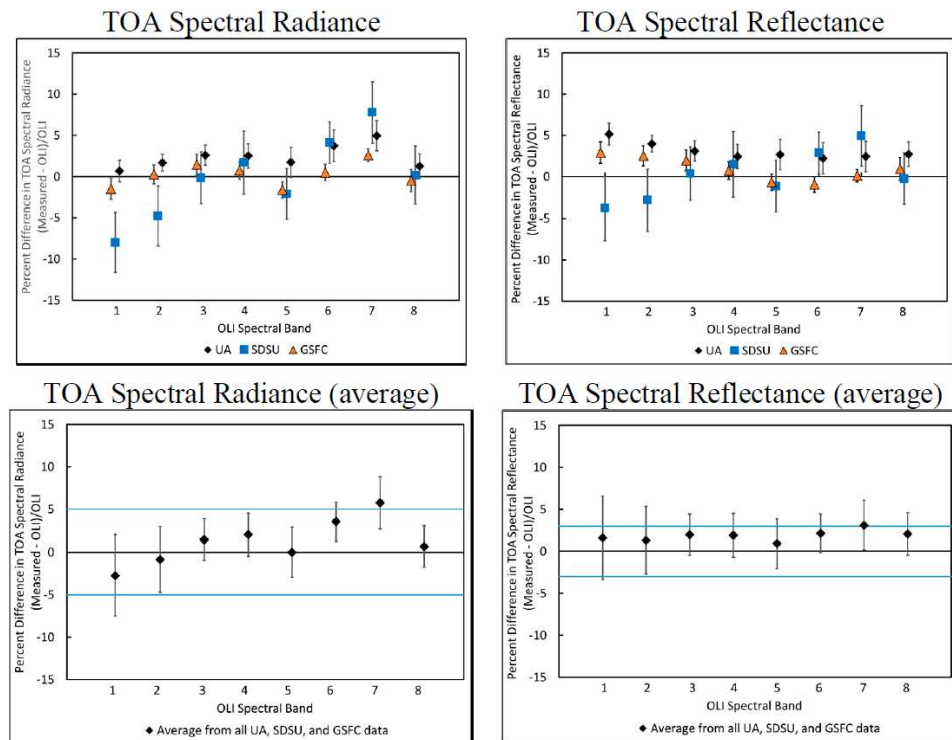
Characteristic	OLI
Technique	Pushbroom
Altitude	705 km
Swath Width	185 km
Field of View (FOV)	15°
Spectral Bands (µm)	B1: 0.433 – 0.453 (Coastal aerosol) B2: 0.450 – 0.515 (Blue) B3: 0.525 – 0.600 (Green) B4: 0.630 – 0.680 (Red) B5: 0.845 – 0.885 (Near Infrared - NIR) B6: 1.560 – 1.660 (SWIR 1) B7: 2,100 – 2.300 (SWIR 2) B8: 0.500 – 0.680 (Panchromatic) B9: 1.360 – 1.390 (Cirrus)
Spatial Resolution	30 m (15 m panchromatic band – B8)
Temporal Resolution	16 days
Radiometric Resolution	12 bits

Source: Irons *et al.* (2012)

The OLI/Landsat-8 sensor has rigorous radiometric performance requirements and it is required to produce data calibrated to an uncertainty less than 5% in terms of absolute, at-aperture spectral radiance, and to an uncertainty less than 3% in terms of top-of-atmosphere spectral reflectance for each spectral band (IRONS et al., 2012;

ROY et al., 2014; CZAPLA-MYERS et al., 2015). Recently, the radiometric calibration of the OLI/Landsat-8 was checked using a combination of techniques including the reflectance-based approach, the Radiometric Calibration Test Site (RadCaTS) and a cross-calibration with ETM+/Landsat-7 (CZAPLA-MYERS et al., 2015). The results achieved by the authors from reflectance-based approach for both the TOA spectral radiance and the TOA reflectance are shown in **Figure 3.2**. In the bottom row of **Figure 3.2**, the data from the three field teams are averaged into one final data set. In the case of both TOA spectral radiance and the TOA reflectance, OLI/Landsat-8 is generally in agreement with the ground-based results, respecting the design specifications (5% and 3%, respectively). The only band that is just out of specification was band 7 (2.2 μm), which typically has a very low signal at both the desert and vegetated sites.

Figure 3.2. A summary of in situ results from the University of Arizona (UA), South Dakota State University (SDSU), and Goddard Space Flight Center (GSFC) for TOA spectral radiance (top left) and reflectance (top right) for OLI/Landsat-8. The uncertainty bars are the 1σ standard deviation of the measurements by each team. Note that band 9 (cirrus) is excluded from the results due to an extremely low Signal-to-Noise Ratio (SNR) in the ground measurements. The bottom row shows the results for TOA spectral radiance (bottom left) and reflectance (bottom right) when the ground-based results from all three teams are consolidated into one data set and then compared to OLI/Landsat-8. The uncertainty bars in the average graphs are the 1σ standard deviation of the average from all three teams.



Source: Czapla-Myers et al. (2015).

The incorporation of Brazil into a long-term remote sensing program has begun with the establishment of the China-Brazil Earth Resources Satellite (CBERS) program. The overall purpose of the program is the observation and the monitoring of the Earth's resources and environment (EIPHANIO, 2009). Images generated by CBERS have been used in several applications, such as deforestation monitoring, water resources control, urban growth, agricultural development, land-use mapping and monitoring and soil occupation (YULIANG et al., 2009; FONSECA et al., 2014). CBERS images can be downloaded for free on INPE CBERS's website (INPE, 2016). According to Ambinakudige et al. (2009) CBERS images could fill the data gaps in Landsat images for land-cover studies.

On December 7th, 2014 the CBERS-4 was successfully launched from the Taiyuan Satellite Launch Center. The CBERS-4 satellite has a sun-synchronous orbit with an altitude of 778 km. The local solar time at the equator crossing is approximately 10:30 a.m. CBERS-4 carries four cameras in the payload module (EIPHANIO, 2011): (a) Panchromatic and Multispectral Camera (PAN); (b) Multispectral Camera (MUX); (c) Infrared System (IRS); (d) Wide-Field Imager (WFI). In the present work, the two sensors of which Brazil is responsible, MUX and WFI, will be the focus.

MUX/CBERS-4 is a multispectral camera with four spectral bands covering the wavelength range from blue to near infrared (450 nm to 890 nm) with ground resolution of 20 m and ground swath width of 120 km. The MUX/CBERS-4 is a National Institute for Space Research (INPE) instrument designed and developed at Opto Eletrônica S. A., São Carlos, São Paulo, Brazil. The main function of the MUX/CBERS-4 is to maintain continuity with the previous CBERS sensors (EIPHANIO, 2011). This sensor ensures global coverage at a standard spatial resolution every 26 days.

Just as the MUX/CBERS-4, the WFI/CBERS-4 camera was also developed in Brazil. The WFI/CBERS-4 has a significant improvement in characteristics compared to previous WFI sensor. The WFI/CBERS-4 is also a multispectral camera, running on four spectral bands from blue to near infrared. Its ground resolution is 64 m at nadir, without losing the revisit capacity of 5 days, due to the large Field of View (FOV) of $\pm 28.63^\circ$. **Table 3.2** shows a summary of the MUX/CBERS-4 and WFI/CBERS-4 characteristics.

Table 3.2. Technical characteristics of the sensors MUX/WFI/CBERS-4.

Characteristic	MUX	WFI
Technique	Pushbroom	Pushbroom
Altitude	778 km	778 km
Swath Width	120 km	866 km
Field of View (FOV)	$\pm 4^\circ$	$\pm 28.63^\circ$
Spectral Bands (μm)	B5: 0.450 – 0.520 (Blue) B6: 0.520 – 0.590 (Green) B7: 0.630 – 0.690 (Red) B8: 0.770 – 0.890 (NIR)	B13: 0.450 – 0.520 (Blue) B14: 0.520 – 0.590 (Green) B15: 0.630 – 0.690 (Red) B16: 0.770 – 0.890 (NIR)
Spatial Resolution	20 m	64 m (nadir)
Temporal Resolution	26 days	5 days
Radiometric Resolution	8 bits	10 bits

Source: Epiphanio (2011)

The main difference characteristic between the sensors is the Field of View (FOV). The FOV is constant for remote sensing sensors. As a result, the effective pixel size on the ground is larger at the extremities of the scan than at nadir (RICHARDS, 2013). Due to this fact, ideally, during calibration it is preferable that the site be centered in the image or at an angle that does not cause large distortions. If the field of view is η and the pixel dimension at nadir is p then its dimension in the scan direction at a scan angle φ is:

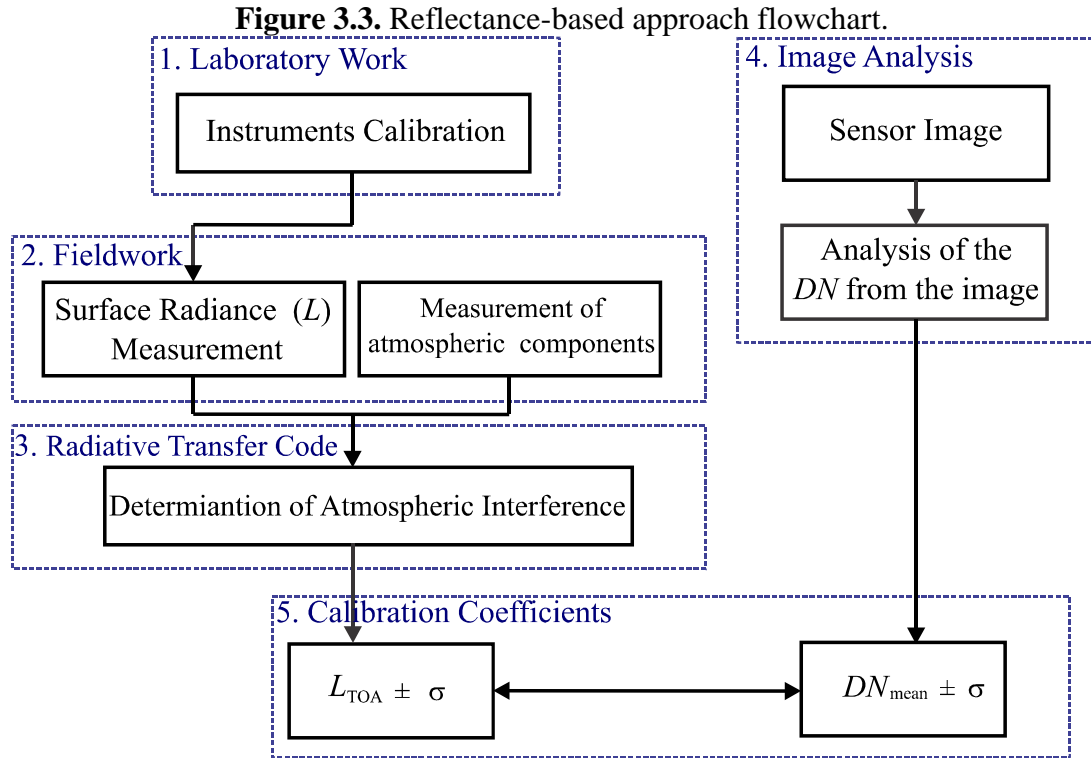
$$p_\varphi = \eta \times h \times \sec^2 \varphi = p \times \sec^2 \varphi \quad (3.1)$$

where: h is the flight altitude. Its dimension across the scan line is $p \times \sec^2 \varphi$. For small values of φ the distortion in pixel size is negligible. However, the effects can be quite evident for sensors images with large field of view.

3.2. Reflectance-Based Approach

As mentioned previously, the reflectance-based approach relies on ground-based measurements (surface reflectance and characterization of the atmosphere) of a selected surface during the sensor overpass. The results of the ground measurements are input into a radiative transfer code, which predicts at-sensor radiance that is compared to the digital number recorded by the sensor. In general, a calibration mission using the

reflectance-based approach includes five steps: (i) laboratory work; (ii) fieldwork; (iii) application of the radiative transfer code; (iv) image analysis; and (v) determining the calibration coefficients. In **Figure 3.3** is illustrated the calibration procedure adopted. In the following sections each of these steps is described.



3.2.1. Test Sites Overview

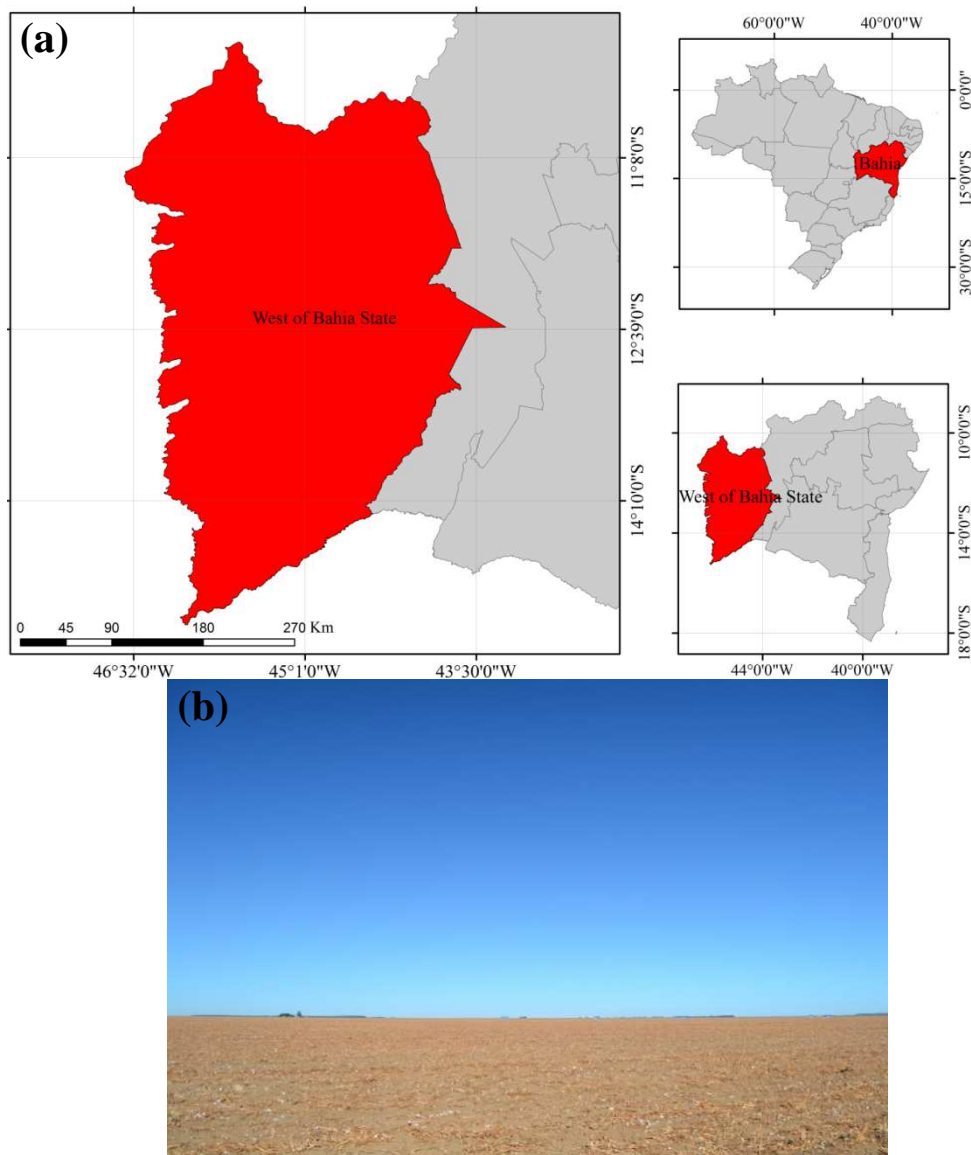
As presented in **Figure 3.1**, the reflectance-based approach was carried out in four different reference surfaces. The first surface was located in Brazil, where there are no “ideal” calibration sites, as established by WGCV (Working Group of Calibration and Validation) of the CEOS (Committee on Earth Observation Satellites). However, considering some limiting administrative and other operational and financial restrictions, it is necessary to maintain efforts to identify national surfaces that minimally reach the needs of the Brazilian Space Program. In Brazil, the sensors absolute calibration works have been conducted in the west part of the State of Bahia (northeast region of Brazil).

According to Ponzoni et al. (2006), Ponzoni et al. (2008) and Pinto et al.(2012) the region presents the following characteristics: (i) lower cloud cover indices during winter time; (ii) relative high reflectance; (iii) the agricultural schedule that is followed every year makes possible to find a specific reference surface with the same characteristics at

a specific time of year; (iv) the reference surfaces present enough isotropy during the calibration time; (v) the region is one of the most arid regions of the Brazilian territory; (vi) as the reference surfaces are located within farms, there are a lot of roads, thus the access is very easy.

The selected surfaces are constituted by bare soil (quartz sand) that presents partially the requirements to be used in absolute calibration missions. The coordinates of the test site are $12^{\circ}23'S$ latitude and $46^{\circ}05'W$ longitude, located at an altitude of 850 m. **Figure 3.4** shows the location of the study area in Brazil and a picture to illustrate the reference surface area.

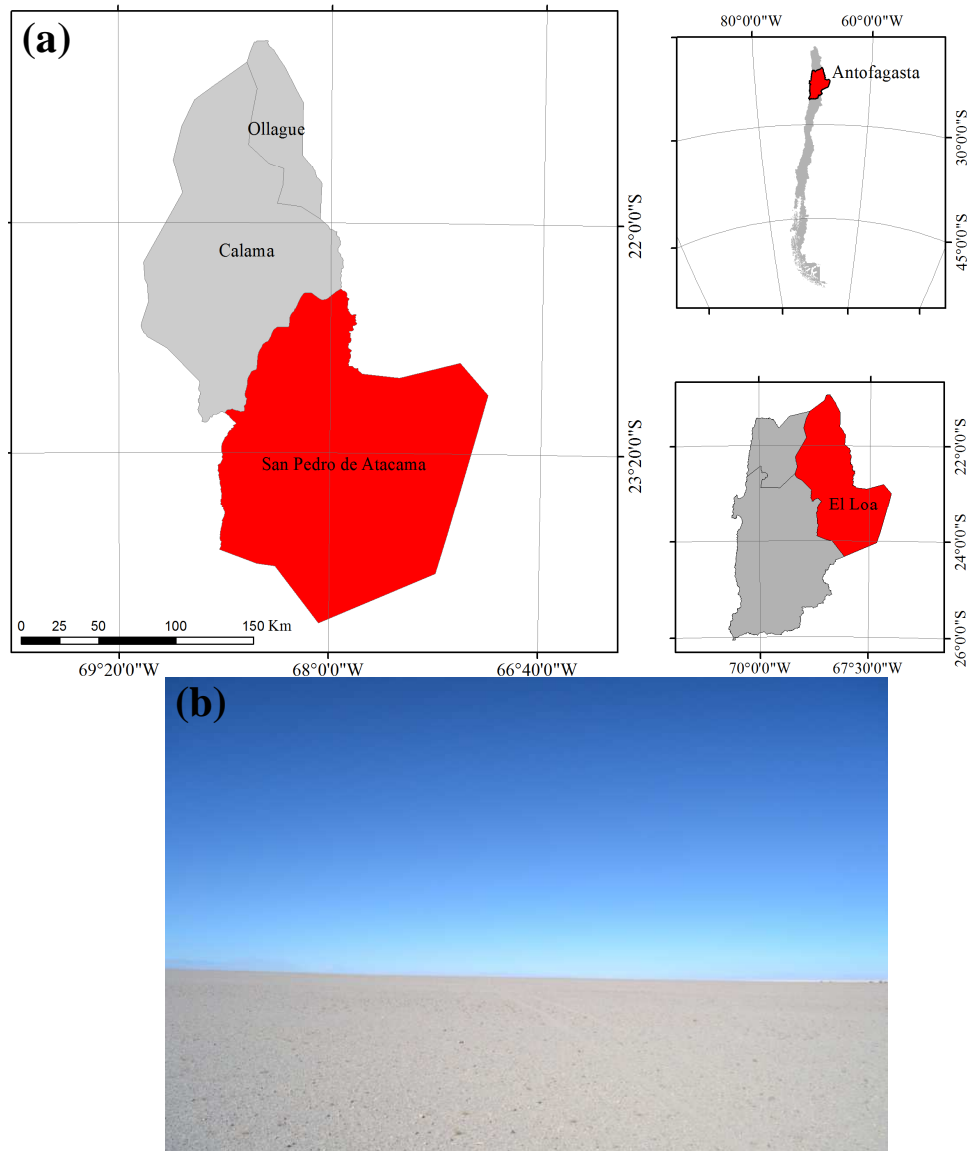
Figure 3.4. In (a) Location of the study area in Brazil; and (b) picture of the reference surface.



The second surface was located in Chilean territory, which theoretically presents favorable characteristics for absolute calibration missions. According Cosnefroy et al. (1996) deserts areas are good candidates for the assessment of optical satellite sensors calibration. The selected reference surface was an area in the Atacama Desert, located in the São Pedro do Atacama region, in the north of Chile (**Figure 3.5**).

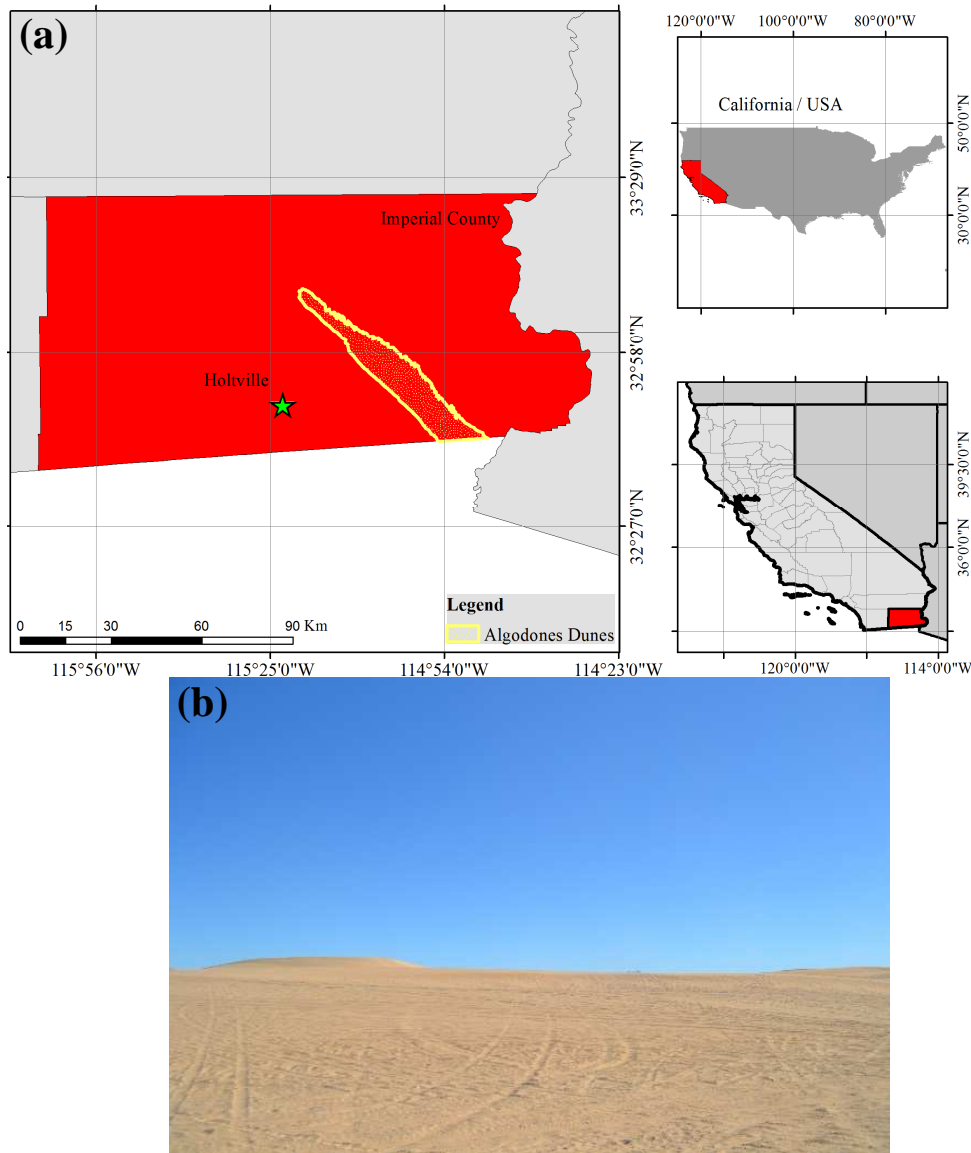
This was the first time that Atacama Desert was explored for calibration purposes. The region presents average elevation of 2400 m. Stretching 600 miles (1000 kilometers), the Atacama is known as the driest place on Earth (VESILIND, 2003). As observed by Houston and Hartley (2003), the Atacama region presents low precipitation levels. In the station situated at Peine city the annual precipitation was 23.1 mm between 1977 and 1991 (HOUSTON and HARTLEY, 2003). The geographical coordinates of the reference surface are 23°08'S latitude and 68°03'W longitude. The surface is ~28 km south of San Pedro de Atacama city and easily accessible by road (PINTO et al., 2015).

Figure 3.5. In (a) Location of the study area in Chile (Atacama Desert); and (b) picture of the reference surface.



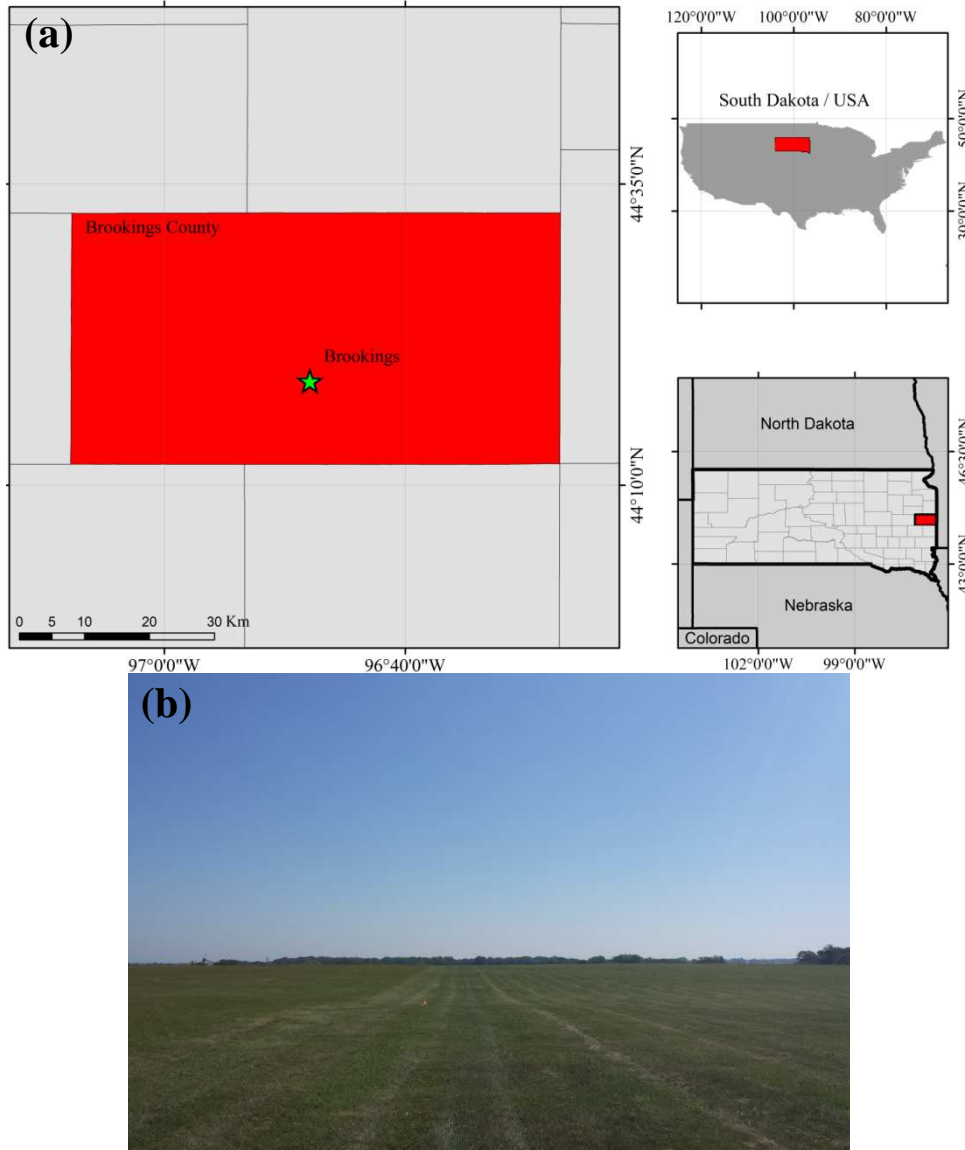
The third surface selected was located at the Imperial Sand Dunes Recreation Area (commonly referred to as Algodones Dunes). Algodones Dunes is located in the southwestern portion of the United States of America, in the state of California at latitude $32^{\circ}54'N$ and longitude $115^{\circ}07'W$ (**Figure 3.6**). The area provides positive characteristics for calibration purposes, including high-reflectance, sufficiently large size, low amount of atmospheric aerosols, good temporal stability, sufficient spatial stability and easy accessibility (PINTO et al., 2016a).

Figure 3.6. In (a) Location of the Algodones Dunes; and (b) picture of the reference surface.



Finally, the fourth selected surface for application of reflectance-base approach was a vegetative site known as the site of the South Dakota State University (SDSU). The SDSU site is located in Brookings, South Dakota, USA (**Figure 3.7**). It is a surface located at an altitude of 505 m and it is surrounded by a larger grass area. The grass on the actual calibration site is routinely maintained during the spring, summer and fall months so that changes in the bidirectional reflectance distribution function (BRDF) due to the structure of the grass is minimized (CZAPLA-MYERS et al., 2015).

Figure 3.7. In (a) Location of the SDSU site; and (b) picture of the reference surface.



From 23 to 26 July 2014 a field campaign was conducted at Marechal Rondon farm, west of Bahia state, Luís Eduardo Magalhães city, Brazil. From August 19 to 22, 2014, a joint field campaign was conducted at Atacama Desert and it involved three different institutions: Universidad de Chile, Servicio Aerofotogramétrico (SAF) from Chile, and National Institute for Space Research (INPE) from Brazil. INPE team collected the data used in this work. From 9 to 13 March 2015 a joint field campaign was conducted at Algodones Dunes and involved five different teams: Arizona Remote Sensing Group (RSG), South Dakota State University (SDSU), Rochester Institute of Technology (RIT), University of Lethbridge and Goddard Space Flight Center (GSFC). The SDSU team collected the data used in this work. Ultimately, one fieldwork was performed at

SDSU site on 3rd September, 2015. **Table 3.3** presents a summary containing the dates of the four campaigns and the date that satellite overpassed the surface.

Table 3.3. Summary of the dates of the four calibration campaigns using the reflectance-based approach.

Surface	Campaign	Satellite	Date satellite overpassed
West of Bahia State (Brazil)	23 rd to 26 th July 2014	Landsat-8	25 th July 2014
Atacama Desert (Chile)	19 th to 22 nd August 2014	Landsat-8	21 st August 2014
Algodones Dunes (USA)	9 th to 13 rd March 2015	CBERS-4	9 th March 2015
SDSU Site (USA)	3 rd September 2015	CBERS-4	3 rd September 2015

3.2.2. Laboratory Measurements

In order to analyze the conditions of the instruments and their respective contributions to the final uncertainty in the measurements, experiments were performed in an optics and radiometry laboratory called *Laboratório de Radiometria e Caracterização de Sensores Eletroópticos* (LaRaC) of the Institute for Advanced Study (IEAv). The LaRaC was set to provide a controlled environment to perform radiometric measurements. The laboratory does not have windows; its walls and ceiling are painted with flat black paint to avoid reflections and also it presents environmental control of temperature and relative humidity. The laboratory equipment's are powered by a stabilized voltage source. During the measurements the temperature and humidity information was collected by a digital thermohygrometer from Delta Ohm. In general, measurements were made with the temperature ranging from 18 to 21°C and relative humidity between 50 and 70%.

The experiments were performed at LaRaC on three occasions: (Lab 1) before the fieldwork in Brazil; (Lab 2) after the fieldwork in Brazil, which fortunately also served as laboratorial step before the fieldwork in Chile; (Lab 3) after the fieldwork in Chile. The instruments utilized during fieldworks in Brazil and in Chile belong to the National Institute for Space Research (INPE). The instruments used in the fieldwork in Algodones Dunes and in SDSU site belong to South Dakota State University and the

calibration data of these instruments were provided by the SDSU Image Processing Laboratory. According to Helder et al. (2012) the instruments calibration were performed by the University of Arizona Remote Sensing Group laboratory (RSG Lab).

Here, only the lab-work carried out in LaRaC will be described. As mentioned in **section 2.1.1**, it is necessary a spectroradiometer and a reference panel to calculate the surface reflectance factor. Then, during the LaRaC experiments the Spectralon reference panel from Labsphere (LABSPHERE, 2009) and the spectroradiometer FieldSpec Pro ASD (ASD, 1999; ASD, 2002) used during the fieldwork were assessed with similar equipment belonging to LaRaC. The LaRaC instruments have recently been calibrated with manufacturers and, therefore, they were considered as standards.

Spectroradiometer Calibration

To perform the calibration of the spectroradiometer FieldSpec Pro ASD, an integrating sphere was used as a standard instrument. The function of an integrating sphere is to spatially integrate radiant flux (LABSPHERE, 2016). According to Chen (1997) the principle of an integrating sphere source is that a source of light is placed inside a sphere, which is coated internally with a standard diffusing white coating; the irradiance of any position of the surface due to light reflected from the rest of the sphere is the same and is directly proportional to the radiation emitted by the lamp light source.

The integrating sphere source model belonging to LaRaC is the USS 2000 Labsphere (LABSPHERE, 2005). The coating of the sphere is Spectrafect. This sphere has an internal diameter of 50 cm and a 20 cm diameter output port. It is equipped with four tungsten halogen lamps; all the lamps are driven with constant current to have the same color temperature of 3000 K, but they have different powers: two 45 W lamps, one 100 W lamp and other 150 W lamp. The 100 W lamp is equipped with a variable aperture shutter in order to modulate the output radiance. Each of the lamps can be turn on and off independently from the others. The overview of the experimental setup is shown in **Figure 3.8**.

Figure 3.8. Overview of the experimental setup to characterize and assess the spectroradiometer. In (a) the FieldSpec Pro ASD used in fieldwork; and (b) the FieldSpec Pro ASD belonging to the LaRaC laboratory, which remains all the time in the laboratory, therefore, is an instrument considered as a reference.



The radiance levels of the integrating sphere source are determined according to the combination of the lamps inside the sphere. Here, five configurations were carried out as presented in **Table 3.4**. The first step in the experimental procedure was turned on the spectroradiometer ASD FieldSpec Pro and all lamps (level 1) of the integrating sphere. The FieldSpec and the integrating sphere source lamps need a warm up period before measurements acquisition. This period is suggested to be roughly 30 minutes to allow the detectors and temperatures inside to stabilize (LABSPHERE, 2005; ASD, 2002). Then, a half hour time was set before beginning the measurements, as recommended by the manufacturers.

Table 3.4. Lamps settings in the integrating sphere source.

Level	Lamps	Total Power (W)
1	150, 100, 45 and 45 W	340
2	150, 45 and 45 W	240
3	45 and 45 W	90
4	45 W	45
5	All lamps turned off	0

Successive measurements of the radiance emanating from the aperture of the integrating sphere were collected every minute during 10 minutes (total of 10 measurements). After the completion of these measurements, the 100 W lamp was turned off, setting up the second lamps combination (150 W, 45 W and 45 W – level 2), and then the same procedure was repeated. In sequence, the 150 W lamp was turned off, setting up the third configuration with both 45 W lamps (level 3). Then, one of the 45 W lamp was

turned off, creating the fourth combination (level 4). Finally, the last 45 W lamp was turned off, and the same procedure was again performed with all lamps turned off (level 5). With this procedure all five combinations of lamps (**Table 3.4**) and, consequently, the five intensities of radiance were achieved.

Reference Panel Calibration

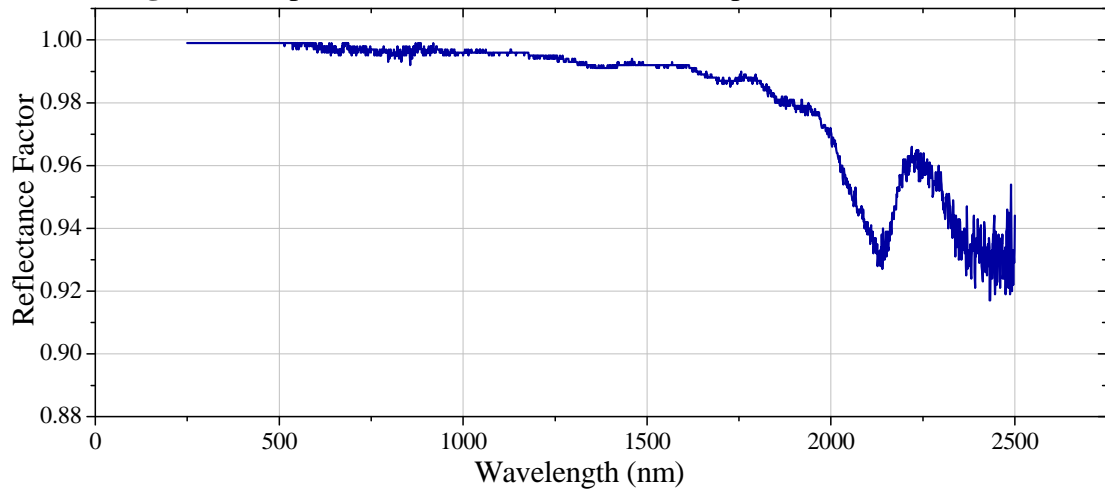
According to Thome (2001) a critical part of the reflectance retrieval is the characterization of the reference panel in laboratory. As mentioned in **section 2.1.1**, the reflectance factor (RF) is obtained indirectly by the ratio of spectral radiance reflected from a sample (target) to the spectral radiance that would be reflected by a reference panel surface, under the same geometry conditions. Therefore, the calibration of the reference panel used during fieldwork was done adopting as a reference a standard panel belonging to the LaRaC laboratory. The panel calibration purpose is to determine the panel correction factor, k_λ , from **Equation 2.7**, which is the panel reflectance factor:

$$RF_{fieldwork_panel,\lambda} = \frac{L_{fieldwork_panel,\lambda}}{L_{standard_panel,\lambda}} \times k_{standard_panel,\lambda} \quad (3.2)$$

where: $RF_{fieldwork_panel,\lambda}$ is the reflectance factor of the fieldwork panel; $L_{fieldwork_pane,\lambda}$ is the radiance of the fieldwork panel; $L_{standart_panel,\lambda}$ is the radiance of the standard panel from laboratory under the same specified conditions of illumination and viewing; $k_{standart_panel,\lambda}$ is the standard panel correction factor, provided by the manufacturer (see **Figure 3.9**). Note that for simplify the equation the angular dependence of the RF was omitted.

Here the standard panel used was a Spectralon panel, SRT-99-120 model from Labsphere, which presents reflectance close to 100%. The spectral reflectance calibration ranged from 250 to 2500 nm (reported at 50 nm intervals) was provided by the manufacturer (LABSPHERE, 2012). The spectral reflectance of the Spectralon standard panel is presented in **Figure 3.9**. The uncertainty of the reflectance values is dependent on the wavelength, ranging between 0.001 and 0.067%.

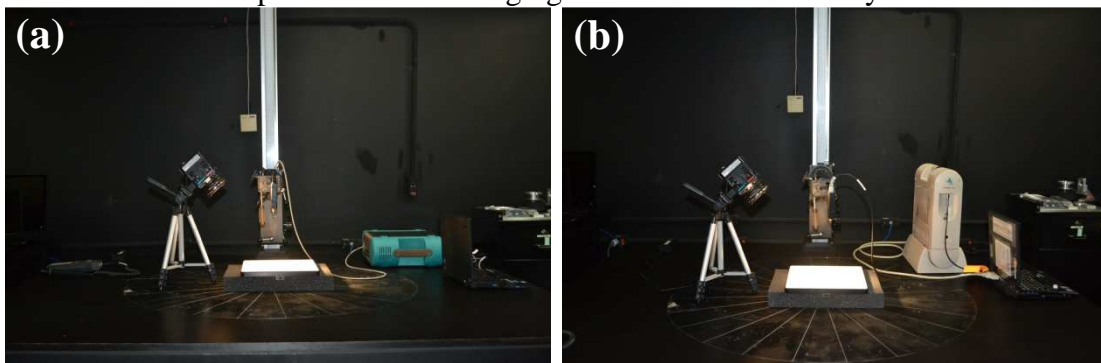
Figure 3.9. Spectral reflectance of the standard panel from LaRaC.



Source: LABSPHERE (2012).

A fixed measurement geometry was setup to determine the panel reflectance factor (see **Figure 3.10**). The illumination source was a 50 W tungsten halogen lamp set at an illumination angle of 45° . The 45° illumination angle was compatible with the sun zenith angles practiced during the field measurements. The illuminator was fixed on a tripod and positioned a distance of approximately 25 cm from the reference panel. The receiver was an ASD FieldSpec spectroradiometer set at a viewing angle of 0° from the normal of the panels (nadir view), positioned at a distance of approximately 10 cm. The overview of the experimental setup is shown in **Figure 3.10**.

Figure 3.10. Overview of the experimental setup to characterize and assess the reference panel used in fieldwork. In (a) measurements with the FieldSpec Pro ASD used in fieldwork; and (b) measurements with the FieldSpec Pro ASD belonging to the LaRaC laboratory.



The reference panel was calibrated using the procedure described by Pinto et al. (2012). Briefly, the first step in the experimental procedure was to turn on the tungsten halogen lamp and the ASD FieldSpec Pro. As mentioned, the spectroradiometer FieldSpec and the lamp need at least 30 minutes of warm-up time, then; this time frame was awaited before starting the measurements. In the next step, ten successive measurements of the standard panel reflectance factor were obtained (reference panel from LaRaC). Shortly thereafter, it was performed the same measurements with the reference panel used in fieldwork. Finally, it was again obtained measurements of the standard panel. This procedure allows verifying whether the standard panel reflectance values changed during the performance of measurements.

During the laboratory measurements all quantities were obtained from direct measurements. The direct measures are those that have been obtained directly through a measuring instrument. As described in **section 2.3**, in a series of independent observations of a certain quantity, whose distribution is symmetrical, the most likely value of quantity is the average, and its uncertainty is the average standard deviation. Thus, in the radiometric laboratory measurements the uncertainties were the statistical (Type A), related to the repeatability of the measurements.

3.2.3. Field Measurements

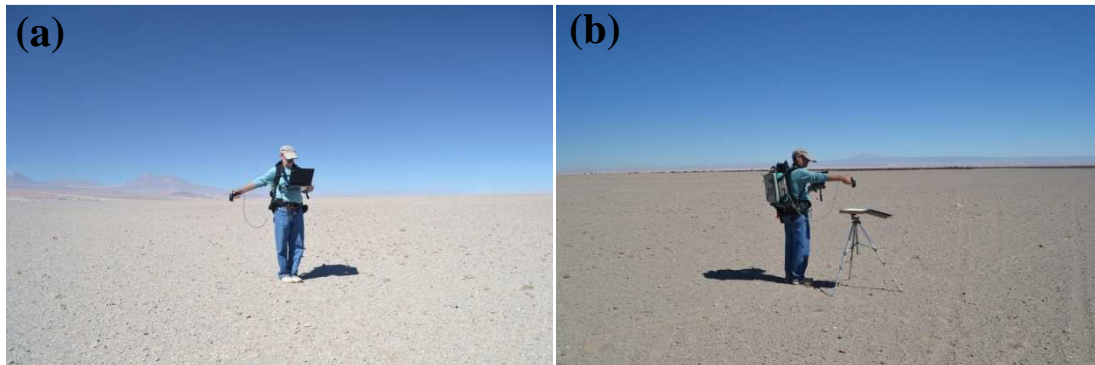
As mentioned before, the reflectance-based approach requires accurate field radiometric measurements concurrent with the overpass of the sensor. The ground based radiometric measurements involve two distinct types of measurements: those related to the surface reflectance and those related to the atmosphere characterization. Below is described how these two measurements were performed.

Reflectance Factor

The surface reflectance factor was measured using a FieldSpec Pro hyperspectral spectroradiometer from ASD (Analytical Spectral Devices), running at the spectral range from 350 nm through 2500 nm (ASD, 1999; ASD, 202). A Spectralon panel from Labsphere was used as the approximate ideal diffuse standard surface (LABSPHERE, 2012). The FieldSpec ASD was operated only by hand with the

collection unit held vertically toward the ground (about 1.3 m high), with the operator avoiding the projection of his shadow on the area measured. The FieldSpec ASD was configured to average 20 spectra per sample and it was transported across the area using a backpack device (**Figure 3.11**).

Figure 3.11. In (a) reference surface (target) measurements collection; and (b) Spectralon panel measurements. The two pictures were taken during the fieldwork in Atacama Desert, Chile. The collection in the other three fieldworks (Brazil, Algodones Dunes and SDSU site) were similar.



Within each reference surface (the size of each area is listed in the **Table 3.5**) were systematically defined points from which it was collected the radiometric data. The reference panel was kept on a tripod near the sample point in a horizontal position (**Figure 3.11b**). At the beginning of each data acquisition the FieldSpec ASD was optimized and five sample spectra of the reference panel were acquired. Next, approximately 15-25 sample spectra of the target (surface) were obtained by walking in line until the next point. Then, the reference panel was again measured by the FieldSpec ASD and five sample spectra were obtained. This procedure was performed in every set point over a period of 40-60 minutes. The corresponding reference surface measurement time, calibration dates and test site layout are listed for each campaign in **Table 3.5**.

Table 3.5. Reflectance factor measurements local time, fieldwork dates and test site layout. In gray are highlighted the dates which the satellite overpassed the region (calibration dates).

Surface	Campaign Date	Test site layout	Fieldspec ASD Acquisition time
West of Bahia State (Brazil)	23 July 2014	300 x 300 m	9:40 a.m. – 10:40 a.m.
	24 July 2014		9:40 a.m. – 10:40 a.m.
	25 July 2014		9:40 a.m. – 10:40 a.m.
	26 July 2014		9:40 a.m. – 10:40 a.m.
Atacama Desert (Chile)	19 August 2014	300 x 300 m	10:00 a.m. – 11:00 a.m.
	20 August 2014		9:40 a.m. – 10:40 a.m.
	21 August 2014		9:40 a.m. – 10:40 a.m.
	22 August 2014		9:40 a.m. – 10:40 a.m.
Algodones Dunes (USA)	9 March 2015	160 x 300 m	11:00 a.m. – 12:00 p.m.
	10 March 2015		9:40 a.m. – 10:40 a.m.
SDSU Site (USA)	3 September 2015	200 x 180 m	12:00 p.m. – 1:00 p.m.

The reference surface size is chosen according to the spatial resolution of the sensor, i.e., the size of the chosen site must be compatible with the pixel size of the sensor. Thome (2001), for example, used a rectangular reference surface of the 480 by 120 m to calibrate the ETM+/Landsat-7, TM/Landsat-4 and TM/Landsat-5 sensors. Czaplá-Myers et al. (2015) considered a 100 by 250m reference surface to calibrate OLI/Landsat-8. Here, the largest site selected was 300 by 300 m and the smaller site layout was 200 by 180 m, which is appropriate to calibrate sensors on-board CBERS-4 and Landsat-8 (or sensors with higher spatial resolution). Increasing the size of the reference surface would provide more statistical sampling, but it also requires a longer collection time. This creates complications due changes in solar zenith angle and increases the probability of changes in atmospheric conditions.

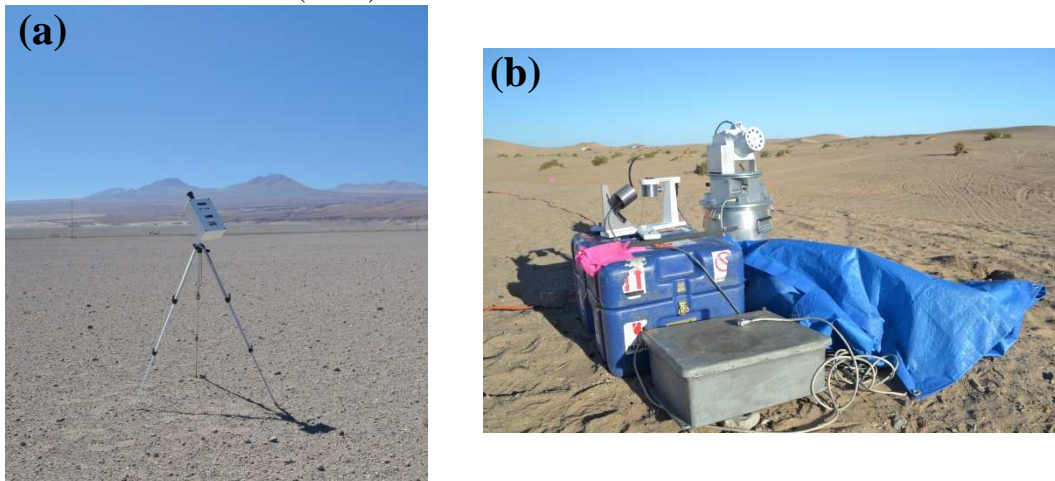
Atmospheric Characterization

The atmospheric characterization data were collected at the same time as the surface reflectance factor measurements. The atmospheric characterization in Brazil and in Chile campaigns was performed using a multi-spectral portable manual sun photometer CE317/CIMEL (LAMPARELLI et al., 2003; PINTO et al., 2015) (see **Figure 3.12a**). The CE317/CIMEL operates in five spectral bands, approximately 20 nm wide, with interference bands selected between 300-1100 nm: band 1 from 1010 to 1030 nm, band

2 from 860 to 880 nm, band 3 from 660 to 680 nm, band 4 from 430 to 450 nm and band 5 from 926 to 946 nm.

In USA campaigns (Algodones Dunes and SDSU site) the atmospheric characterization was performed using an Automated Solar Radiometer (ASR) developed and manufactured by the University of Arizona running in ten spectral bands (EHSANI et al., 1998) (see **Figure 3.12b**). The ASR operates in ten spectral bands that presents narrow bandpasses of approximately 10 nm each and are spaced fairly uniformly in the visible and near-IR regions; spectral band center were selected to avoid strong gaseous spectral absorption lines except for one placed in a water absorption band (EHSANI et al., 1998). The center wavelengths are typically 380, 400, 440, 520, 610, 670, 780, 870, 940, and 1030 nm.

Figure 3.12. In (a) the sun photometer CE317/CIMEL; and (b) Automated Solar Radiometer (ASR).



The CIMEL/CE317 and ASR measurements were performed according to the schedule presented in **Table 3.6**. The CE317/CIMEL and ASR generate a digital output signal, V_{λ} , which is linearly proportional to the solar irradiance. This can be modeled according to the Beer Law (see **Equation 2.8**). Assuming that total optical depth, τ_{λ} , remains constant over the range of airmasses, m , for which measurements are performed, a Langley plot (linearization of Beer's law - **Equation 2.12**) will yield a set of data points distributed along a straight line with slope equal the total optical depth, τ_{λ} , and intercept equal the natural logarithm of the CE317/CIMEL and ASR calibration constant, $V_{0,\lambda}$ (SCHMID and WEHRLI, 1995; ROLLIN, 2000; PINTO et al., 2015).

Table 3.6. Atmospheric measurements schedule, Julian day, and the day angle. In gray are highlighted the dates which the satellite overpassed the region (calibration dates).

West of Bahia State (Brazil)				
Date	Instrument	Acquisition time	<i>J</i>	<i>d_a</i>
23 July 2014	CIMEL/CE317	6h30 - 18h00	204	3.49
24 July 2014		8h20 - 11h10	205	3.51
25 July 2014		8h20 - 11h00	206	3.53
26 July 2014		8h25 - 10h20	207	3.55
Atacama Desert (Chile)				
19 August 2014	CIMEL/CE317	7h15 - 18h00	231	3.96
20 August 2014		9h30 - 11h30	232	3.98
21 August 2014		9h15 - 12h15	233	3.99
22 August 2014		9h30 - 11h30	234	4.01
Algodones Dunes (USA)				
9 March 2015	ASR	9h00 - 12h30	68	1.15
10 March 2015		9h00 - 12h30	69	1.17
SDSU Site (USA)				
3 September 2015	ASR	9h00 - 15h30	246	4.22

The Langley method requires determining the Sun-Earth distance, d , and the value of the relative optical airmass, m . To estimate the Sun-Earth distance was used **Equation 2.10**, where the day angle, d_a , was determined according to **Equation 2.11**. The day angle, d_a , and Julian day, J , are presented in **Table 3.6**. For the calculation of m it was used **Equation 2.9**, which depends on the surface pressure, P , and the solar zenith angle θ_z . The surface pressure in Brazil, Chile and USA sites was obtained from the weather station closest to the reference surface, from the website of the Instituto Nacional de Meteorologia (INMET), Red de Agrometeorológica del INIA (Agromet), and National Weather Service (DNs), respectively (INMET, 2016; AGROMET, 2016; NWS, 2016).

The atmospheric pressure may vary greatly during the day. Thus, it was used an average pressure in the range the measurements were performed, see **Table 3.6**. The uncertainty (standard deviation) of the pressure considered in the period was less than 0.2%, which is well below the uncertainty in the values of optical airmass, m , which is of the order of 1 to 2% (Pinto, 2011), for an optical airmass from 1 to 7. In **Figure 3.13** it can be seen

the values of the zenith angle for each measurement time with the CE317/CIMEL and ASR. The graph of the airmass as a function of the solar zenith angle is presented in **Figure 3.14**.

Figure 3.13. Solar zenith angle as a function of measuring time with the sun photometer. In (a) on 25 July 2014 in Brazil; (b) on 21 August 2014 in Atacama Desert; (c) on 9 March 2015 in Algodones Dunes; (d) on 3 September 2015 in SDSU site.

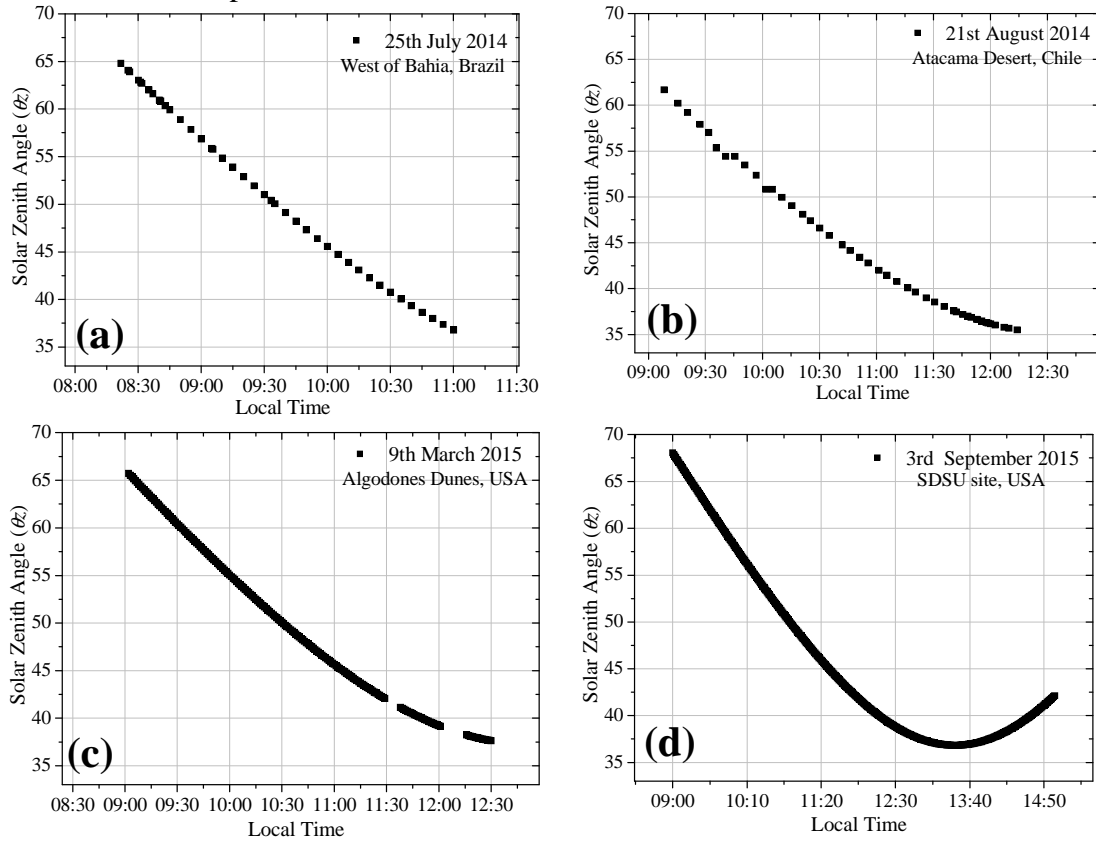
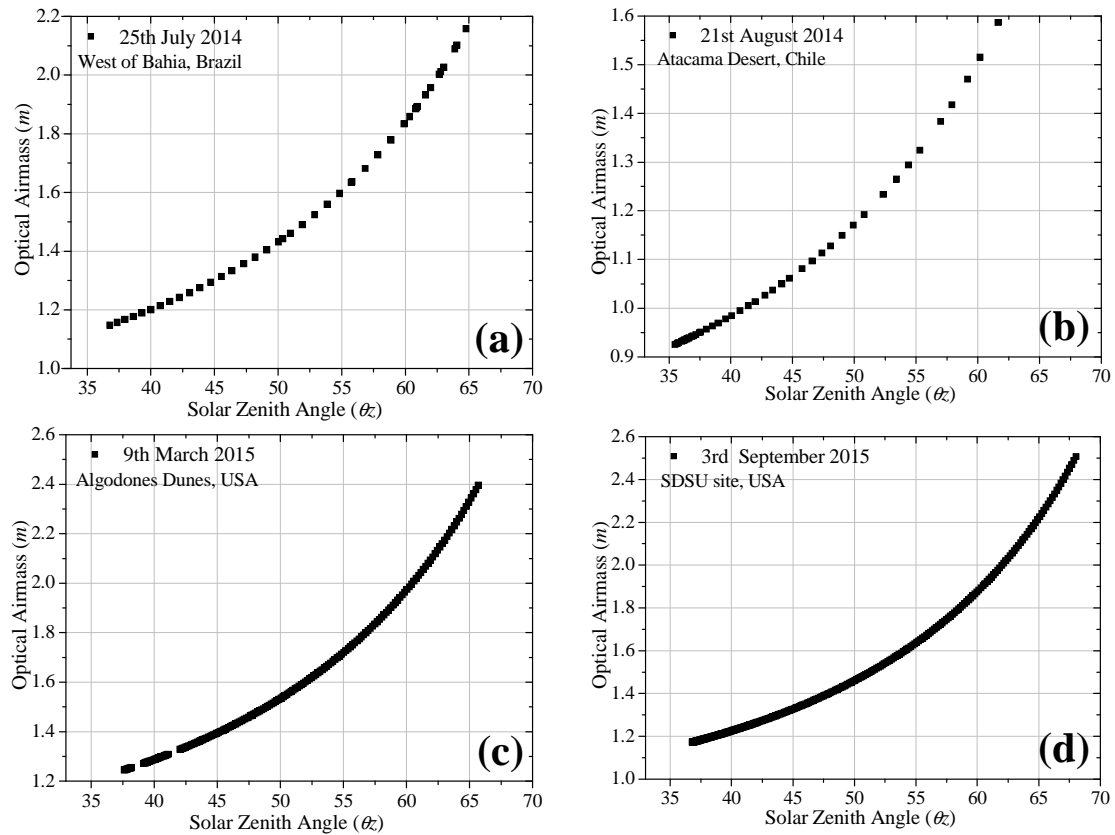


Figure 3.14. Optical airmass as a function of the sun's zenith angle. In (a) on 25 July 2014 in Brazil; (b) on 21 August 2014 in Atacama Desert; (c) on 9 March 2015 in Algodones Dunes; (d) on 3 September 2015 in SDSU site.

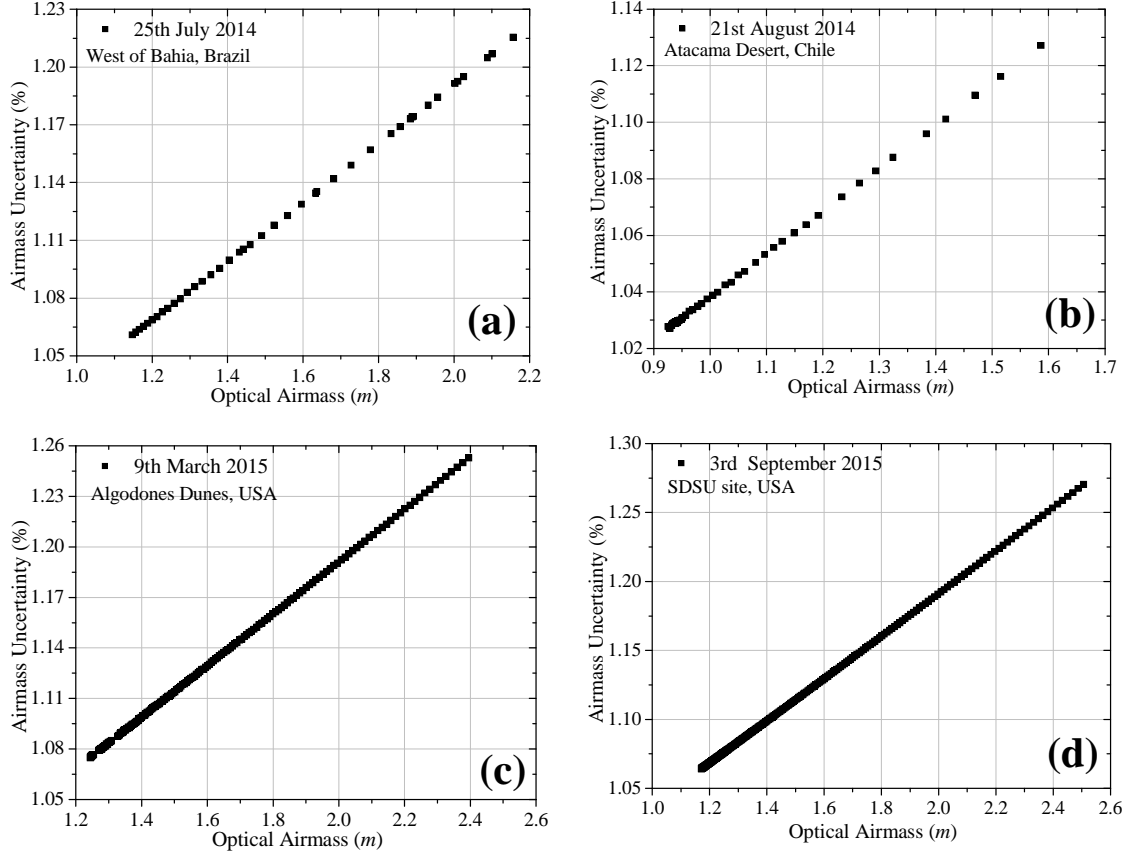


It is possible to verify in **Figure 3.13** and **Figure 3.14** that it was performed more measurements in Algodones Dunes and SDSU site, comparing to measurements taken in Brazil and in Chile. It can be explained since the ASR is an automatic sun radiometer and, therefore, measurements were taken every minute. On the other hand, the sun photometer CE317/CIMEL is a manual solar radiometer, and measurements were made at intervals of approximately five minutes.

The airmass uncertainties were determined as described in Pinto (2011), according to **Equation 3.3**. The authors consider two sources of uncertainties: (a) an uncertainty of 0.5% of the optical airmass, corresponding to the calculating of m using the **Equation 2.9**; and (b) the uncertainty related to the adjustment of the time in the CE317/CIMEL e ASR instruments. **Figure 3.15** shows the graph of the optical airmass uncertainties.

$$\sigma_m = \sqrt{(0.005 \times m)^2 + (0.00171 \times m^2 + 0.00739 \times m)^2} \quad (3.3)$$

Figure 3.15. Optical airmass uncertainties. In (a) on 25 July 2014 in Brazil; (b) on 21 August 2014 in Atacama Desert; (c) on 9 March 2015 in Algodones Dunes; (d) on 3 September 2015 in SDSU site.



The aerosol optical depth was determined using **Equation 2.13**. However, to use this equation it is necessary estimating the optical depth due to Rayleigh scattering, using **Equation 2.14**. The Rayleigh scattering uncertainty was estimated using **Equation 3.4** (PINTO, 2011). This equation is determined by the application of the ISO-GUM method (propagation of uncertainty), discussed in **section 2.3.1**.

$$\sigma_{\tau_{Rayleigh}} = \sqrt{\left(\frac{\partial \tau_{Rayleigh}}{\partial \lambda}\right)^2 \times (\sigma_{\lambda})^2 + \left(\frac{\partial \tau_{Rayleigh}}{\partial P}\right)^2 \times (\sigma_P)^2} \quad (3.4)$$

where: σ_{λ} and σ_P are, respectively, the uncertainties of wavelength λ , and the surface atmospheric pressure, P .

The aerosol optical depth uncertainty was estimated according to the following equation (PINTO, 2011):

$$\sigma_{\tau_{Aerosols, \lambda}} = \sqrt{(\sigma_{\tau_{Rayleigh, \lambda}})^2 + (\sigma_{\tau_{\lambda}})^2} \quad (3.5)$$

where: $\sigma_{\tau_{Rayleigh, \lambda}}$ and $\sigma_{\tau_{\lambda}}$ are the uncertainties of Rayleigh scattering and the total optical depth, respectively.

Aerosols were assumed to follow a power law distribution (Ångström's turbidity formula - **Equation 2.15**), also referred to as a Junge distribution. The Ångström exponent (power law exponent) is related to the average size distribution of the aerosols. Then, after the calculation of the aerosol optical depth it was performed the fitting according to the Ångström's formula, estimating the parameters called the power law exponent, α , and the unremarkable constant, β . The next step was calculating: (a) the horizontal visibility, VIS, using **Equation 2.16**; and (b) the aerosol optical depth at 550 nm, $\tau_{Aerosol, 550nm}$, applying **Equation 2.15**. The horizontal visibility uncertainty and the aerosol optical depth at 550 nm uncertainty were determined according to **Equation 3.6** and **Equation 3.7**, respectively (PINTO, 2011).

$$\sigma_{VIS} = \frac{-15 \times \sigma_{\beta}}{\beta} \quad (3.6)$$

where: σ_{β} is the uncertainty of β .

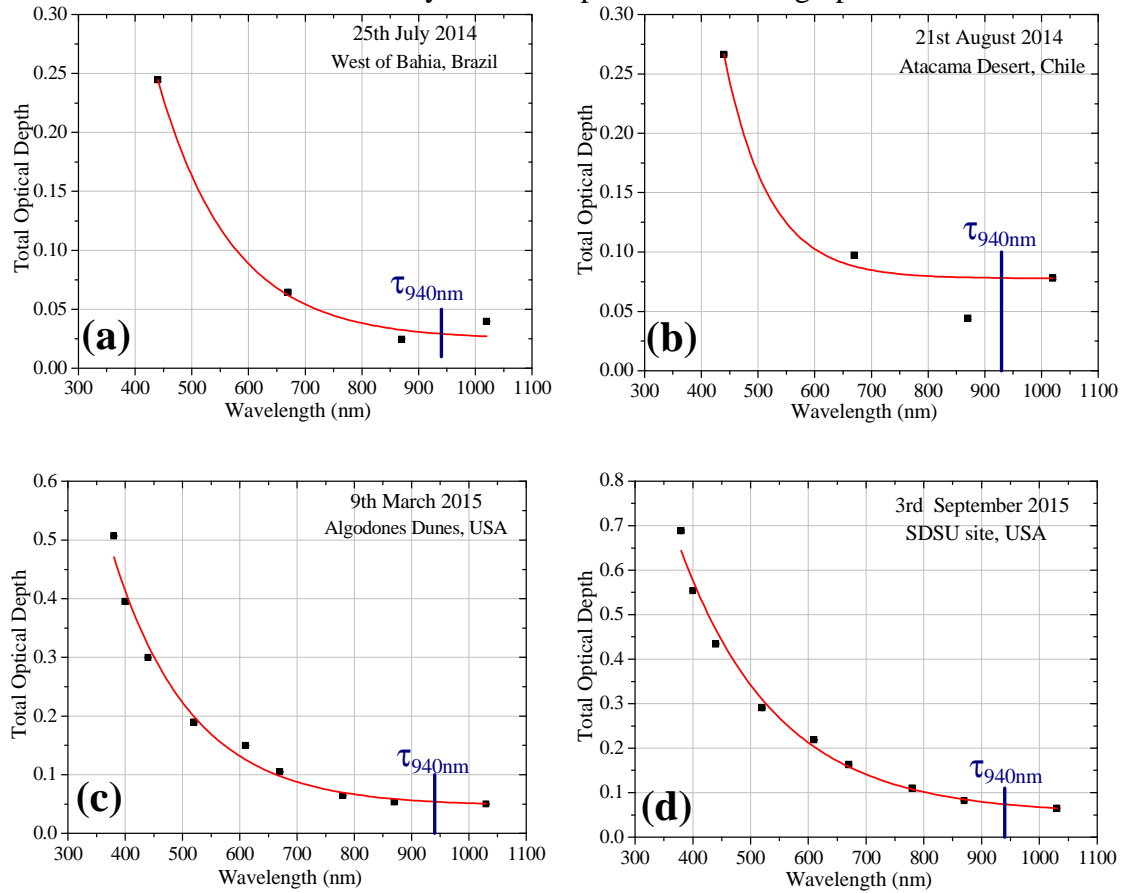
$$\sigma_{\tau_{aerosol, 550nm}} = \sqrt{\left(\frac{\partial \tau_{Aerosol, 550nm}}{\partial \beta}\right)^2 \times (\sigma_{\beta})^2 + \left(\frac{\partial \tau_{Aerosol, 550nm}}{\partial \alpha}\right)^2 \times (\sigma_{\alpha})^2} \quad (3.7)$$

where: σ_{α} is the uncertainty of α .

Lastly, the absorption by water vapor is restricted to narrow spectral bands. Therefore, the spectral range centered approximately at 940 nm was used to estimate the water vapor atmospheric content. Columnar water vapor was determined using a modified-Langley approach (**Equation 2.19**). The theoretical total optical depth at

940 nm, τ_{940nm} , was obtained by interpolation from adjacent wavelengths (adjacent spectral bands) that do not have influence of water vapor, as illustrated in **Figure 3.16**.

Figure 3.16. Total Optical depth at 940 nm. In (a) on 25th July 2014 in Brazil; (b) on 21th August 2014 in Atacama Desert; (c) on 9th March 2015 in Algodones Dunes; (d) on 3rd September 2015 in SDSU site. The uncertainties are very small comparable with the graph scale.



A modified-Langley plot will yield a set of data points distributed along a straight line whose intercept is $\ln(V_{0,940 \text{ nm}})$ and whose slope is $a \times W^b$ (**Equation 2.19**). Thus, after the application of the modified-Langley method it was possible to estimate the water vapor column abundance, W , according to equation:

$$W = \left(\frac{A}{a} \right)^{\frac{1}{b}} \quad (3.8)$$

where: A is the slope value of the straight line; and a and b are constants known beforehand related to the instrument (CE317/CIMEL and ASR).

The water vapor column abundance uncertainty was determined applying the following equation derived from ISO-GUM method (propagation of uncertainty), discussed in **section 2.3.1** (PINTO, 2011):

$$\sigma_w = \frac{1}{a} \times \frac{1}{b} \times A^{\frac{1}{b}-1} \times \sigma_A \quad (3.9)$$

where: σ_A is the uncertainty of A .

3.2.4. Radiative Transfer Code

The in-situ radiometric measurements of the reference surface and the atmosphere parameters described in the previous section were utilized to constrain the radiative transfer code that estimates the top-of-atmosphere (TOA) radiance or reflectance (see **Equation 3.10**). The atmospheric radiative transfer code adopted was the MODerate resolution atmospheric TRANsmission (MODTRAN 5.2.1) (BERK et al., 2011)

An estimate of the TOA radiance is incomplete unless accompanied by its uncertainty. According to Berk et. al (1998), the accuracy of MODTRAN is typically 2-5% (this value is related to the model accuracy). However, this accuracy is only one uncertainty source. As described in the **section 3.2.3** the atmospheric parameters and the reflectance factor surface were estimated with the associated uncertainties, therefore, it is also necessary to verify the impact of the input parameters uncertainties on MODTRAN. To achieve this goal was considered, in addition to the MODTRAN uncertainty itself (accuracy of MODTRAN), five others sources of uncertainty: (i) the reflectance factor of the surface - RF; (ii) the aerosol optical depth - AOD; (iii) the water vapor column abundance; (iv) the ozone; and (v) the horizontal visibility – VIS. All input atmospheric parameters were estimated (see previous section), with the exception of ozone, which it was used the default ozone column of MODTRAN.

$$L_{TOA_MODTRAN} = L_{TOA_MODTRAN}(RF, AOD, Water, O_3, VIS) \quad (3.10)$$

To determine the impact of the reflectance factor uncertainties on MODTRAN, all other input parameters were firstly held fixed. Then, the MODTRAN was run for two cases: (i) maximum reflectance factor (average reflectance added the uncertainty + 1σ); (ii) minimum reflectance factor (average reflectance subtracted the uncertainty - 1σ).

The next step was to determine the difference between these two results and divide it by two. The division by two is required because the uncertainty is always “plus or minus (\pm)” the mean value. The value obtained from this division would be the "sensitivity" of MODTRAN to the maximum and minimum values of the reflectance and, then, it was considered the impact of the reflectance factor uncertainties on MODTRAN.

To determine the uncertainties of the other parameters on MODTRAN (aerosol optical depth, water vapor column abundance, ozone and horizontal visibility) the same procedure was applied. The parameter of interest always varied (maximum and minimum) while the other inputs were kept fixed. After all uncertainties have been calculated the final uncertainty of the TOA radiance (or TOA reflectance) predicted by MODTRAN was estimated using **Equation 3.11**. In order to not overestimate the uncertainty was considered 2% in the accuracy of MODTRAN (BERK et. al, 1998):

$$\sigma_{MODTRAN} = \sqrt{(\sigma_{RF})^2 + (\sigma_{AOD})^2 + (\sigma_{Water})^2 + (\sigma_{O3})^2 + (\sigma_{VIS})^2 + (\sigma_{Accuracy})^2} \quad (3.11)$$

3.2.5. Image Analysis and Calibration Coefficients

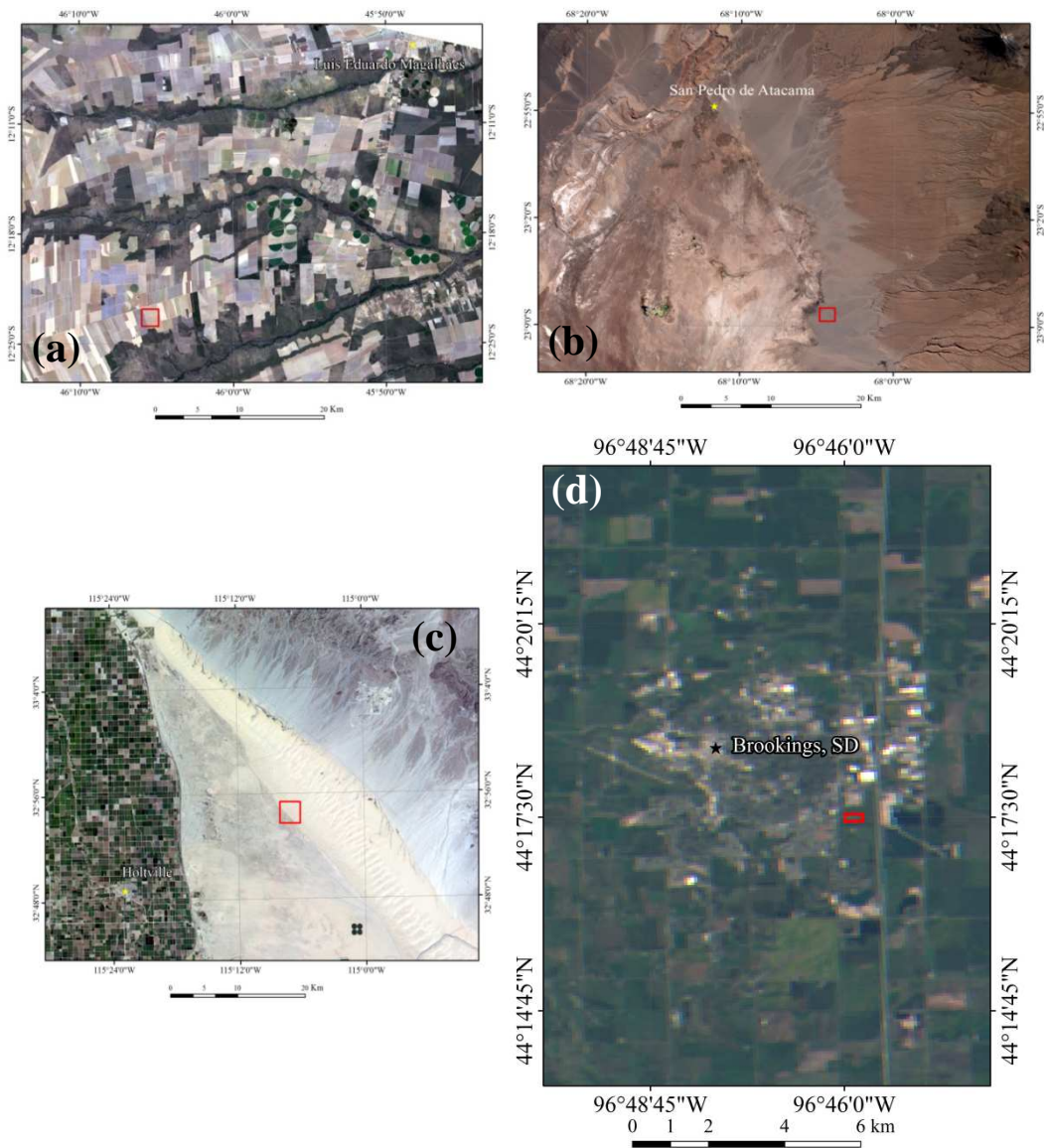
The next step necessary to determine the sensor radiometric calibration coefficients is to compare the average digital number (DN) output to the predicted radiances by MODTRAN. The average DN output is determined by averaging all pixels coinciding with the ground measurements. For example, the size of the surface site at Algodones Dunes was 160 meters by 300 meters, which guarantee a region of interest (ROI) of 8x15 pixels for the MUX’s 20 meter pixel and an ROI of 3x5 pixels for the WFI’s 64 meter. In **Table 3.7** is presented the ROI size related to each reference surface.

Table 3.7. The region of interest (ROI) related to each test site.

Surface	Sensor	Spatial Resolution	Test site layout	ROI
West of Bahia State (Brazil)	OLI	30 m (15 m PAN band)	300 x 300m	10x10 pixels (multispectral bands)
Atacama Desert (Chile)	OLI		300 x 300m	20x20 pixels (15 m PAN band)
Algodones Dunes (USA)	MUX	20 m	160 x 300 m	8x15 pixels
	WFI	64 (nadir)		3x5 pixels
SDSU Site (USA)	MUX	20 m	200 x 180 m	10x9 pixels
	WFI	64 (nadir)		3x3 pixels

The image processing steps in each spectral band of the sensor was as follows: (1) the test site characterized in the fieldwork was located in the image (see **Figure 3.17**); and (2) set up the grid (the ROI) of contiguous image windows or cells and extract the mean and standard deviation. Thus, the average DN with their respective standard deviation was calculated.

Figure 3.17. In (a) OLI/Landsat-8 image from west of Bahia State site, Brazil; (b) OLI/Landsat-8 image from Atacama Desert site, Chile; (c) MUX/CBERS-4 image from Algodones Dunes site, USA; (d) WFI/CBERS-4 image from SDSU site. The red box indicates the location of the study area.



The initial plan was to calibrate the MUX/CBERS-4 and WFI/CBERS-4 using Algodones Dunes and SDSU sites. However, during the fieldwork on SDSU site the WFI/CBERS-4 sensor was the only to acquire images of the surface. This happened because WFI/CBERS-4 sensor has a wide field of view of $\pm 28.63^\circ$ (see **Table 3.2**) and the site was not centered in the image, but at the image edge. In addition, the area of the SDSU site is small for the spatial resolution of the WFI/CBERS-4 sensor (64 meters). In fact, the area in Algodones Dunes could also be considered small to calibrate the WFI/CBERS-4 sensor, however, it is surrounded by the same type of surface (the same surface coverage). On the other hand, the SDSU site is surrounded by urban area.

As described in **section 3.1**, during calibration it is preferable that the site be centered in the image or at an angle that does not cause large distortions. Then, to avoid the effect of sensor field of view and misregistration errors in choosing the proper image pixel corresponding to the reference surface, the SDSU site was not used to calibrate the WFI/CBERS-4 sensor. Nevertheless, all the results of this site (reflectance factor, atmosphere conditions and TOA radiance) are presented, since it is a surface that can be used in future calibrations and it is important to know its characteristics.

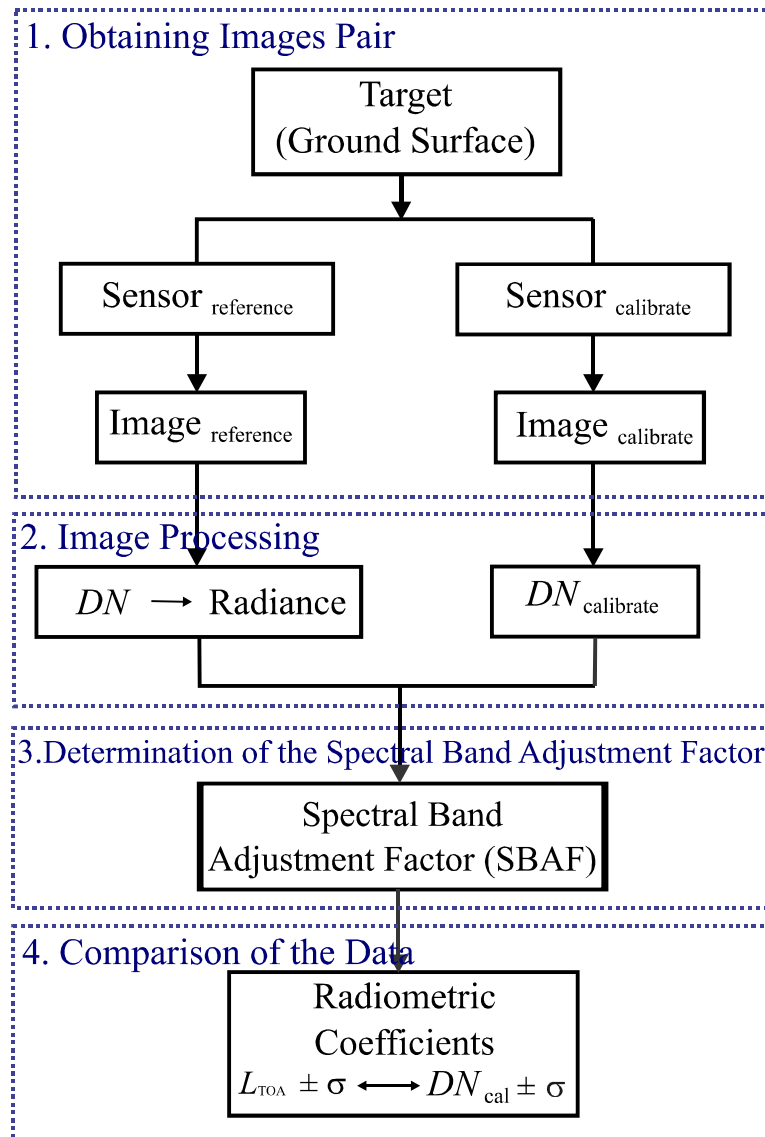
The last step of the reflectance-based approach was determining the calibration coefficient for each sensor spectral band by comparing the average DN output from the sensor to the predicted at sensor radiance calculated by MODTRAN. Note that the MODTRAN output is the Top-of-Atmosphere (TOA) radiance for each nanometer (hyperspectral TOA radiance). Therefore, before performing this comparison, it is necessary to weight the output data of MODTRAN with the Spectral Response Function (SRF) of the sensor to find the band averaged at-sensor radiance values at each spectral band, similar to **Equation 2.24**.

The uncertainty of the reflectance-based method has traditionally been estimated using the classical method (see **section 2.3.1**), therefore, this present work utilized this approach in almost all the stages of the performed measurement. However, the uncertainty propagate of **Equation 2.24** using the classical method is complex because it is difficult to determine the complete set of partial derivatives required by this method and also to estimate the existing covariances. Then, to solve this issue, Monte Carlo simulation approach was applied (see **section 2.3.2**).

3.3. Cross-Calibration Method

In the cross-calibration method, the response of the sensor under investigation is compared against a reference sensor that is well-characterized over time. In general, a calibration mission using the cross-calibration method includes four steps: (i) obtaining images pair; (ii) processing images pair; (iii) determination and application of the Spectral Bands Adjustment Factor (SBAF); and (iv) comparison of the sensors data, to obtain the radiometric calibration coefficients, along with its associated uncertainty. In **Figure 3.18** is illustrated the calibration procedure adopted. The following sections describe how each of these steps was performed. However, firstly the two test sites used to perform the cross-calibration are described.

Figure 3.18. General work flowchart for cross-calibration.

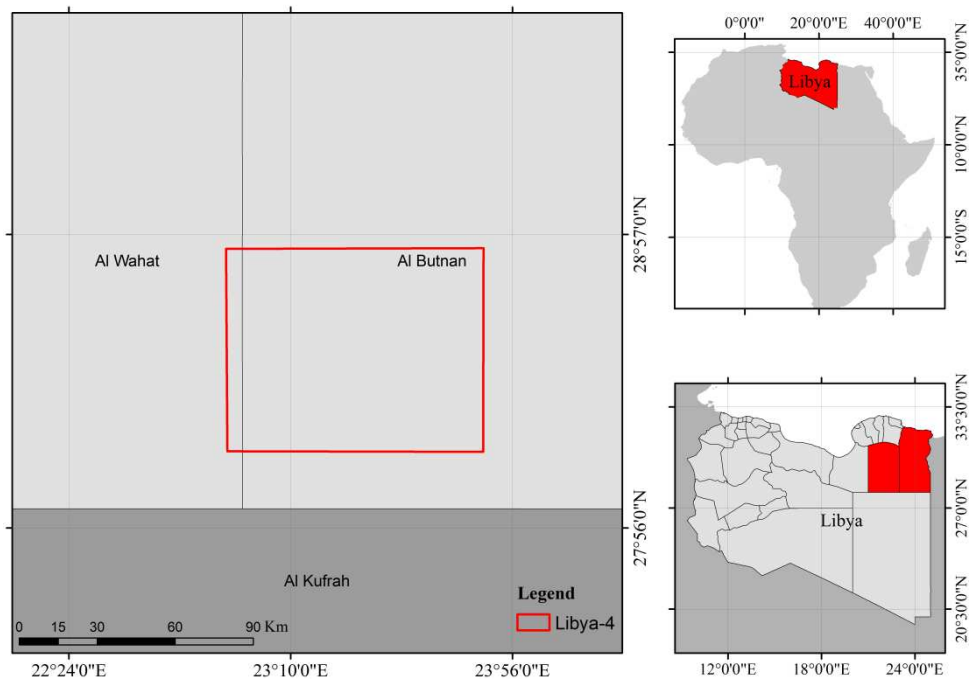


3.3.1. Test Sites Overview

The cross-calibration between MUX/WFI/CBERS-4 and OLI/Landsat-8 sensors was performed based on simultaneous imaging of two different sites: (a) Libya-4, Lybia; and (b) Atacama Desert, Chile. The Atacama Desert region has been described in **section 3.2.1**. The location of the Atacama Desert can be seen in **Figure 3.5**.

Pseudo invariant calibration sites (PICS) have been used for on-orbit radiometric trending of optical satellite systems for more than 15 years (HELDER et al., 2010; HELDER et al., 2013). According to Mishra et al. (2014b), the advantages of using these sites are their stable spectral characteristics over time, high reflectance, and minimal atmospheric effect on upward radiance. Several sites have been developed and include locations in Libya, Algeria, Niger and Mauritania. The site known as Libya-4 has proven to be the most stable of these sites (HELDER et al., 2013). **Figure 3.19** shows the location of Libya-4.

Figure 3.19. Location of the Libya-4 site.



3.3.2. Image Pair

Table 3.8 provides information about the metadata for the scenes utilized in this present study. The images of the OLI/Landsat-8 and MUX/WFI/CBERS-4 sensors from Libya-4 were acquired with four-days apart, but the site known as Libya-4 has proven to be the most stable of PICS sites over time (HELDER et al., 2013). **Figure 3.20** and **Figure 3.21** shows the image pairs from Libya-4 and Atacama Desert, respectively

Table 3.8. Metadata of scenes used for MUX/WFI/CBERS-4 and OLI/Landsat-8 cross-calibration.

Sensor/Satellite	Date	Acquisition Time	Path/Row	Solar zenith angle	Solar azimuth angle	Look Angle
Libya-4						
OLI/Landsat-8	07/11/2015	08:54	181/040	22.5°	102.0°	Nadir
MUX/CBERS-4	07/07/2015	09:20	095/068	17.2°	106.6°	Nadir
WFI/CBERS-4	07/07/2015	09:20	094/069	16.4°	106.3°	Nadir
Atacama Desert						
OLI/Landsat-8	11/28/2015	14:31	233/76	25.3°	91.26°	Nadir
MUX/CBERS-4	11/28/2015	14:52	177/126	19.8°	88.43°	Nadir
WFI/CBERS-4	11/28/2015	14:51	177/123	18.9°	97.8°	Nadir

Figure 3.20. Libya-4 image from (a) OLI/Landsat-8 (b) MUX/CBERS-4 and (c) WFI/CBERS-4. The red box indicates the location of the study area.

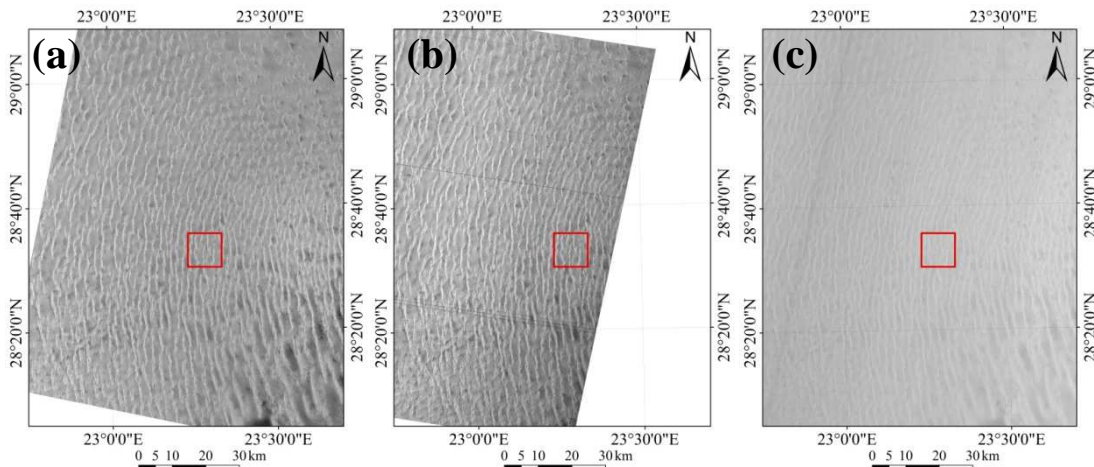
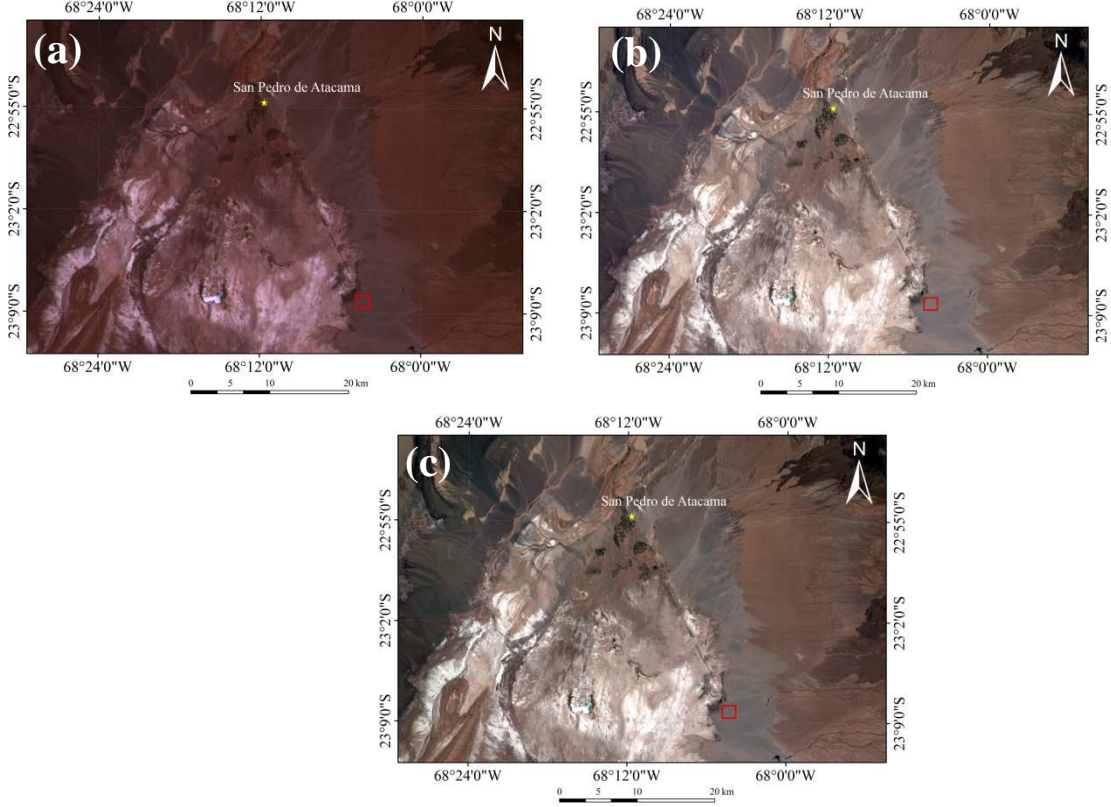


Figure 3.21. Atacama Desert image from (a) OLI/Landsat-8 (b) MUX/CBERS-4 and (c) WFI/CBERS-4. The red box indicates the location of the study area.



3.3.3. Image Processing

The second step of the cross-calibration was converting the digital numbers (NDs) of the sensor considered as reference into radiance values (or reflectance). Standard Landsat-8 L1T products are distributed by USGS EROS in 16 bits unsigned integer format and can be rescaled to TOA spectral reflectance and TOA spectral radiance using the radiometric rescaling coefficients provided by the metadata file (MTL file), as briefly described below. According to Mishra et al. (2014a) OLI/Landsat-8 data can be converted to TOA spectral radiance using the radiance rescaling factors provided in the metadata file:

$$L_{\lambda} = G_L \times DN_{cal} + offset_L \quad (3.12)$$

where: L_{λ} is the TOA spectral radiance [$W/(m^2 \cdot sr \cdot \mu m)$]; G_L is the band-specific multiplicative rescaling factor from the metadata; $offset_L$ is the band-specific additive rescaling factor from the metadata; DN_{cal} is the quantized and calibrated standard product pixel values (DN).

The OLI/Landsat-8 DNs data can also be converted to TOA planetary reflectance using reflectance rescaling coefficients provided by the metadata file, according to the equation:

$$\rho_{\lambda}' = G_{\rho} \times DN_{cal} + offset_{\rho} \quad (3.13)$$

where: ρ_{λ}' is the TOA planetary reflectance, without correction for solar angle; G_{ρ} is the band-specific multiplicative rescaling factor from the metadata; $offset_{\rho}$ is the band-specific additive rescaling factor from the metadata; and DN_{cal} is the quantized and calibrated standard product pixel values (DN).

Note that ρ_{λ}' does not contain a correction for the sun angle. TOA reflectance with a correction for the sun angle (solar zenith angle) is then:

$$\rho_{\lambda} = \frac{\rho_{\lambda}'}{\cos(\theta_{SZ})} = \frac{\rho_{\lambda}'}{\sin(\theta_{SE})} \quad (3.14)$$

where: ρ_{λ} is the TOA planetary reflectance; θ_{SE} is the local sun elevation angle. The scene center sun elevation angle in degrees is provided in the metadata; and $\theta_{SZ} = 90^{\circ} - \theta_{SE}$.

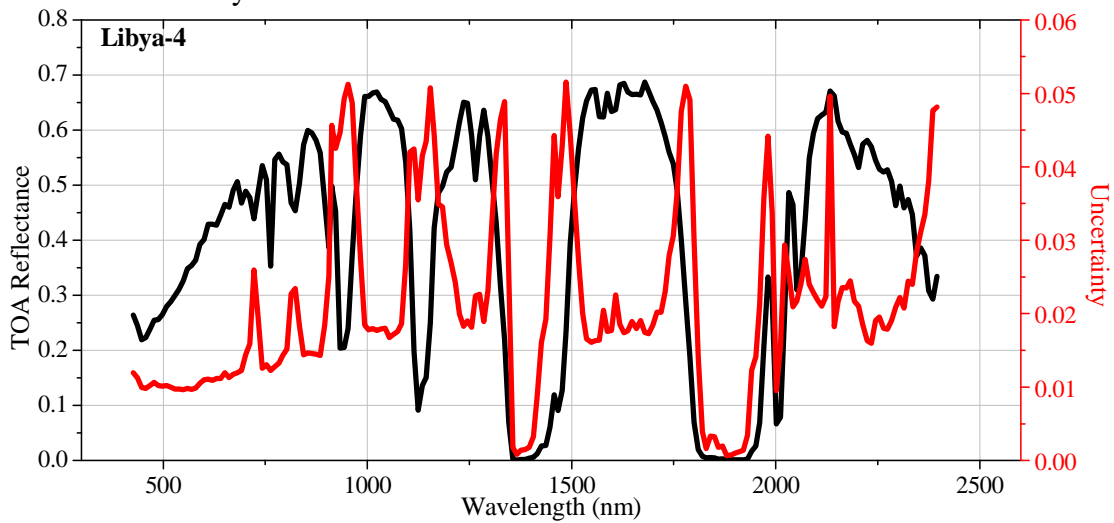
3.3.4. Spectral Band Adjustment Factor

There are significant differences in Spectral Response Function (SRF) profiles between corresponding MUX/WFI/CBERS-4 and OLI/Landsat-8 spectral bands (**Figure 2.3**). According to Teillet et al. (2001) the effects that these spectral band differences have on measured TOA reflectance depend on spectral variations in the exoatmospheric solar illumination, the atmospheric transmittance and the surface reflectance. The differences in the spectral responses of the sensors must be quantified and compensated to avoid large uncertainties in cross-calibration results (CHANDER et al., 2013b). For this purpose, the Spectral Band Adjustment Factor (SBAF) is calculated.

As mentioned previously, the cross-calibration was performed over two test sites: Libya-4 and Atacama Desert. In the case of the Libya-4 the Hyperion hyperspectral sensor on-board Earth Observing-1 (EO-1) was used as the spectral profile source, i.e.

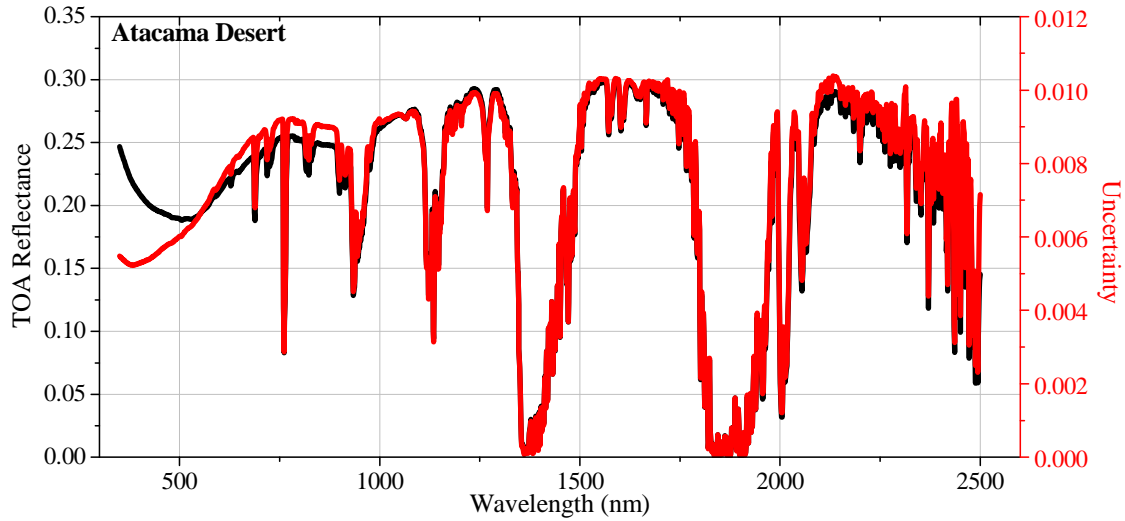
the Hyperion/EO-1 sensor was utilized to understand the spectral signature of the target and to derive the SBAF (HELDER et al. 2013; CHANDER et al. 2013b; MISHRA et al. 2014a). The calibration of Hyperion/EO-1 is well documented and it is radiometrically stable to within 5% (UNGAR et al. 2009). **Figure 3.22** shows the Hyperion/EO-1 TOA reflectance profile and its derived standard deviation using 224 cloud-free images over Libya-4 from 2004 to 2014.

Figure 3.22. Average TOA reflectance profile of 224 Hyperion/EO-1 images over Libya-4 from 2004 to 2014.



On the other hand, in the case of Atacama Desert the procedure to derive the spectral signature of the target was performed as described by Teillet et al. (2001). It has used measurements of surface spectral reflectance factor and atmospheric parameters available for the Atacama Desert. These data were used as inputs to a radiative transfer code (MODTRAN) to compute the TOA reflectance. **Figure 3.23** shows the TOA reflectance and its derived standard deviation using surface radiometric measurements over Atacama Desert.

Figure 3.23. Average TOA reflectance over Atacama Desert profile from ground measurements.



The reflectance/radiance at each spectral band for any sensor was calculated by integrating the spectral response of the sensor with the hyperspectral TOA reflectance/radiance profile at each sampled wavelength, averaged by the respective SRF (see **Equation 2.24**). The SBAF was calculated by taking the ratio of two respective simulated reflectances from both sensors of interest according to **Equation 2.26**.

The evaluation of the SBAFs inherent uncertainties was performed using Monte Carlo Simulation method (see **section 2.3.2**) (PINTO et al., 2016b). The program used to evaluate the uncertainties using Monte Carlo method can be divided into three stages: input, processing and output (similar to **Figure 2.5**). The input data were: (a) mathematical model of measurement; (b) probability density functions corresponding to each input quantity; and (c) number of iterations. The mathematical model of measurement used is represented by **Equation 2.26**. Input quantities are ρ_λ and SRF. Both input quantities were considered to have a normal probability density function (PDF) for each wavelength.

The input variables are hyperspectral data. The spectral signature of the target can be seen in both **Figure 3.22** and **Figure 3.23**. The variable Spectral Response Function is presented in **Figure 2.3**. Therefore, each one of the hyperspectral input variables (ρ_λ and SRF_λ) has a correlation matrix and the data were considered statistically dependent. The correlation coefficient is a measure of the relative mutual dependence of two

variables (x_i, x_j) , equal to the ratio of their covariances ($COV(x_i, x_j)$) to the positive square root of the product of their variances ($u(x_i)$ and $u(x_j)$), according **Equation 2.30**.

In order to assess the impact of the data correlations in the final uncertainty of SBAF it was utilized and evaluated the results of three correlation matrices. Every correlation matrix contains what is called main diagonal. It is the set of cells, which shows the correlation of each variable with itself, then, always contains entries equal to 1 (one). The first correlation matrix evaluated contains the maximum correlation: values equal to 1 (one) throughout the matrix. The second correlation matrix contains no correlation between the data: values equal to 0 (zero) throughout the matrix (except for the main diagonal that contains values of 1). Finally, in the third matrix the correlation values were decreasing in the "sub-diagonal", adjacent to the main diagonal, ranging from 0.9 to 0.1, with an interval of 0.1 and the remaining correlation values used to fill up the matrix was 0.05 (except, again, for the main diagonal that contains values of 1).

Lastly, the number of iterations influences the accuracy of the results obtained by Monte Carlo simulation. Some tests were conducted to evaluate variations in the results in relation to the number of iterations. With this study, we have chosen performing 10000 iterations in each variable randomly generated. Chen et al. (2015), for example, have performed 1000 iterations.

3.3.5. Image Analysis and Calibration Coefficients

The last step in the cross-calibration was determining the calibration coefficient for each sensor spectral band by comparing the digital number (DN) to the radiance predicted by the reference sensor (after the correction with the SBAF). This comparison was done using the **Equation 2.23**, which can be rewrite:

$$L_{\lambda,cal} = L_{\lambda,ref} \cdot \frac{[E_{SUN_{\lambda}} \cdot \cos \theta_z]_{cal}}{[E_{SUN_{\lambda}} \cdot \cos \theta_z]_{ref}} \cdot \frac{d_{ref}^2}{d_{cal}^2} \cdot (SBAF_{\lambda})^{-1} \quad (3.15)$$

With the **Equation 3.15** the radiance value of the sensor to be calibrated, $L_{\lambda,cal}$, is obtained from the reference sensor radiance, $L_{\lambda,ref}$. It is necessary to reverse

Equation 3.15 if you want to adjust the sensor to be calibrated with respect to the reference sensor.

Analyzing the **Equation 3.15**, it is possible to determine the source of uncertainty in the cross-calibration method. The first one is the associated uncertainty from the estimation of the radiance with the reference sensor ($L_{\lambda,ref}$). The determination of $L_{\lambda,ref}$ involves two sources of uncertainty: (a) the uncertainty associated with the accuracy of the reference sensor (instrumental uncertainty); and (b) the uncertainty of the selected surface. As mentioned earlier, the sensor utilized as reference (OLI/Landsat-8) presents a well-defined radiometric calibration, with 5% in terms of absolute at-aperture spectral radiance (IRONS et al., 2012; ROY et al., 2014). The associated uncertainty with the surfaces used in this work is computed using the standard deviation from the image ROI (region of interest) selected to perform the cross-calibration.

The second source of uncertainty is from the evaluation of the mean exoatmospheric solar irradiance. The mean exoatmospheric solar irradiance, $E_{SUN\lambda}$, for MUX/CBERS-4, WFI/CBERS-4 and OLI/Landsat-8 sensors was estimated using the CHKUR Extraterrestrial Solar Spectral Irradiance dataset from MODTRAN 5.2.1 software (PINTO et al., 2016a). The accuracy of the solar spectrum was considered within 1-2%, then, this uncertainty was propagated (using the Monte Carlo technique described in **section 2.3.2**) to the mean solar exoatmospheric irradiance of each sensor spectral band. The $E_{SUN\lambda}$ values for MUX/CBERS-4, WFI/CBERS-4 and OLI/Landsat-8 spectral bands are summarized in **Table 3.9**.

Table 3.9. Solar Exoatmospheric spectral irradiances ($E_{SUN\lambda}$) for MUX/CBERS-4, WFI/CBERS-4 and OLI/Landsat-8 spectral bands.

Spectral Bands (nm)	$E_{SUN\lambda}$ MUX [W/(m ² ·μm)]	$E_{SUN\lambda}$ WFI [W/(m ² ·μm)]	$E_{SUN\lambda}$ OLI [W/(m ² ·μm)]
Blue	1958 ± 35	1952 ± 35	1975 ± 34
Green	1852 ± 29	1852 ± 29	1852 ± 29
Red	1559 ± 18	1545 ± 18	1570 ± 18
NIR	1091 ± 11	1098 ± 11	951 ± 10

The third source of uncertainty is from the illumination angle (solar zenith angle). The next source of uncertainty is the determination of the Earth-Sun distance. Chander et al. (2009) presents Earth-Sun distance in astronomical units throughout a

year. If the images from the two sensors are collected at the same day, then, the Earth-Sun distance will be the same, and consequently, the ratio will be equal to one. The last source of uncertainty is from the SBAF, discussed in the previous section.

Finally, this radiance value of the sensor to be calibrated was compared to the DN generated by the sensor, and through application of **Equation 2.2** it was possible to determine the radiometric coefficients.

3.4. Validation of the MUX/WFI/CBERS-4 Radiometric Calibration Coefficients

To assess the radiometric calibration coefficients of both MUX/CBERS-4 and WFI/CBERS-4 sensors, a validation was performed using once again cross-calibration techniques. The ETM+/Landsat-7 sensor has been extremely stable since launching and it has been used by researchers for several cross-calibration studies. On May 31, 2003 the Scan Line Corrector (SLC) in the ETM+ instrument failed, causing the scanning pattern to exhibit wedge-shaped scan-to-scan gaps. Then, all ETM+/Landsat-7 scenes collected since May of 2003 have data gaps: the scenes have only 78% of their pixels. However, these data are still some of the most geometrically and radiometrically accurate of all civilian satellite data in the world.

The SLC failure has no impact on the radiometric performance with the valid pixels (CHANDER et al., 2009). Recently, for example, the ETM+/Landsat-7 sensor was used to calibrate the OLI/Landsat-8 sensor (CZAPLA-MYERS et al., 2015). For the validation of sensors MUX/WFI/CBERS-4 were discarded 22% of the ETM+ scene pixels, i.e. it were used just the valid pixels.

Absolute calibration uncertainties of the reflective bands of the ETM+/Landsat-7 are specified to be within 5% (MARKHAM and HELDER, 2012). Landsat-7 overpassed the Algodones Dunes region on 10th March 2015; therefore, the images collected on this date were used here. Hyperion/EO-1 images were used to derive the Spectral Band Adjustment Factor (SBAF) and to compensate the spectral differences between the sensors.

Five common Regions of Interest (ROIs) were chosen carefully to cover all four images (MUX/CBERS-4, WFI/CBERS-4, ETM+/Landsat-7 and Hyperion/EO-1) and to cover a range of targets (with different reflectance values). **Table 3.10** shows the metadata for the scenes used and **Figure 3.24** shows the Hyperion/EO-1, ETM+/Landsat-7, MUX/CBERS-4 and WFI/CBERS-4 images over Algodones Dunes.

Table3.10. Metadata of scenes used for MUX/CBERS-4 and WFI/CBERS-4 validation.

Satellite/ Sensor	Date	Acquisition Time	Path/Row	Solar zenith angle	Solar azimuth angle	Look Angle
ETM+/Landsat-7	03/10/2015	18:15:28	39/37	43.7°	143.5°	Nadir
MUX/CBERS-4	03/09/2015	18:33:29	238/63	42.1°	151.9°	Nadir
WFI/CBERS-4	03/09/2015	18:33:29	238/63	42.1°	151.9°	Nadir
Hyperion/EO-1	03/09/2015	17:10:40	39/37	53.6°	126.3°	18.1°

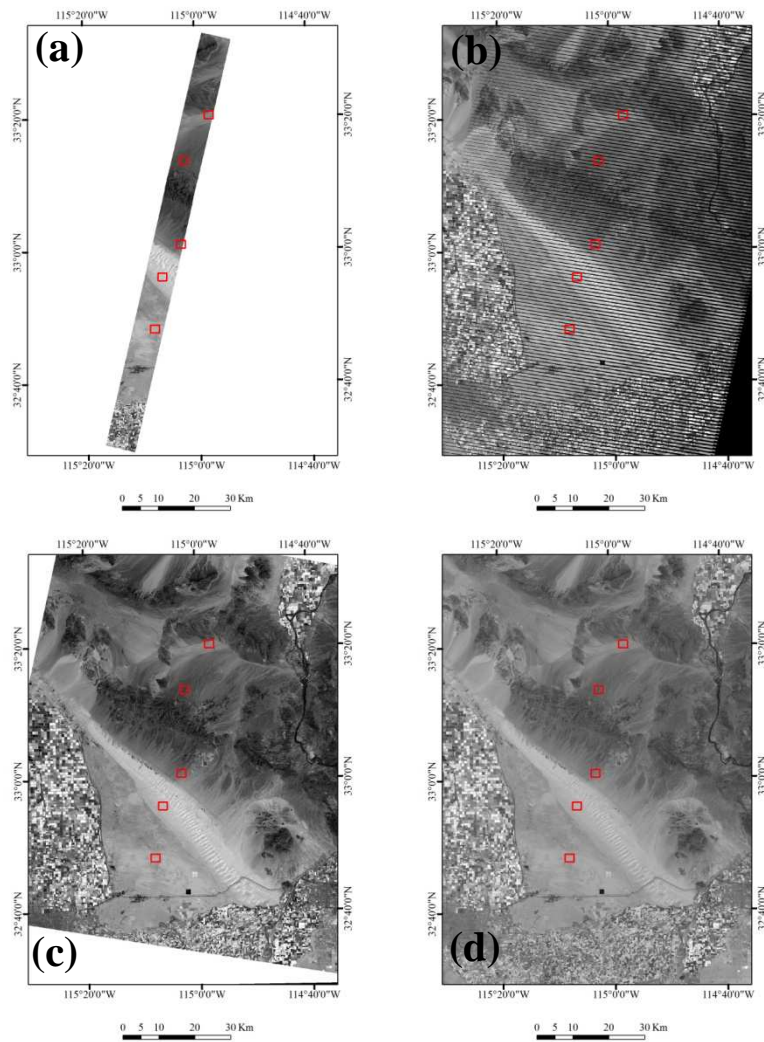
According to Mishra et al. (2014a) once spectral equivalency has been performed using the SBAF technique, for a stable atmosphere, the in-band reflectance can be directly compared to determine the differences between the sensors. Thus, the percentage differences were estimated between the well calibrated ETM+/Landsat-7 and the at-sensor reflectance reported by the current calibration of MUX/CBERS-4 and WFI/CBERS-4 (**Equation 3.16**). If the calibration coefficients estimated here are correct, both values must match within the associated uncertainties. It should be noted that an advantage in the use of reflectance is that the effects due to solar spectrum mismatch are eliminated.

$$Difference (\%) = \left(\frac{\rho_{CBERS,\lambda} - \rho_{Landsat,\lambda}}{\rho_{Landsat,\lambda}} \right) \times 100 \quad (3.16)$$

where: $\rho_{CBERS,\lambda}$ is the TOA reflectance for CBERS-4 sensors (MUX and WFI) after SBAF is applied; and $\rho_{Landsat,\lambda}$ is the TOA reflectance for ETM+/Landsat-7.

Note that the difference calculated by **Equation 3.16** should be compared with the uncertainties associated with the ETM+/Landsat-7 and MUX/WFI/CBERS-4 sensors. If the difference is less than the uncertainties, then, it means that sensors measure, statistically, the same value of reflectance. However, if the difference is greater than the associated uncertainty with the sensors, then, it means that there is a significant difference between the measurements with these sensors.

Figure 3.24. Algodones Dunes image from (a) Hyperion/EO-1; (b) EMT+/Landsat-7; (c) MUX/CBERS-4 and (d) WFI/CBERS-4. The five red boxes indicate the location of the five ROIs.



4 RESULTS AND DISCUSSION

In this section are presented the results obtained in the absolute radiometric calibration using the reflectance-based approach and the cross-calibration method, described in the **section 4.1** and **section 4.2**, respectively. The combined results achieved with these two methods of calibration are presented in **section 4.3**. Lastly, in **section 4.4** the validation of the radiometric calibration coefficients (CBERS-4 sensors) is presented.

4.1. Reflectance-Based Approach

4.1.1. Laboratory Measurements

In order to analyze and to evaluate the conditions of the instruments and their respective contributions to the final uncertainty of the measurements, experiments were performed at LaRaC. As explained in **section 3.2.2**, the measurements at LaRaC were held in three occasions: (1) before the fieldwork in Brazil; (2) after the fieldwork in Brazil, which also served as laboratorial step before the fieldwork in Chile; (3) after the fieldwork in Chile. The instruments used during these fieldworks (the Spectralon panel from Labsphere and the spectroradiometer ASD FieldSpec) were evaluated in relation to similar equipment.

Spectroradiometer Calibration

As described in **section 3.2.2**, ten set of radiance measurements using an integrating sphere source and five levels of radiance were performed. **Figure 4.1** shows the mean of the radiance measurements and its uncertainty estimated with four illumination levels (340 W, 240 W, 90 W and 45 W, see **Table 3.4**) from laboratory 1. The results from laboratory 2 and 3 are similar.

As can be seen in **Figure 4.1a** and **Figure 4.1b**, the spectral behavior was similar for both spectroradiometers. Remembering that one spectroradiometer was that used during the fieldwork and another one belonging to the laboratory, which was considered as a reference. Here these spectroradiometers will be called F18184 (fieldwork spectroradiometer) and F6246 (reference spectroradiometer). It was observed in both spectroradiometers data the presence of discontinuities in the radiance values around

1000 and 1850 nm, corresponding to "exchange" of the radiometers (PINTO, 2011). The relative uncertainties with the spectroradiometer F6426 were between 0.0013 to 0.84% in the spectral range of 350 to 2400 nm, while they ranged from 0.0018 to 0.76% for spectroradiometer F18184, considering the entire spectral range (350 to 2500nm).

In order to verify if there has been any change in the spectroradiometer before and after the fieldwork, it was calculated the different between both radiance measurements (Figure 4.2). The measurements taken before and after the fieldwork had minor changes. Excluding the very noisy regions (350-450 nm and 2400-2500nm) the absolute difference was between 0.00010 to 2.4%. On average the absolute difference was in the order of 0.5% throughout all electromagnetic spectrum (350-2500 nm). This results indicates that the behavior of the equipment remained unchanged (no breaking of fibers, no change in calibration, etc.) over the fieldwork measurements.

Figure 4.1. In (a) and (b) radiance as a function of wavelength of the FieldSpec F6426 and F18184, respectively; and (c) and (d) relative uncertainty as a function of wavelength of the FieldSpec F6426 and F18184, respectively.

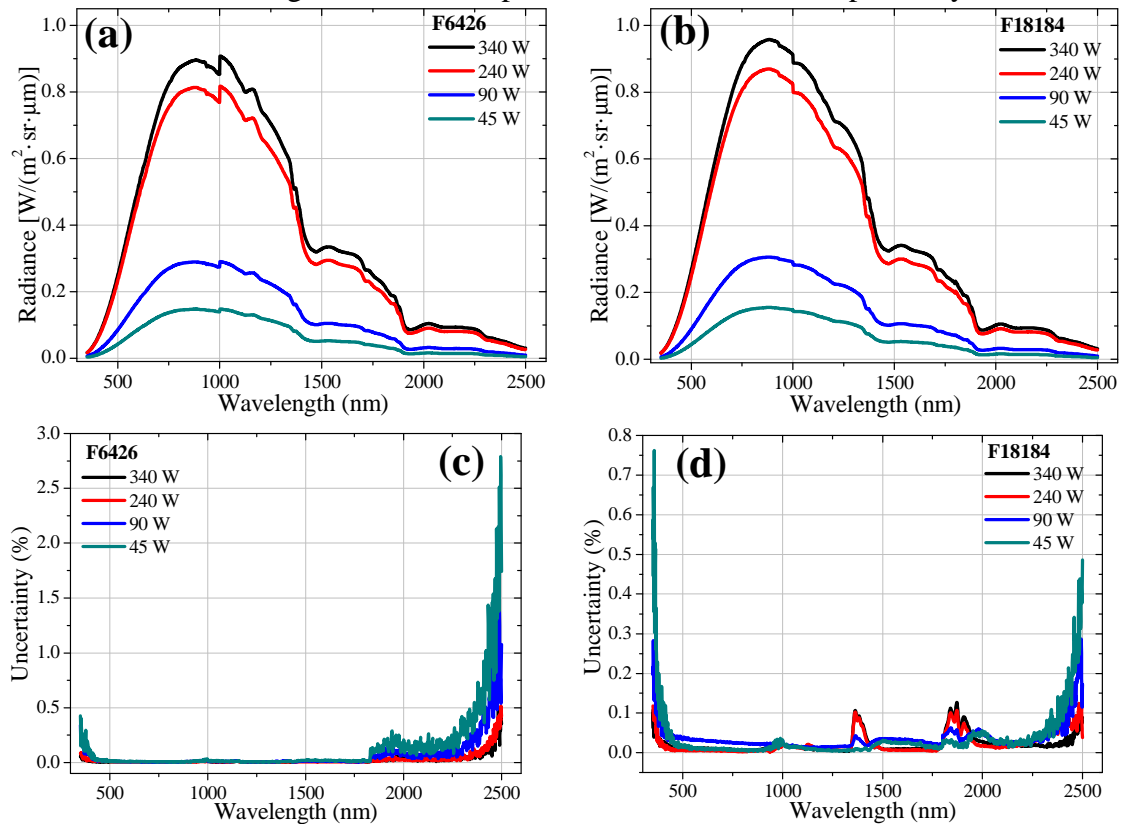
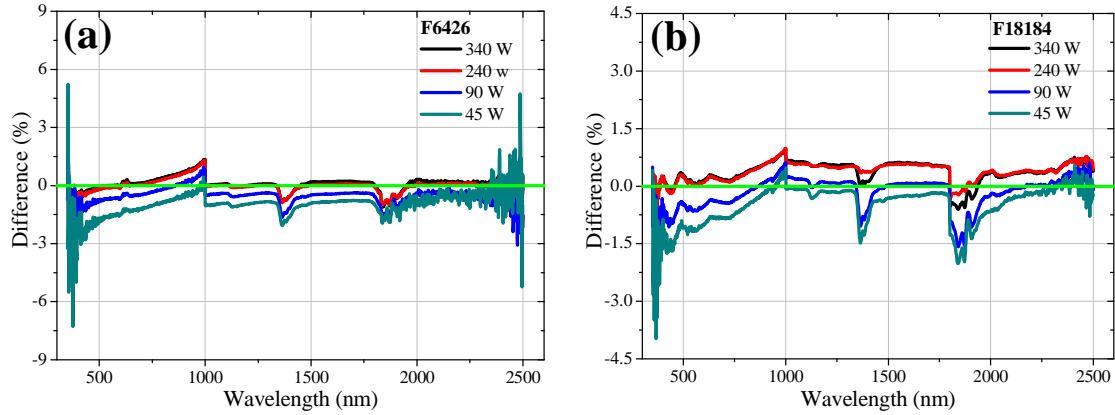


Figure 4.2. Difference between the measurements with the integrating sphere source made before and after fieldwork as a function of the wavelength. In (a) with the FieldSpec F6426; and (b) with the FieldSpec F18184. The differences presented in this figure are from laboratory 1 compared with laboratory 2. The results during laboratory 3 were similar.



Reference Panel Calibration

Laboratory measurements also allowed the field reference panel to be referenced to a standard panel from LaRaC. As described in **section 3.2.2**, ten successive measurements of the panel reflectance factor were obtained to determine the panel correction factor. In **Figure 4.3** is presented the average reflectance factor of the panel used in the ground measurement and its uncertainties. The reflectance factor values shown in **Figure 4.3** were corrected for the reflectance factor of the standard panel (provided by the manufacturer, see **Figure 3.9**). The relative uncertainties for the reflectance of the fieldwork panel were smaller than: 0.21% in the spectral range of 350 to 450 nm; 0.030% in the spectral range of 450 to 2200 nm; and 0.11% from 2200 to 2500 nm.

To verify if there has been any change in the reference panels before and after the ground measurements, it was calculated the difference between the measurements of the panel reflectance made before and after fieldwork, see **Figure 4.4**. The results showed small differences between the reflectance of the panel obtained before and after the ground measurements. In the spectral region between 350-450 nm there was major absolute difference between the measurements: 0.017-1.27%. This can be explained by the use of the panel reference in the field, where it was exposed to dust and solar radiation, causing degradation of their characteristics. The absolute average difference was 0.13% throughout the entire explored electromagnetic spectrum range.

Figure 4.3. In (a) reflectance factor of the panel reflectance used in fieldwork as a function of wavelength; and (b) uncertainties (mean standard deviation) as a function of wavelength.

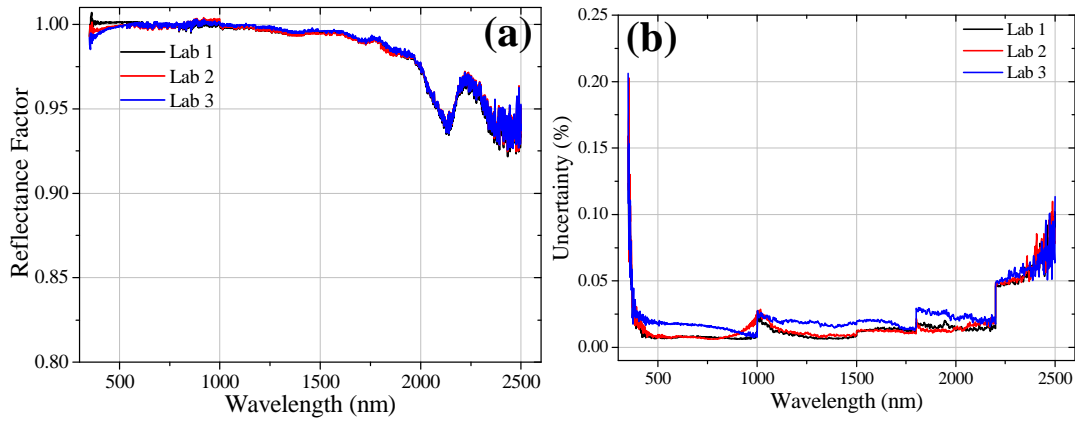
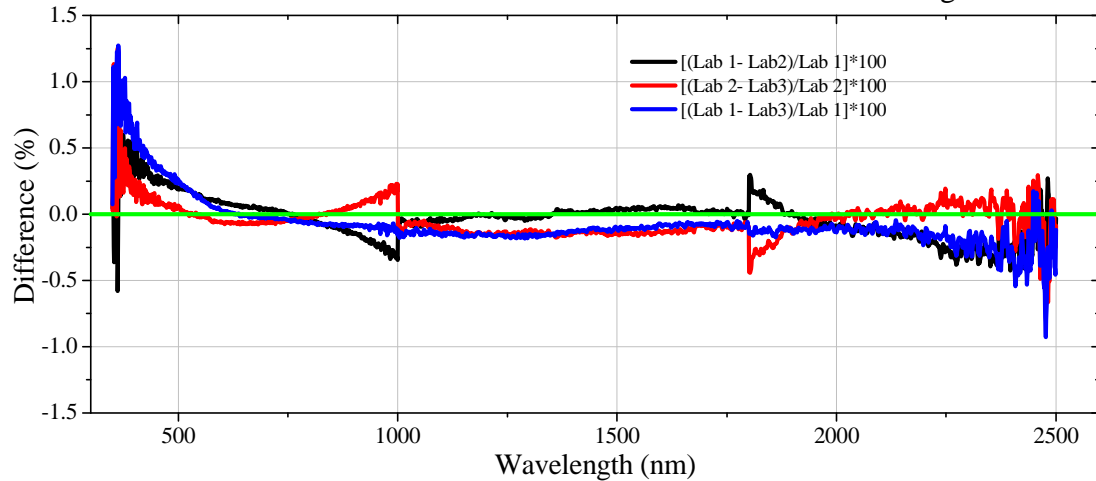


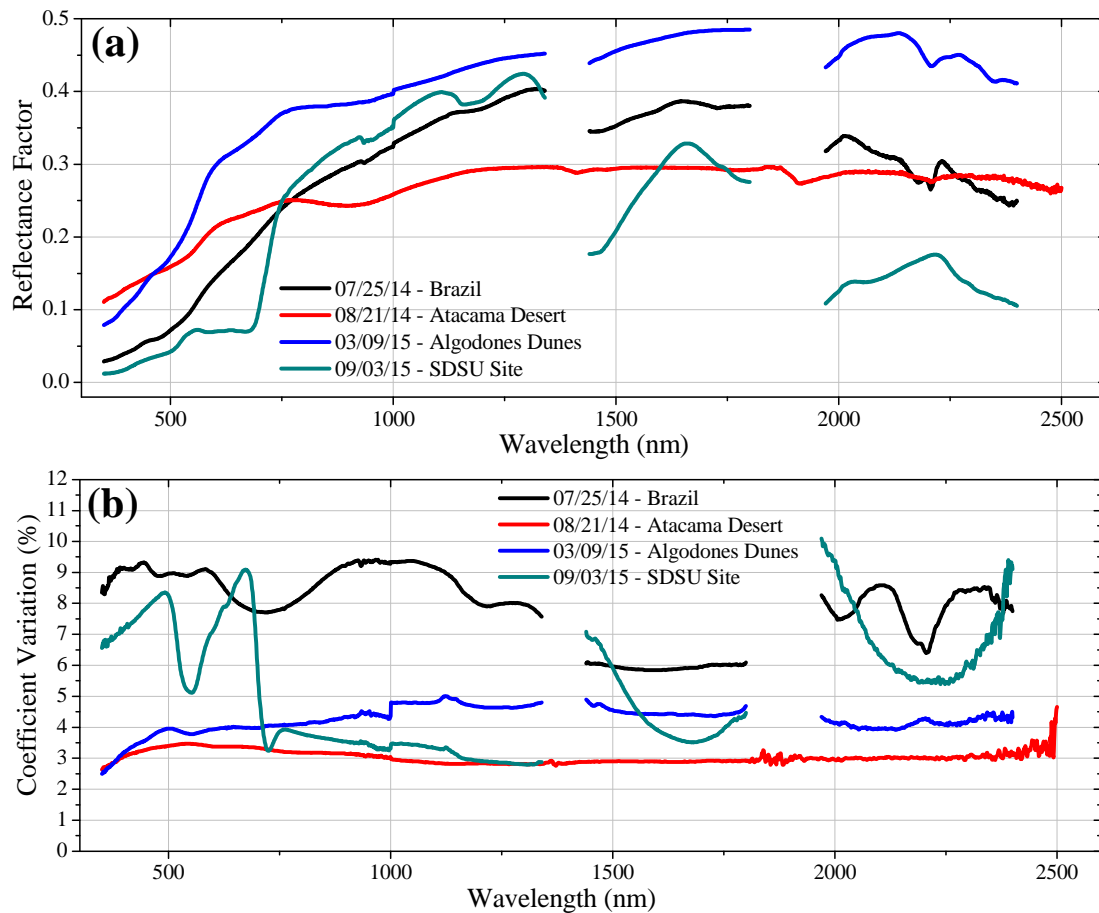
Figure 4.4. Difference between the measurements of the reference panel reflectance made before and after fieldwork as a function of the wavelength.



4.1.2. Field Measurements

The first component of the reflectance-based approach is the surface reflectance factor at the time of sensor overpass. In **Figure 4.5a** is presented the spectral reflectance factor from the four reference sites: (i) west part of the Bahia State, Brazil; (ii) Atacama Desert, Chile; (iii) Algodones Dunes, USA; and (iv) South Dakota State University (SDSU) site, USA. In addition, the coefficient of variation (CV) defined as the ratio between the standard deviation and the average is shown as a percentage in **Figure 4.5b**.

Figure 4.5. In (a) Spectral reflectance results of the reference sites; and (b) surface coefficient of variation in percentage.



The gaps around 1400 and 1800 nm are due to strong water vapor absorption near those wavelengths and the 2400-2500 nm spectral region shows larger variability primarily due to decreasing signal level. The line representing the Atacama Desert is the only one that did not present gaps in both the reflectance factor and the coefficient of variation curve in the spectrum regions strongly affected by water vapor absorption. This means that the amount of water is very low in this region (Atacama Desert).

According to Scott et. al (1996) reflectance values higher than 0.3 over the entire spectral range are preferred. This reduces the impact of uncertainties in the path radiance. The reference surface in Brazil has a typical spectral reflectance curve for soil. Both minimum and maximum reflectance were, respectively, 0.03 and 0.4. As it can be seen in **Figure 4.5a** the average reflectance factor of the Atacama Desert was between 0.11 and 0.25 from 350 to 1000 nm and around 0.30 from 1000 to 2500 nm. The reference surface at Algodones Dunes presents reflectance higher than 0.3 in almost the

entire spectral range. The average Algodones Dunes reflectance factor was between 0.08 and 0.30 from 350-600 nm and between 0.30 and 0.49 from 600-2500 nm. Lastly, the SDSU site has a typical spectral reflectance curves for vegetation. Vegetation cover is a very good absorber of electromagnetic energy in the visible region, then, the reflectance factor in this spectral range was between of 0.012 to 0.11. Absorption greatly reduces and reflection increases in the red/infrared boundary near 700 nm. The reflectance was between 0.11 to 0.42 from 700 to 1400 nm and decreases for the longer wavelengths.

Ponzoni et. al (2015) suggested that a surface is sufficiently spatially uniform if the Coefficient of Variation (CV) is lower than 5%. The average CV of the reference surface in Brazil was between 5.84 to 9.41%. The average relative CV of the spectral measurements at Algodones Dunes ranged from 2.5 to 5.0%, indicating that the reference surface presents a spatial uniformity better than 5%. The average CV of the spectral measurements at Atacama Desert ranged from 2.63 to 4.65%. Finally, the average CV of the SDSU site was between 2.79 to 10.1%.

As described in **section 3.2.3**, solar radiometer measurements were used to characterize the atmosphere over the reference surfaces, providing data used in a Langley method retrieval scheme to determine the atmospheric optical depths that are inverted to give aerosol size distribution and column water vapor. **Figure 4.6, 4.7, 4.8 and 4.9** shows the Langley Method graphs obtained with the data collected during measurements in Brazil, Chile, Algodones Dunes and SDSU site, respectively.

Figure 4.6. Langley graph on July 25th, 2014 in Brazil site, for spectral bands of the CE317/CIMEL sun photometer.

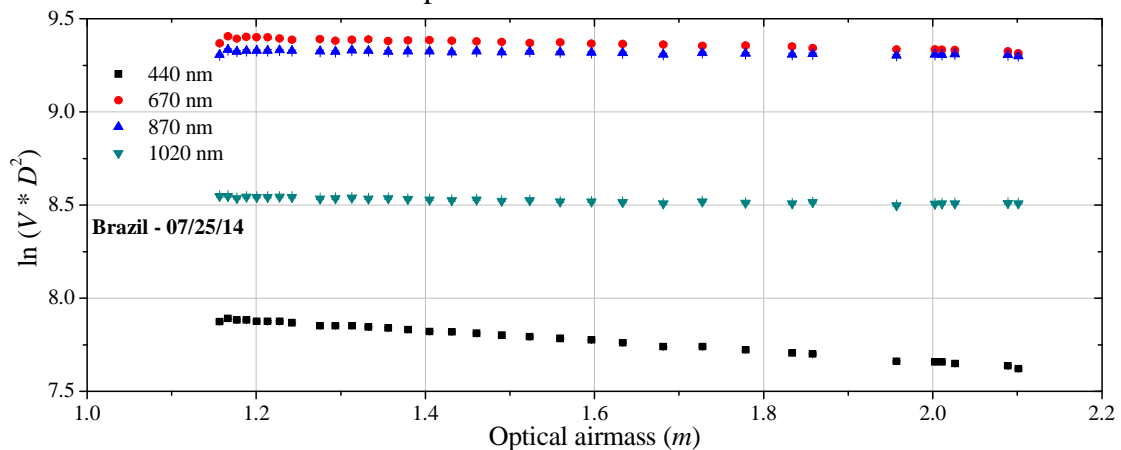


Figure 4.7. Langley graph on August 21st 2014 in Atacama Desert, Chile, for spectral bands of the CE317/CIMEL sun photometer.

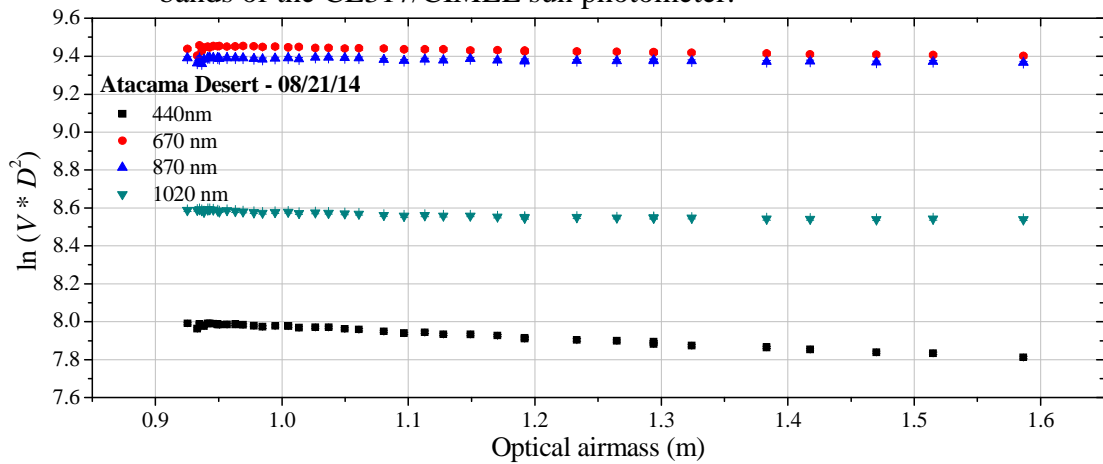


Figure 4.8. Langley graph on March 9th 2015 in Algodones Dunes, USA, for spectral bands of the Automated Solar Radiometer (ASR).

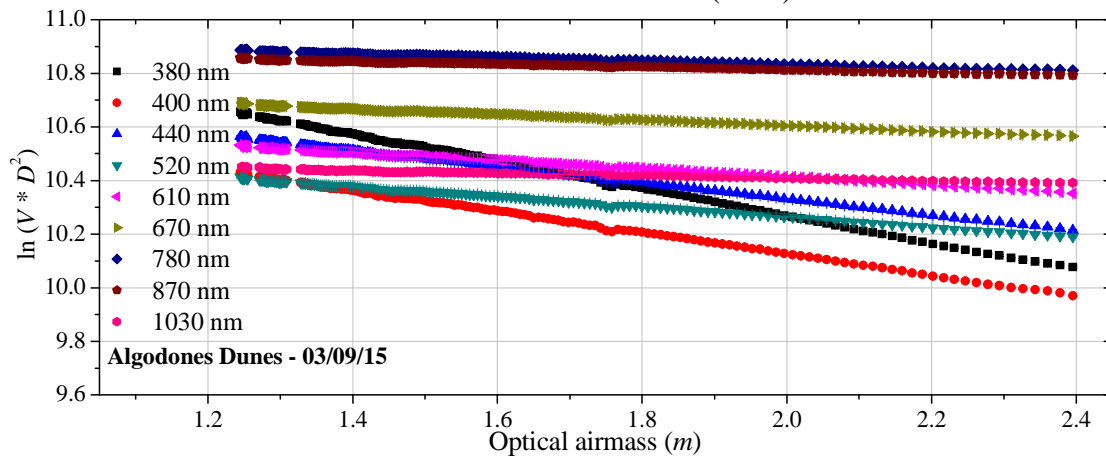
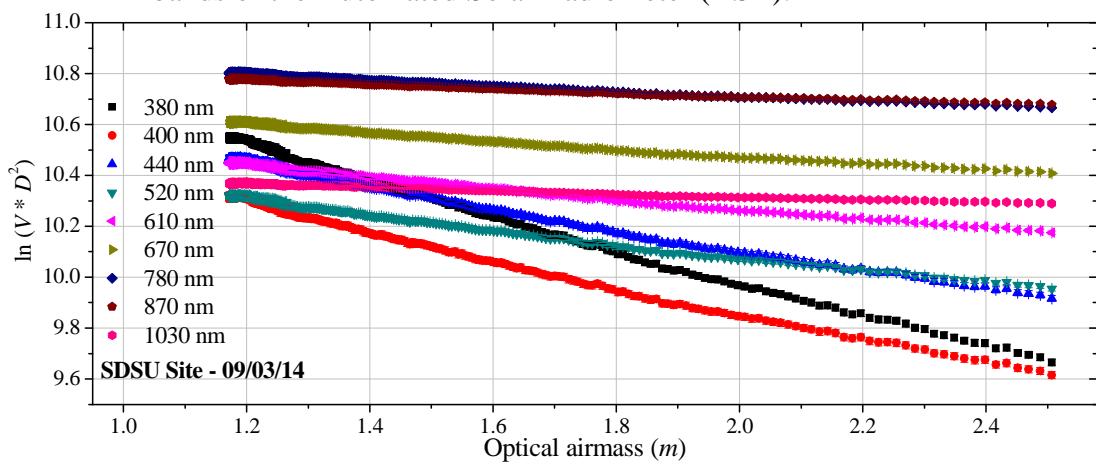


Figure 4.9. Langley graph on September 3th 2015 in SDSU site, USA, for spectral bands of the Automated Solar Radiometer (ASR).



The dependence of $\ln(V_\lambda \times D^2)$ with the optical air mass, m , have a behavior similar to a straight, as suggested in Langley method. Thus, it was performed a linear regression, which the slope is equal the total optical depth, τ_λ , and the intercept is equal of the natural logarithm of CE317/CIMEL and ASR calibration constant, $V_{0,\lambda}$. The results of this fitting for the data collected in Brazil, Chile, Algodones Dunes and SDSU site, are presented in **Tables 4.1, 4.2, 4.3** and **4.4**, respectively.

The sun photometer measurements or the solar radiometer carried out during the first day of each campaign were utilized to calibrate the instrument (CIMEL/CE-317 or the Automated Solar Radiometer), i.e., the data from the first day of the each campaign were used to determine the calibration constant $V_{0,\lambda}$ according to **Equation 2.12**. This explains why the values of the calibration constant are the same in all fieldwork on each surface reference.

Table 4.1. Total optical depth, τ_λ , and calibration constant, $V_{0,\lambda}$ of the CE317/CIMEL in measurements performed in Brazil site.

Banda (nm)	$V_{0,\lambda}$	$\sigma_{Relative}$ (%)	τ_λ	$\sigma_{Relative}$ (%)	R^2	χ^2_{red}
07/23/2014						
1020	5361 ± 14	0.26	0.0318 ± 0.0008	2.52	0.90	0.98
870	11571 ± 22	0.19	0.0329 ± 0.0006	1.82	0.95	1.04
670	12930 ± 28	0.22	0.0710 ± 0.0007	0.99	0.98	0.95
440	3499 ± 15	0.43	0.2599 ± 0.0014	0.54	1.00	0.98
07/24/2014						
1020	5361 ± 14	0.26	0.0415 ± 0.0009	2.17	0.79	1.19
870	11571 ± 22	0.19	0.0228 ± 0.0009	3.95	0.60	1.64
670	12930 ± 28	0.22	0.0598 ± 0.0011	1.84	0.85	1.74
440	3499 ± 15	0.43	0.2425 ± 0.0020	0.82	0.96	3.60
07/25/2014						
1020	5361 ± 14	0.26	0.0398 ± 0.0006	1.51	0.88	1.06
870	11571 ± 22	0.19	0.0245 ± 0.0006	2.45	0.71	0.97
670	12930 ± 28	0.22	0.0645 ± 0.0009	1.40	0.89	1.25
440	3499 ± 15	0.43	0.2446 ± 0.0012	0.49	0.98	4.55
07/26/2014						
1020	5361 ± 14	0.26	0.0540 ± 0.0022	4.07	0.66	1.55
870	11571 ± 22	0.19	0.0424 ± 0.0028	6.60	0.56	2.74
670	12930 ± 28	0.22	0.097 ± 0.005	5.15	0.62	2.89
440	3499 ± 15	0.43	0.340 ± 0.013	3.82	0.71	2.38

Table 4.2. Total optical depth, τ_λ , and calibration constant, $V_{0,\lambda}$ of the CE317/CIMEL in measurements performed at Atacama Desert site in Chile.

Banda (nm)	$V_{0,\lambda}$	$\sigma_{Relative}$ (%)	τ_λ	$\sigma_{Relative}$ (%)	R^2	χ^2_{red}
08/19/2014						
1020	5730 ± 40	0.70	0.0849 ± 0.0023	2.71	0.86	1.00
870	12470 ± 140	1.12	0.085 ± 0.004	4.71	0.71	1.00
670	13950 ± 140	1.00	0.132 ± 0.003	2.27	0.88	1.00
440	3770 ± 40	1.06	0.3162 ± 0.0029	0.92	0.98	1.00
08/20/2014						
1020	5730 ± 40	0.70	0.1050 ± 0.0012	1.14	0.78	1.02
870	12470 ± 140	1.12	0.0675 ± 0.0009	1.33	0.64	1.14
670	13950 ± 140	1.00	0.1237 ± 0.0010	0.81	0.85	1.27
440	3770 ± 40	1.06	0.3018 ± 0.0012	0.40	0.98	0.99
08/21/2010						
1020	5730 ± 40	0.70	0.0781 ± 0.0009	1.15	0.85	1.08
870	12470 ± 140	1.12	0.0442 ± 0.0011	2.49	0.31	1.10
670	13950 ± 140	1.00	0.0972 ± 0.0014	1.44	0.61	1.23
440	3770 ± 40	1.06	0.2665 ± 0.0009	0.34	0.98	1.06
08/22/2010						
1020	5730 ± 40	0.70	0.0877 ± 0.0011	1.25	0.49	1.34
870	12470 ± 140	1.12	0.0501 ± 0.0006	1.20	0.44	1.22
670	13950 ± 140	1.00	0.1034 ± 0.0007	0.68	0.84	1.69
440	3770 ± 40	1.06	0.2808 ± 0.0005	0.18	0.99	0.79

Table 4.3. Total optical depth, τ_λ , and calibration constant, $V_{0,\lambda}$ of the Automated Solar Radiometer (ASR) in measurements performed at Algodones Dunes site in USA.

Banda (nm)	$V_{0,\lambda}$	$\sigma_{Relative}$ (%)	τ_λ	$\sigma_{Relative}$ (%)	R^2	χ^2_{red}
03/09/2015						
380	79470 ± 100	0.13	0.5071 ± 0.0008	0.16	1.00	1.00
400	55080 ± 60	0.11	0.3951 ± 0.0007	0.18	1.00	1.00
440	55900 ± 60	0.11	0.2999 ± 0.0006	0.20	1.00	1.00
520	41890 ± 40	0.10	0.1896 ± 0.0005	0.26	1.00	1.00
610	44950 ± 30	0.07	0.1496 ± 0.0005	0.33	1.00	1.00
670	49720 ± 40	0.08	0.1048 ± 0.0005	0.48	1.00	1.00
780	57710 ± 40	0.07	0.0645 ± 0.0004	0.62	0.99	1.00
870	55270 ± 40	0.07	0.0535 ± 0.0004	0.75	0.99	1.00
1030	36576 ± 25	0.07	0.0502 ± 0.0004	0.80	0.99	1.00
03/10/2015						
380	79470 ± 100	0.13	0.48810 ± 0.00021	0.04	1.00	1.01
400	55080 ± 60	0.11	0.36865 ± 0.00030	0.08	1.00	1.00
440	55900 ± 60	0.11	0.27434 ± 0.00023	0.08	1.00	1.01
520	41890 ± 40	0.10	0.16844 ± 0.00025	0.15	1.00	1.00
610	44950 ± 30	0.07	0.12981 ± 0.00025	0.19	1.00	1.00
670	49720 ± 40	0.08	0.08550 ± 0.00027	0.32	1.00	1.00
780	57710 ± 40	0.07	0.04991 ± 0.00021	0.42	0.99	1.00
870	55270 ± 40	0.07	0.03899 ± 0.00024	0.62	0.99	1.00
1030	36576 ± 25	0.07	0.03253 ± 0.00022	0.68	0.99	1.00

Table 4.4. Total optical depth, τ_λ , and calibration constant, $V_{0,\lambda}$ of the Automated Solar Radiometer (ASR) in measurements performed at SDSU site in USA.

Banda (nm)	$V_{0,\lambda}$	$\sigma_{Relative}$ (%)	τ_λ	$\sigma_{Relative}$ (%)	R^2	χ^2_{red}
09/03/2015						
380	85120 ± 250	0.29	0.6879 ± 0.0020	0.29	1.00	1.00
400	57650 ± 180	0.31	0.5536 ± 0.0022	0.40	0.99	0.97
440	58240 ± 150	0.26	0.4342 ± 0.0018	0.41	0.99	0.92
520	42550 ± 90	0.21	0.2907 ± 0.0014	0.48	0.99	0.98
610	44560 ± 70	0.16	0.2190 ± 0.0010	0.46	0.99	1.13
670	49010 ± 60	0.12	0.1629 ± 0.0009	0.55	0.99	0.89
780	55890 ± 50	0.09	0.1101 ± 0.0006	0.54	0.99	0.96
870	52820 ± 40	0.08	0.0822 ± 0.0005	0.61	0.99	1.03
1030	34400 ± 20	0.06	0.0651 ± 0.0004	0.61	0.99	1.55

The total optical depth accuracy depends on: (i) the calibration of the sun photometer; and (ii) of the atmospheric conditions stability during the period of measurements. According to Biggar et al. (1994) the sun photometer measurements uncertainties should not be more than 5%. Just only one day during the fieldwork in Brazil (on 07/26/14) and for the wavelengths 670 nm and 870 nm the uncertainties were larger than 5%: 5.2 and 6.6%, respectively. Then, except on 07/26/14, the uncertainties in the measurements of the total optical depth, τ_λ , with the CIMEL/CE-317 ranged between 0.18-4.71%. In general, the uncertainty in the band centered at 870 nm showed higher uncertainty. On the other hand, the measurements uncertainties of the total optical depth with the Automated Solar Radiometer were lower: varied between 0.04% (band 380 nm at March 10th, 2015) and 0.80% (band 1030 nm at March 9th, 2015).

The optical depth due to Rayleigh scattering, $\tau_{Rayleigh}$, and the aerosol optical depth, $\tau_{Aerosol}$, were calculated using both **Equation 2.14** and **Equation 2.13**, respectively. **Table 4.5, 4.6, 4.7** and **4.8** present these two quantities for the fieldwork in Brazil, Chile, Algodones Dunes and SDSU site, respectively.

The aerosol optical depth (AOD) is a measure of radiation extinction due to the interaction of radiation with aerosol particles in the atmosphere. According to Rollin (2000) the variation in AOD with wavelength defines the attenuation of solar irradiance as a function of wavelength and it provides the basis for retrieving the columnar size distribution of the atmospheric aerosol. AOD lower than 0.1 indicates clear sky, whereas value of 1 corresponds to very hazy conditions (GRO et al., 2013).

In Brazil the AOD ranged from 0.0088 ± 0.0009 (870 nm) to 0.116 ± 0.013 (440 nm). The AOD in Chile, Atacama Desert, were between 0.0328 ± 0.0011 (870 nm) to 0.133 ± 0.003 (440 nm). The campaign in Algodones Dunes presented AOD lower than 0.08664 ± 0.0005 . The highest AOD value found was during the measurements in SDSU site; on September 3rd 2015 for 380 nm: 0.2695 ± 0.0027 . Therefore, in general, the four sites used presented low aerosol loading. Regarding the AOD relative's uncertainties, they ranged from 1.85-11.6% in Brazil, 0.92-5.41% in Chile, 0.58- 11% in Algodones Dunes and 0.63-1.21% in SDSU site.

Table 4.5. Rayleigh scattering, $\tau_{Rayleigh}$, and aerosol optical depth, $\tau_{Aerossol}$, of the CE317/CIMEL in measurements performed in Brazil site.

Banda (nm)	$\tau_{Rayleigh}$	$\sigma_{Relative}$ (%)	$\tau_{Aerossol}$	$\sigma_{Relative}$ (%)
07/23/2014				
1020	0.00737 ± 0.00003	0.41	0.0244 ± 0.0008	3.28
870	0.01398 ± 0.00006	0.43	0.019 ± 0.0006	3.16
670	0.04015 ± 0.00019	0.47	0.0308 ± 0.0007	2.27
440	0.2235 ± 0.0011	0.49	0.03646 ± 0.0017	4.66
07/24/2014				
1020	0.00737 ± 0.00003	0.41	0.0342 ± 0.0009	2.63
870	0.01398 ± 0.00006	0.43	0.0088 ± 0.0009	10.2
670	0.04016 ± 0.00017	0.42	0.0196 ± 0.0011	5.61
440	0.2235 ± 0.0009	0.40	0.019 ± 0.0022	11.6
07/25/2014				
1020	0.00736 ± 0.00003	0.41	0.0324 ± 0.0006	1.85
870	0.01397 ± 0.00006	0.43	0.0105 ± 0.0006	5.71
670	0.04014 ± 0.00016	0.40	0.0243 ± 0.0009	3.70
440	0.2234 ± 0.0009	0.40	0.0212 ± 0.0015	7.08
07/26/2014				
1020	0.00736 ± 0.00003	0.41	0.0466 ± 0.0022	4.72
870	0.01397 ± 0.00006	0.43	0.0284 ± 0.0028	9.86
670	0.04014 ± 0.00016	0.40	0.057 ± 0.005	8.77
440	0.2234 ± 0.0009	0.40	0.116 ± 0.013	11.2

Table 4.6. Rayleigh scattering, $\tau_{Rayleigh}$, and aerosol optical depth, $\tau_{Aerosol}$, of the CE317/CIMEL in measurements performed at Atacama Desert site in Chile.

Banda (nm)	$\tau_{Rayleigh}$	$\sigma_{Relative}$ (%)	$\tau_{Aerosol}$	$\sigma_{Relative}$ (%)
08/19/2014				
1020	0.00603 ± 0.00003	0.50	0.0789 ± 0.0023	2.92
870	0.01145 ± 0.00005	0.44	0.074 ± 0.004	5.41
670	0.03288 ± 0.00015	0.46	0.099 ± 0.003	3.03
440	0.1830 ± 0.0008	0.44	0.133 ± 0.003	2.26
08/20/2014				
1020	0.00604 ± 0.00003	0.50	0.0989 ± 0.0012	1.21
870	0.01145 ± 0.00005	0.44	0.0561 ± 0.0009	1.60
670	0.03290 ± 0.00014	0.43	0.0908 ± 0.0010	1.10
440	0.1831 ± 0.0008	0.44	0.1187 ± 0.0014	1.18
08/21/2010				
1020	0.00603 ± 0.00003	0.50	0.0721 ± 0.0009	1.25
870	0.01145 ± 0.00005	0.44	0.0328 ± 0.0011	3.35
670	0.03289 ± 0.00014	0.43	0.0643 ± 0.0014	2.18
440	0.1830 ± 0.0008	0.44	0.0835 ± 0.0012	1.44
08/22/2010				
1020	0.00603 ± 0.00003	0.50	0.0817 ± 0.0011	1.35
870	0.01145 ± 0.00005	0.44	0.0386 ± 0.0006	1.55
670	0.03288 ± 0.00014	0.43	0.0705 ± 0.0007	0.99
440	0.1830 ± 0.0008	0.44	0.0978 ± 0.0009	0.92

Table 4.7. Rayleigh scattering, $\tau_{Rayleigh}$, and aerosol optical depth, $\tau_{Aerossol}$, of the Automated Solar Radiometer (ASR) in measurements performed at Algodones Dunes site in USA.

Banda (nm)	$\tau_{Rayleigh}$	$\sigma_{Relativa}(\%)$	$\tau_{Aerossol}$	$\sigma_{Relativa}$ (%)
03/09/2015				
380	0.4395 ± 0.0018	0.41	0.0674 ± 0.0020	2.97
400	0.3551 ± 0.0015	0.42	0.0399 ± 0.0016	4.01
440	0.2394 ± 0.0010	0.42	0.0604 ± 0.0012	1.99
520	0.1206 ± 0.0005	0.41	0.0689 ± 0.0007	1.02
610	0.06294 ± 0.00026	0.41	0.08664 ± 0.0005	0.58
670	0.04302 ± 0.00017	0.40	0.06178 ± 0.0005	0.81
780	0.02326 ± 0.00009	0.39	0.0412 ± 0.0004	0.97
870	0.01497 ± 0.00006	0.40	0.0385 ± 0.0004	1.04
1030	0.00759 ± 0.00003	0.40	0.0426 ± 0.0004	0.94
03/10/2015				
380	0.4397 ± 0.0018	0.41	0.0486 ± 0.0018	3.70
400	0.3552 ± 0.0015	0.42	0.0136 ± 0.0015	11.0
440	0.2395 ± 0.0010	0.42	0.0349 ± 0.0010	2.87
520	0.1207 ± 0.0005	0.41	0.0478 ± 0.0006	1.26
610	0.06297 ± 0.00026	0.41	0.0669 ± 0.0004	0.60
670	0.04304 ± 0.00017	0.39	0.0425 ± 0.0003	0.71
780	0.02327 ± 0.00009	0.39	0.02665 ± 0.00023	0.86
870	0.01498 ± 0.00006	0.40	0.02393 ± 0.00025	1.04
1030	0.00759 ± 0.00003	0.40	0.02494 ± 0.00022	0.88

Table 4.8. Rayleigh scattering, $\tau_{Rayleigh}$, and aerosol optical depth, $\tau_{Aerossol}$, of the Automated Solar Radiometer (ASR) in measurements performed at SDSU site in USA.

Banda (nm)	$\tau_{Rayleigh}$	$\sigma_{Relativa}(\%)$	$\tau_{Aerossol}$	$\sigma_{Relativa}$ (%)
09/03/2015				
380	0.4184 ± 0.0018	0.43	0.2695 ± 0.0027	1.00
400	0.3380 ± 0.0014	0.41	0.2156 ± 0.0026	1.21
440	0.2279 ± 0.0010	0.44	0.2063 ± 0.0020	0.97
520	0.1148 ± 0.0005	0.44	0.1759 ± 0.0015	0.85
610	0.0599 ± 0.00025	0.42	0.1590 ± 0.0010	0.63
670	0.04095 ± 0.00017	0.42	0.1220 ± 0.0009	0.74
780	0.02214 ± 0.00009	0.41	0.0880 ± 0.0006	0.68
870	0.01425 ± 0.00006	0.42	0.0679 ± 0.0005	0.74
1030	0.00722 ± 0.00003	0.42	0.0579 ± 0.0004	0.69

The relationship between the wavelength dependence of the spectral aerosol optical depth and the size of atmospheric aerosol particles was first suggested by Ångström (**Equation 2.15**). A fitting was applied using the Ångström formula and from the Ångström parameters it was determined the horizontal visibility, VIS , and the aerosol optical depth at 550 nm, $\tau_{Aerosol,550nm}$. The results can be seen in **Table 4.9**.

Thome (2001) reported results from ground-based measurements of atmospheric conditions made at Railroad Valley Playa, Nevada, Roach Lake Playa, Nevada, and White Sands Missile Range, New Mexico. For comparison purposes, the aerosol optical depth at 550 nm was between 0.0207 and 0.1024 in these regions. Here, the aerosol optical depth at 550 ranged from 0.027 ± 0.012 (Brazil) to 0.155 ± 0.014 (SDSU site).

Table 4.9. Horizontal Visibility, VIS , and the aerosol optical depth at 550 nm, $\tau_{Aerosol,550nm}$.

Date	VIS (km)	$\tau_{Aerosol,550nm}$
West part of the Bahia State, Brazil		
07/23/2014	50.9 ± 2.4	0.033 ± 0.010
07/24/2014	54 ± 5	0.027 ± 0.012
07/25/2014	53 ± 5	0.029 ± 0.012
07/26/2014	41.3 ± 2.4	0.062 ± 0.018
Atacama Desert, Chile		
08/19/2014	31.3 ± 0.8	0.114 ± 0.009
08/20/2014	33.0 ± 1.8	0.102 ± 0.014
08/21/2010	37.4 ± 2.4	0.076 ± 0.013
08/22/2010	37.2 ± 2.1	0.077 ± 0.012
Algodones Dunes, USA		
03/09/2015	40.4 ± 2.3	0.066 ± 0.017
03/10/2015	48.0 ± 2.6	0.046 ± 0.014
South Dakota State University (SDSU) site, USA		
09/03/2015	34.6 ± 0.9	0.155 ± 0.014

Columnar water vapor was derived from the solar extinction data using a modified Langley approach (**Equation 2.19**). A plot of the left-hand side of this equation ($\ln(V_{936nm} \times D^2) + m \times \tau_{936nm}$) against m^c for water band (940 nm) yielded a straight line whose slope is proportional to the water content (see **Figure 4.10**). The R -squared and Chi-squared reduced statistics ranged from 0.79 to 0.99 and 0.23 to 3.04,

respectively (see **Table 10**). The values of these statistics indicate that the adjusted function (**Equation 2.19**) is truly appropriate.

The amount of water for every fieldwork and for each site utilized is shown in **Table 4.10**. As expected, the water content in the Atacama Desert was minimal: lower than 0.43 g/cm^2 for the four days and its uncertainties ranged from 0.33% to 4.66%. The region with the largest content of water was in site Brazil and the SDSU site: between 3.15 ± 0.03 from 3.409 ± 0.015 .

Figure 4.10. Modified Langley graph. In (a) on July 25th, 2014 in Brazil site, for water band of the CE317/CIMEL sun photometer; (b) on August 21st 2014 in Atacama Desert, Chile, for water band of the CE317/CIMEL sun photometer; (c) on March 9th 2015 in Algodones Dunes, USA, for water band of the Automated Solar Radiometer (ASR); and (d) on September 3th 2015 in SDSU site, USA, for water band of the Automated Solar Radiometer (ASR).

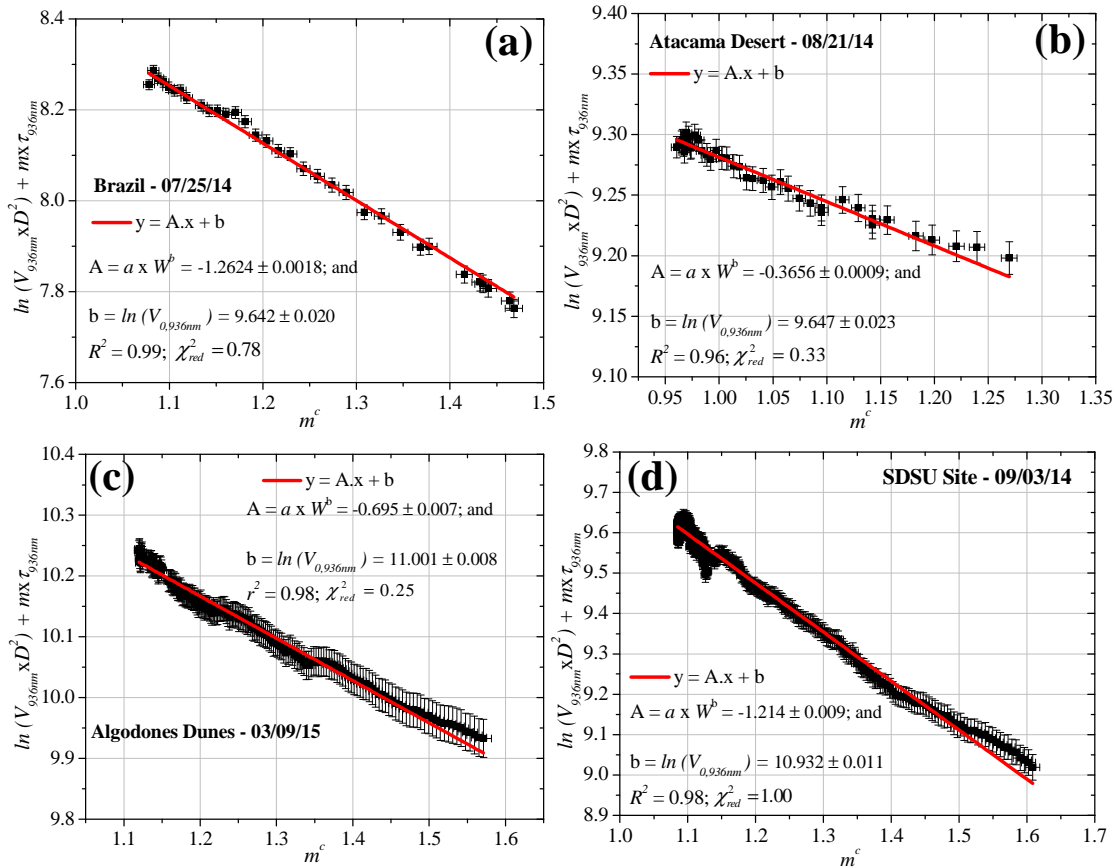


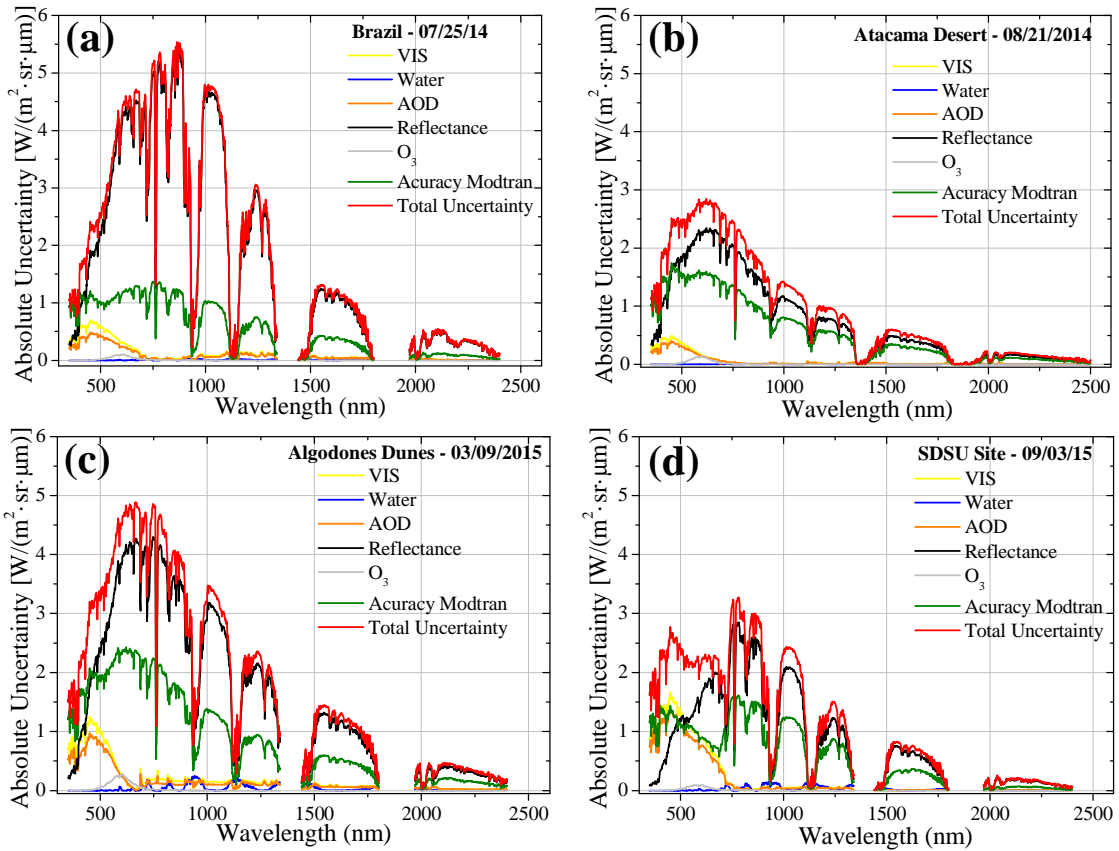
Table 4.10. Water vapor column abundance, W .

Date	W (g/cm ²)	$\sigma_{relative}$ (%)	R^2	χ^2_{red}
West part of the Bahia State, Brazil				
07/23/2014	3.40 ± 0.05	1.47	0.98	1.00
07/24/2014	3.409 ± 0.015	0.44	0.97	3.04
07/25/2014	3.402 ± 0.007	0.21	0.99	0.78
07/26/2014	3.30 ± 0.04	1.21	0.81	0.97
Atacama Desert, Chile				
08/19/2014	0.429 ± 0.020	4.66	0.79	1.00
08/20/2014	0.4318 ± 0.0023	0.53	0.88	0.44
08/21/2010	0.2986 ± 0.0010	0.33	0.96	0.33
08/22/2010	0.4267 ± 0.0018	0.42	0.91	0.39
Algodones Dunes, USA				
03/09/2015	1.055 ± 0.014	1.33	0.98	0.25
03/10/2015	0.476 ± 0.005	1.05	0.99	0.23
South Dakota State University (SDSU) site, USA				
09/03/2015	3.15 ± 0.03	0.95	0.98	1.00

4.1.3. MODTRAN

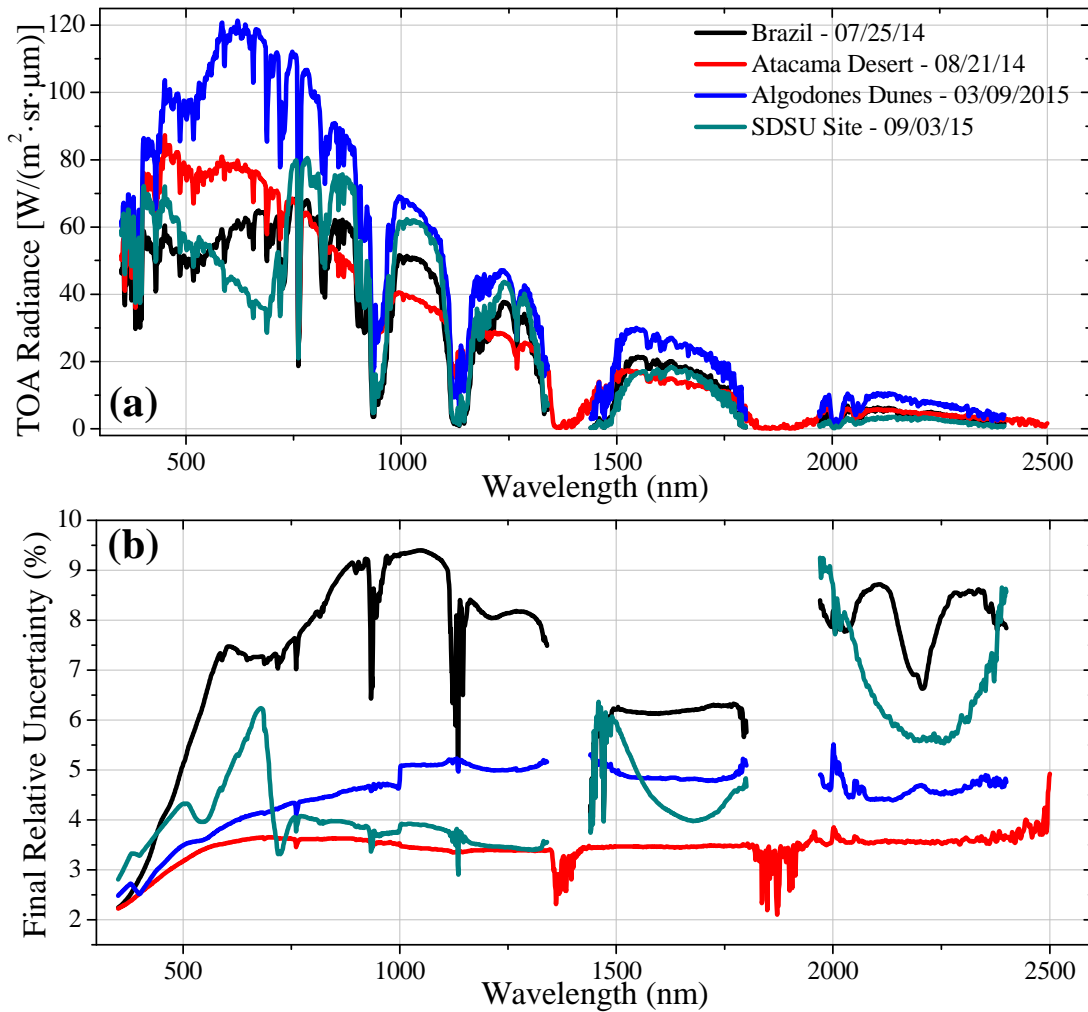
The surface reflectance factor and atmospheric data were inputs into a radiative transfer code (MODTRAN) to predict the top-of-the-atmosphere radiance. As described in the **section 3.2.4**, the TOA radiance estimation (or TOA reflectance) is incomplete unless accompanied with an uncertainty. In this work, six uncertainties sources were considered: (i) MODTRAN uncertainty itself (accuracy of MODTRAN); (ii) the reflectance factor of the surface (Reflectance); (iii) the aerosol optical depth (AOD); (iv) the water vapor column abundance (Water); (v) the ozone (O₃); and (vi) the horizontal visibility (VIS). **Figure 4.11** gives the graph of these uncertainties.

Figure 4.11. TOA radiance uncertainty predicted by MODTRAN. In (a) on July 25th, 2014 in Brazil site; (b) on August 21st 2014 in Atacama Desert, Chile; (c) on March 9th 2015 in Algodones Dunes, USA; and (d) on September 3th 2015 in SDSU site.



Every source of uncertainty depends on the wavelength. The main source of uncertainty, considering the four calibration sites, was the surface reflectance factor, which supports the importance of properly choosing a reference surface for calibration. The second major source of uncertainty, also for the four calibration sites, was the MODTRAN uncertainty itself (accuracy of MODTRAN). The uncertainty related to the visibility and aerosol has similar spectral behavior. This result is easily explained by the fact that these parameters are correlated. Uncertainties related to water and ozone, as expected, affect the spectral regions that are influenced by water vapor and ozone, respectively. These two uncertainties were less significant in the four calibration sites. **Figure 4.12** shows the values of the TOA radiance predicted by MODTRAN and its final relative uncertainty (in percentage).

Figure 4.12. In (a) TOA radiance predicted by MODTRAN; and (b) its final relative uncertainty (in percentage).



The reference surfaces that presented the highest final uncertainty were in both Brazil and the SDSU sites: between 2.24 - 9.40% and 2.80-9.25%, respectively. The reference surface in the Atacama Desert presented the lowest final uncertainties: from 2.22 to 3.85%. Finally, the lower uncertainty in Algodones Dunes site was 2.48% and highest uncertainty was 5.51%. These are the overall total uncertainty using the reflectance-based approach with each of the sites in the spectral region between 350-2500 nm. In the next two sections it will be presented, respectively, the final radiometric calibration results of the OLI/Landsat-8 and MUX/WFI/CBERS-4 using the reflectance-based approach.

4.1.4. OLI/Landsat-8 Radiometric Calibration

According to mentioned in the **section 3**, the calibration using the reference surface in Brazil and in Chile has been performed with OLI/Landsat-8. **Table 4.11** presents the band-averaged TOA radiance predicted by MODTRAN for each of the nine multispectral bands of OLI/Landsat-8 derived from the spectral curve in **Figure 4.12**. As expected, due to the results presented in the previous section, the uncertainty in the TOA radiance predicted by MODTRAN were higher for the surface located in Brazil (between 2.4-8.7% for the nine OLI/Landsat-8 spectral bands) than the uncertainties in Atacama Desert (less than 3.6% for the nine OLI/Landsat-8 spectral bands).

Table 4.11. TOA radiance predicted by MODTRAN and from image of the OLI/Landsat-8 using Brazil and Atacama Desert sites. In this table is also presented the percent difference (see **Equation 4.1**) and the residue (the difference between the predicted value and the observed value).

Band	Band-averaged TOA Radiance predicted by MODTRAN [W/(m ² ·sr·µm)]	Uncertainty [%]	TOA Radiance from OLI image [W/(m ² ·sr·µm)]	Uncertainty [%]	Difference [%]	Residue
West of Bahia State (Brazil)						
B1	54.6 ± 2.1	3.8	59.0 ± 0.6	1.0	-7.41	-2.02
B2	52.0 ± 2.4	4.6	55.2 ± 0.8	1.4	-5.74	-1.26
B3	54 ± 4	7.4	55.4 ± 1.0	1.8	-3.03	-0.45
B4	62 ± 4	6.5	64.8 ± 0.9	1.4	-5.14	-0.74
B5	60 ± 5	8.3	63.3 ± 1.3	2.1	-5.49	-0.64
B6	19.1 ± 1.2	6.3	19.48 ± 0.19	1.0	-2.04	-0.34
B7	4.6 ± 0.4	8.7	4.62 ± 0.10	2.2	0.21	0.03
B8	56 ± 4	7.1	59.5 ± 1.3	2.2	-5.34	-0.78
B9	0.125 ± 0.003	2.4	0.103 ± 0.017	16.5	21.8	1.27
Atacama Desert (Chile)						
B1	77.6 ± 2.2	2.8	81.1 ± 0.9	1.1	-4.35	-1.49
B2	79.1 ± 2.4	3.0	82.0 ± 1.2	1.5	-3.51	-1.07
B3	76.6 ± 2.6	3.4	78.3 ± 1.4	1.8	-2.08	-0.54
B4	75.6 ± 2.7	3.6	79.7 ± 1.5	1.9	-5.10	-1.31
B5	49.5 ± 1.8	3.6	53.0 ± 1.0	1.9	-6.69	-1.75
B6	14.6 ± 0.5	3.4	14.93 ± 0.16	1.1	-2.39	-0.68
B7	4.69 ± 0.17	3.6	4.69 ± 0.05	1.1	-0.12	-0.03
B8	76.4 ± 2.7	3.5	79.9 ± 1.6	2.0	-4.39	-1.13
B9	0.91 ± 0.03	3.3	0.861 ± 0.022	2.6	5.31	1.21

The radiometric calibration of the OLI/Landsat-8 sensor is well performed and it is supported by preflight, post launch on-board, and ground reference data (IRONS et al., 2012; ROY et al., 2014; CZAPLA-MYERS et al., 2015). Standard

Landsat-8 data products provided by the USGS EROS Center consist of quantized and calibrated scaled digital numbers (DN) representing multispectral image data. The products are delivered in 16-bit unsigned integer format and can be rescaled to the TOA reflectance and/or radiance using radiometric rescaling coefficients provided in the product metadata file (MTL file). Then, **Table 4.11** also presents the TOA radiance for each of the nine spectral bands of OLI/Landsat-8 derived from the image. To convert OLI/Landsat-8 data to TOA spectral radiance/reflectance it was used the rescaling factors provided by the metadata file, according to process described in **section 3.3.3**.

Table 4.12 presents both the band-averaged TOA reflectance predicted by MODTRAN for the nine OLI/Landsat-8 and spectral bands and TOA reflectance derived from the image of the OLI/Landsat-8.

Table 4.12. TOA reflectance predicted by MODTRAN and from image of the OLI/Landsat-8 using Brazil and Atacama Desert sites. In this table is also presented the percent difference (see **Equation 4.1**) and the residue (the difference between the predicted value and the observed value, divided by the associated uncertainty).

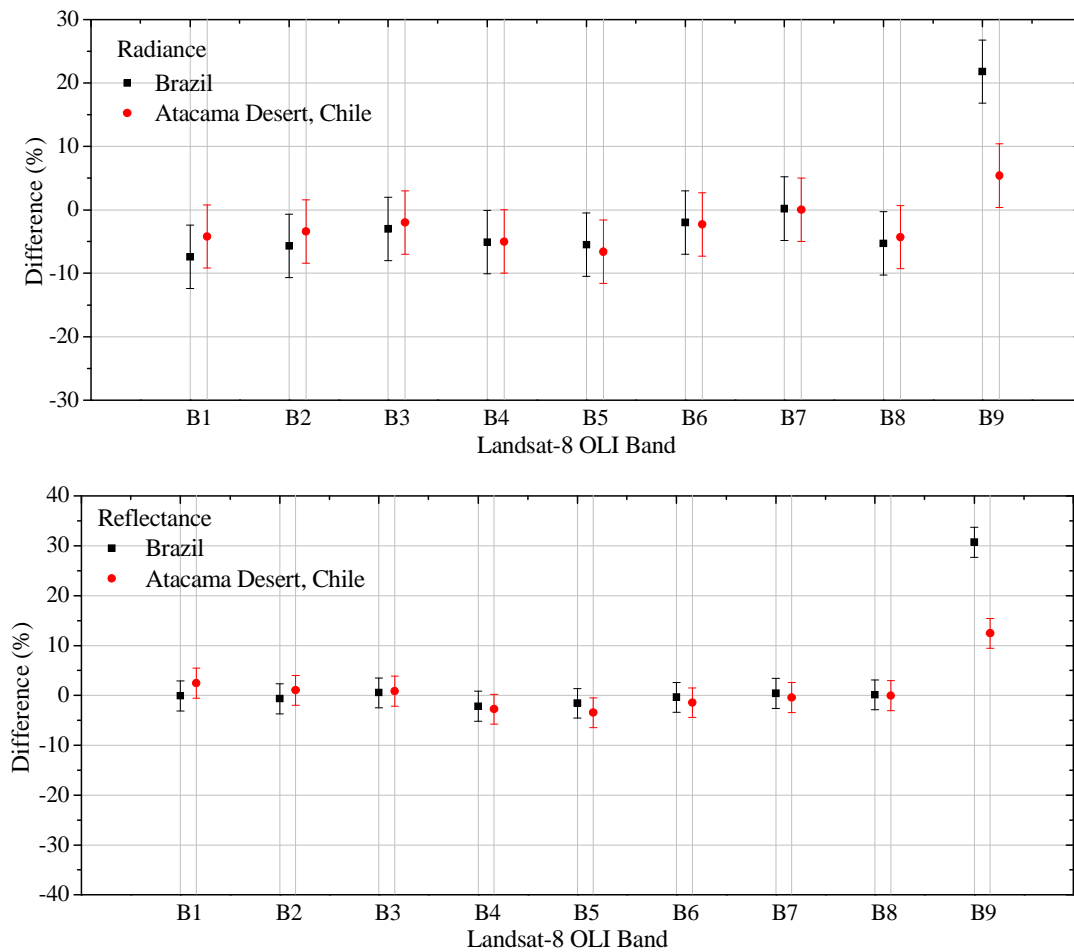
Band	Band-averaged TOA Reflectance predicted by MODTRAN [unitless]	Uncertainty [%]	TOA Reflectance from OLI image [unitless]	Uncertainty [%]	Difference [%]	Residue
West of Bahia State (Brazil)						
B1	0.135 ± 0.005	3.7	0.1354 ± 0.0014	1.0	-0.14	-0.04
B2	0.123 ± 0.006	4.9	0.1237 ± 0.0017	1.4	-0.68	-0.14
B3	0.135 ± 0.009	6.7	0.1346 ± 0.0023	1.7	0.51	0.07
B4	0.183 ± 0.013	7.1	0.1869 ± 0.0026	1.4	-2.19	-0.30
B5	0.293 ± 0.026	8.9	0.298 ± 0.006	2.0	-1.64	-0.18
B6	0.368 ± 0.022	6.0	0.369 ± 0.004	1.1	-0.40	-0.06
B7	0.261 ± 0.020	7.7	0.260 ± 0.006	2.3	0.40	0.05
B8	0.152 ± 0.010	6.6	0.152 ± 0.003	2.0	0.07	0.01
B9	0.00162 ± 0.00004	2.5	0.00124 ± 0.00021	16.9	30.7	1.78
Atacama Desert (Chile)						
B1	0.196 ± 0.006	3.1	0.1919 ± 0.0021	1.1	2.33	0.76
B2	0.191 ± 0.006	3.1	0.1894 ± 0.0027	1.4	0.94	0.27
B3	0.198 ± 0.007	3.5	0.196 ± 0.004	2.0	0.71	0.18
B4	0.230 ± 0.008	3.5	0.237 ± 0.004	1.7	-2.93	-0.74
B5	0.248 ± 0.009	3.6	0.258 ± 0.005	1.9	-3.62	-0.92
B6	0.287 ± 0.010	3.5	0.292 ± 0.003	1.0	-1.56	-0.44
B7	0.270 ± 0.010	3.7	0.2720 ± 0.0027	1.0	-0.62	-0.17
B8	0.209 ± 0.007	3.3	0.210 ± 0.004	1.9	-0.24	-0.06
B9	0.0120 ± 0.0004	3.3	0.01071 ± 0.00027	2.5	12.3	2.69

The results presented here are in percent difference form between radiance and reflectance values of OLI/Landsat-8 sensor and the prediction provided by the reflectance-based approach, according to equation:

$$Difference \ (%) = \left(\frac{Measured - OLI}{OLI} \right) \times 100 \quad (4.1)$$

where: *Measured* are the ground-based data (TOA radiance or TOA reflectance predicted by MODTRAN); and *OLI* are the data derived from OLI/Landsat-8 sensor (using radiometric rescaling coefficients provided by the metadata file - MTL file). The results are shown in **Figure 4.13**.

Figure 4.13. Comparison of radiance/reflectance reported by OLI/Landsat-8 and radiance/reflectance predicted with the reflectance-based approach. The error bars in this graph are the uncertainties of OLI/andsat-8 sensor (5% in radiance and 3% in reflectance).



OLI/Landsat-8 Band 9 (1360-1390 nm) provides detection of high-altitude cloud contamination that may not be visible in other spectral bands. This band contains a strong water absorption feature and facilitates the detection of cirrus clouds in OLI/Landsat-8 images. Cirrus clouds appear bright while most land surfaces will appear dark through cloud-free atmospheres containing water vapor. Thus, the uncertainties of OLI/Landsat-8 radiance measurements with band 9 in Brazil surface were high: 16.5% (see **Table 4.11**). Moreover, the band 9 uncertainty in the radiance measurement in Chile, region that exhibit low amount of water, was just 2.6% (see **Table 4.11**). This result clearly showed that it is essential using an area that presents low values of water vapor when performing the calibration of the OLI/Landsat-8 band 9. The authors in Czapla-Myers et al. (2015), for example, showed no calibration in band 9 of the OLI/Landsat-8 sensor due to this fact (high water content in the region).

The other spectral bands in **Figure 4.13** showed agreement between OLI/Landsat-8 and reflectance-based results. In the case of reflectance values the agreement was between 0.07-2.19% and 0.24-3.62% in measurements in Brazil and in Chile, respectively (except for cirrus band). The agreement of the radiance value was within 0.21% and 7.41% using the site in Brazil with the exception of the cirrus band. In Chile the absolute differences in the radiance in all spectral bands, including the cirrus band, were between 0.12-6.69%. The absolute differences between the reflectance values are smaller than the differences in radiance. These results were similar to those presented by Czapla-Myers et al. (2015) (see **Figure 3.2**).

4.1.5. MUX/WFI/CBERS-4 Radiometric Calibration

The reflectance-based approach calibration using the surface located in Algodones Dunes site has been performed with sensors on-board CBERS-4. **Table 4.13** and **Table 4.14** presents the band-averaged TOA radiance for each of the four multispectral bands of MUX/CBERS-4 and WFI/CBERS-4, respectively, derived from the spectral curve presented in **Figure 4.12**. These tables also present the average digital number from the image for each spectral band.

Recalling that the measured area in SDSU site was not seen by MUX/CBERS-4 sensor and, therefore, the MUX/CBERS-4 sensor did not acquire an image of the area.

Furthermore, as explained in **section 3.2.5**, to avoid the effect of sensor field of view and misregistration errors in choosing the proper image pixel corresponding to the reference surface, the SDSU site also was not used to calibrate the WFI/CBERS-4 sensor. However, the results with this site were presented with the purpose of understanding its characteristics.

Table 4.13. Summary of reflectance-based approach results for MUX/CBERS-4 using Algodones Dunes site.

Band	Band-averaged TOA Radiance predicted by MODTRAN [W/(m²·sr·μm)]	Uncertainty [%]	Digital Number	Uncertainty [%]
Algodones Dunes (USA)				
Blue	96 ± 3	3.1	56.4 ± 1.1	2.0
Green	108 ± 4	3.7	66.8 ± 1.6	2.4
Red	114 ± 5	4.4	74.2 ± 1.9	2.6
NIR	91 ± 4	4.4	66.7 ± 1.6	2.4

Table 4.14. Summary of reflectance-based approach results for WFI/CBERS-4 using Algodones Dunes and SDSU sites.

Band	Band-averaged TOA Radiance predicted by MODTRAN [W/(m²·sr·μm)]	Uncertainty [%]	Digital Number	Uncertainty [%]
Algodones Dunes (USA)				
Blue	96 ± 3	3.1	258.8 ± 2.7	1.0
Green	108 ± 4	3.7	212.7 ± 2.9	1.4
Red	114 ± 5	4.4	320 ± 5	1.6
NIR	92 ± 4	4.3	260 ± 3	1.2
SDSU Site (USA)				
Blue	58.2 ± 2.4	4.1	189 ± 9	4.8
Green	51.0 ± 2.1	4.1	148 ± 4	2.7
Red	36.9 ± 2.2	6.0	138 ± 10	7.2
NIR	70.7 ± 2.8	4.0	332 ± 10	3.0

Previous works (BIGGAR et al., 1994) with the reflectance-based method indicated that the method presented relative uncertainties of ± 5%, and it estimated that improvements should result in an uncertainty of ± 3% in the middle of the visible portion of the spectrum (CZAPLA-MYERS et al., 2015). Here, as can be seen in **Table 4.13** and **Table 4.14**, the uncertainty in the TOA radiance predicted by MODTRAN ranged from

3.1 to 4.4% in the four MUX/CBERS-4 and WFI/CBERS-4 spectral bands using Algodones Dunes site. As expected, due to the results achieved in **section 4.1.3**, the uncertainties were higher using the SDSU site: from 4.0 to 6.0%.

The radiometric calibration coefficient G (coefficient gain) was calculated for Algodones Dunes site. At this part of the present work was considered that the *offset* coefficient was zero, then, the **Equation 2.2** can be rewritten according to **Equation 4.2**. This assumption can be made because the *offset* is the radiance value corresponding to the DN (digital number) equal to zero, i.e. when there is no radiance in the sensor aperture the expected value of DN is zero. The **Table 4.15** lists the coefficients G .

$$G_{\lambda} = \frac{L_{\lambda}}{DN_{\lambda}} \quad (4.2)$$

Table 4.15. Radiometric calibration coefficient G (coefficient gain) of MUX/CBERS-4 and WFI/CBERS-4 using Algodones Dunes site.

Band	G	Uncertainty	G	Uncertainty
	[W/(m ² ·sr·μm)]	[%]	[W/(m ² ·sr·μm)]	[%]
Algodones Dunes (USA)				
	MUX		WFI	
Blue	1.71 ± 0.07	4.1	0.371 ± 0.013	3.5
Green	1.61 ± 0.07	4.3	0.506 ± 0.020	4.0
Red	1.54 ± 0.07	4.5	0.357 ± 0.016	4.5
NIR	1.37 ± 0.07	5.1	0.354 ± 0.016	4.5

4.2. Cross-Calibration Method

The cross-calibration between MUX/CBERS-4 and WFI/CBERS-4 sensors and the OLI/Landsat-8 (reference sensor) was performed based on simultaneous imaging of two different sites: (a) Libya-4, Africa; and (b) Atacama Desert, Chile. One of the most important steps during the cross-calibration is the Spectral Band Adjustment Factor (SBAF) assessment.

4.2.1. Spectral Band Adjustment Factor

The key to an accurate estimation of the Spectral Band Adjustment Factor (SBAF) is the representation of the spectral profile of the target and the Spectral Response Function (SRF) of the sensors. The two targets used in this work were Libya-4 and Atacama Desert, which the hyperspectral TOA reflectance profile are presented in **Figure 3.22** and **Figure 3.23**, respectively. The SRF of MUX/CBERS-4, WFI/CBERS-4 and OLI/Landsat-8 sensors are presented in **Figure 2.3**.

The result of the simulated reflectance factor histogram for the spectral band blue of the sensors MUX/CBERS-4, WFI/CBERS-4 and OLI/Landsat-8 (output quantity) for Libya-4 site and for two different correlations (minimum and maximum) can be seen in **Figure 4.14**. The results were similar to the other spectral bands (green, red and NIR). The simulated reflectance values in the MUX/CBERS-4 blue band for maximum correlation and for Libya-4 (**Figure 4.14c**) were between 0.228 and 0.288. However, for the same sensor, same band, same site, but different correlation (minimum) (**Figure 4.14d**) the simulated reflectance values ranged from 0,246 to 0,270.

The histogram shape gives further insight in to the behavior of the data, i.e. the histogram is an estimation of the probability distribution. Looking at **Figure 4.14** it can be seen that the results for the simulated reflectance were distributed according to a Gaussian (Normal). All normal distributions are characterized by two parameters: the mean and the standard deviation. The evaluation and estimation of these two parameters for each band of the sensors are presented in **Table 4.16** and **Table 4.17**. These tables present the MUX/CBERS-4, WFI/CBERS-4 and OLI/Landsat-8 average simulated reflectance for the two reference surfaces used in this work for cross-calibration (Libya-4 and Atacama Desert). The results are presented in the four analogous spectral bands (blue, green, red and NIR) and for the three different evaluated correlation matrices (maximum, minimum and intermediate correlation).

Figure 4.14. Simulated reflectance factor histogram for the spectral blue band and for Libya-4 site. In (a) and (b) sensor OLI/Landsat-8 with maximum and minimum correlation, respectively; (c) and (d) sensor MUX/CBERS-4 with maximum and minimum correlation, respectively; (e) and (f) sensor WFI/CBERS-4 with maximum and minimum correlation, respectively.

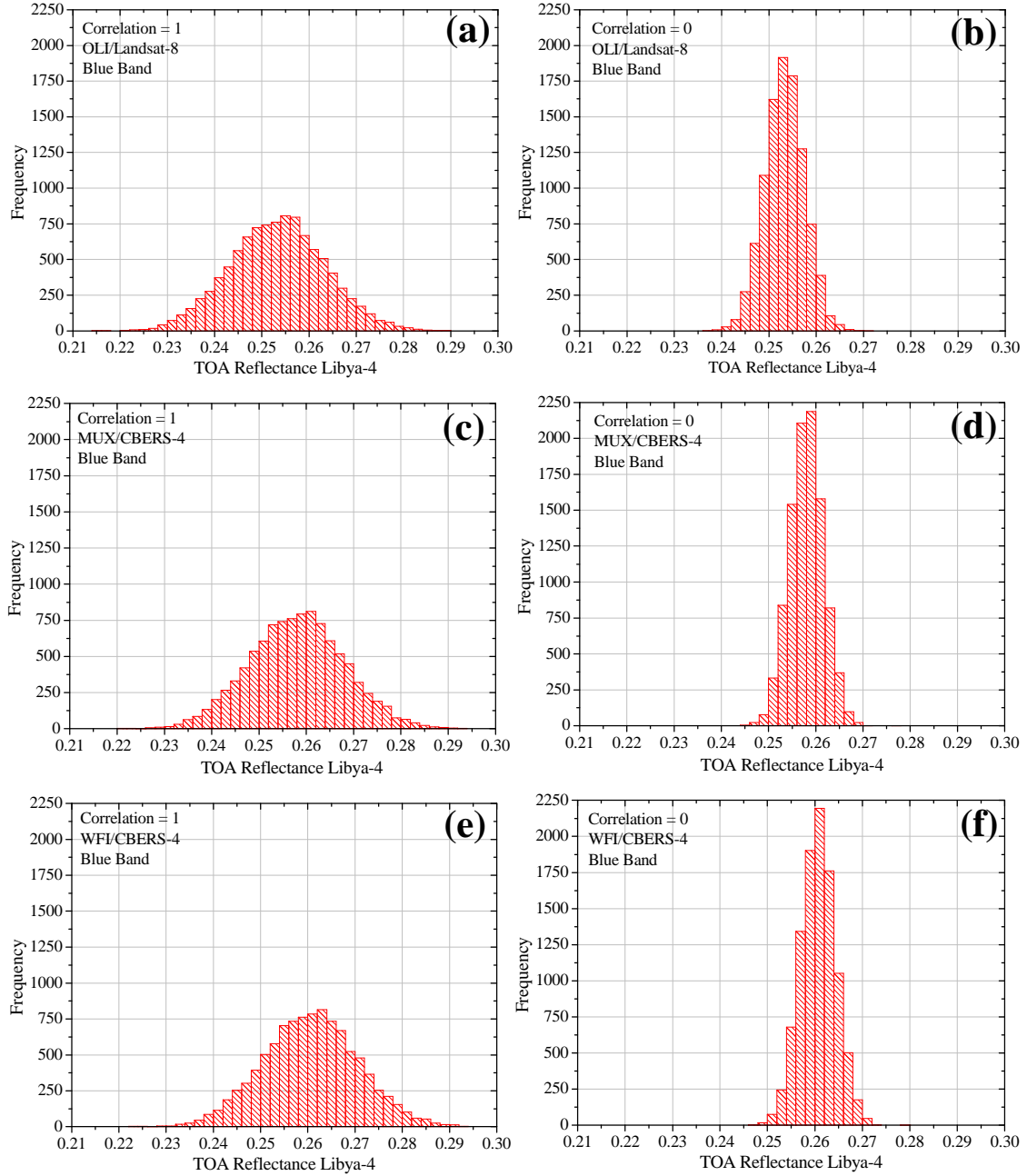


Table 4.16. Average MUX/CBERS-4, WFI/CBERS-4 and OLI/Landsat-8 simulated reflectance for Libya-4 site.

MUX/CBERS-4						
#	Maximum Correlation		Intermediate Correlation		Minimum Correlation	
Band	Simulated Reflectance	Uncertainty (%)	Simulated Reflectance	Uncertainty (%)	Simulated Reflectance	Uncertainty (%)
Blue	0.258 ± 0.010	3.89	0.258 ± 0.009	3.58	0.258 ± 0.004	1.64
Red	0.344 ± 0.010	2.86	0.344 ± 0.009	2.57	0.344 ± 0.003	1.16
Green	0.469 ± 0.012	2.46	0.469 ± 0.010	2.33	0.469 ± 0.005	1.24
NIR	0.534 ± 0.016	3.00	0.534 ± 0.013	2.37	0.534 ± 0.005	1.40
WFI/CBERS-4						
#	Maximum Correlation		Intermediate Correlation		Minimum Correlation	
Band	Simulated Reflectance	Uncertainty (%)	Simulated Reflectance	Uncertainty (%)	Simulated Reflectance	Uncertainty (%)
Blue	0.261 ± 0.010	3.86	0.261 ± 0.009	3.36	0.261 ± 0.004	1.40
Red	0.342 ± 0.010	2.88	0.342 ± 0.009	2.50	0.342 ± 0.003	1.00
Green	0.472 ± 0.012	2.46	0.472 ± 0.011	2.23	0.472 ± 0.005	0.97
NIR	0.532 ± 0.016	2.91	0.532 ± 0.013	2.36	0.532 ± 0.005	0.87
OLI/Landsat-8						
#	Maximum Correlation		Intermediate Correlation		Minimum Correlation	
Band	Simulated Reflectance	Uncertainty (%)	Simulated Reflectance	Uncertainty (%)	Simulated Reflectance	Uncertainty (%)
Blue	0.253 ± 0.010	3.99	0.253 ± 0.009	3.35	0.253 ± 0.004	1.38
Red	0.347 ± 0.010	2.81	0.347 ± 0.009	2.48	0.347 ± 0.004	0.99
Green	0.465 ± 0.011	2.46	0.465 ± 0.011	2.23	0.465 ± 0.006	0.96
NIR	0.591 ± 0.014	2.44	0.591 ± 0.014	2.46	0.591 ± 0.008	0.91

Table 4.17. Average MUX/CBERS-4, WFI/CBERS-4 and OLI/Landsat-8 simulated reflectance factor for Atacama Desert site.

MUX/CBERS-4						
#	Maximum Correlation		Intermediate Correlation		Minimum Correlation	
Band	Simulated Reflectance	Uncertainty (%)	Simulated Reflectance	Uncertainty (%)	Simulated Reflectance	Uncertainty (%)
Blue	0.191 ± 0.006	3.08	0.1910 ± 0.0023	1.22	0.1910 ± 0.0006	0.34
Red	0.198 ± 0.007	3.41	0.1975 ± 0.0027	1.35	0.1975 ± 0.0007	0.37
Green	0.229 ± 0.008	3.59	0.229 ± 0.004	1.57	0.2286 ± 0.0010	0.45
NIR	0.245 ± 0.009	3.59	0.245 ± 0.003	1.27	0.2451 ± 0.0008	0.33
WFI/CBERS-4						
#	Maximum Correlation		Intermediate Correlation		Minimum Correlation	
Band	Simulated Reflectance	Uncertainty (%)	Simulated Reflectance	Uncertainty (%)	Simulated Reflectance	Uncertainty (%)
Blue	0.191 ± 0.006	3.09	0.1907 ± 0.0024	1.25	0.1907 ± 0.0007	0.35
Red	0.197 ± 0.007	3.40	0.1971 ± 0.0027	1.35	0.1971 ± 0.0007	0.37
Green	0.229 ± 0.008	3.59	0.229 ± 0.004	1.58	0.2290 ± 0.0010	0.45
NIR	0.244 ± 0.009	3.59	0.244 ± 0.003	1.28	0.2439 ± 0.0008	0.33
OLI/Landsat-8						
#	Maximum Correlation		Intermediate Correlation		Minimum Correlation	
Band	Simulated Reflectance	Uncertainty (%)	Simulated Reflectance	Uncertainty (%)	Simulated Reflectance	Uncertainty (%)
Blue	0.191 ± 0.006	3.05	0.1911 ± 0.025	1.33	0.1911 ± 0.0007	0.39
Red	0.198 ± 0.007	3.42	0.198 ± 0.003	1.52	0.1977 ± 0.0009	0.44
Green	0.230 ± 0.008	3.59	0.230 ± 0.004	1.89	0.2301 ± 0.0013	0.58
NIR	0.248 ± 0.009	3.60	0.248 ± 0.005	2.05	0.2480 ± 0.0016	0.65

According **Table 4.16** and **Table 4.17** the correlation value did not change the average reflectance in each spectral band of the sensors, as expected. In all cases, the average reflectance remained the same. The only parameter that changed with the correlation is the uncertainty. The uncertainty increases with the correlation. For example, for the blue band the reflectance factor value at Libya-4 site and for MUX/CBERS-4 was 0.258 and its uncertainty was 3.89% when it used the maximum correlation (values equal to 1 throughout the correlation matrix). However, the uncertainty was 3.58% and 1.64% when it used intermediate (correlation ranged from 0.9 to 0.1) and minimum correlation, respectively.

Once the simulated TOA reflectance is calculated for each sensor, it is possible to estimate the SBAF using **Equation 2.26**. In this case the OLI/Landsat-8 TOA reflectance was divided by the MUX/CBERS-4 and WFI/CBERS-4 TOA reflectance, generating the SBAFs which are utilized to compensate the SRF differences between

sensors. The result of the SBAF histogram derived from the Monte Carlo simulation for the spectral blue band for Atacama Desert and Libya-4 site and for two different correlations (minimum and maximum) can be seen in **Figure 4.15** and **Figure 4.16**. **Table 4.18** and **Table 4.19** summarize the statistical results (average and its standard deviation) of the SBAFs for both sites.

Figure 4.15. Simulated SBAF histogram used to compensate the MUX/CBERS-4 TOA reflectance to match OLI/Landsat-8 TOA reflectance. In (a) Libya-4 site with maximum correlation; (b) Libya-4 site with minimum correlation; (c) Atacama Desert site with maximum correlation; (d) Atacama Desert site with minimum correlation.

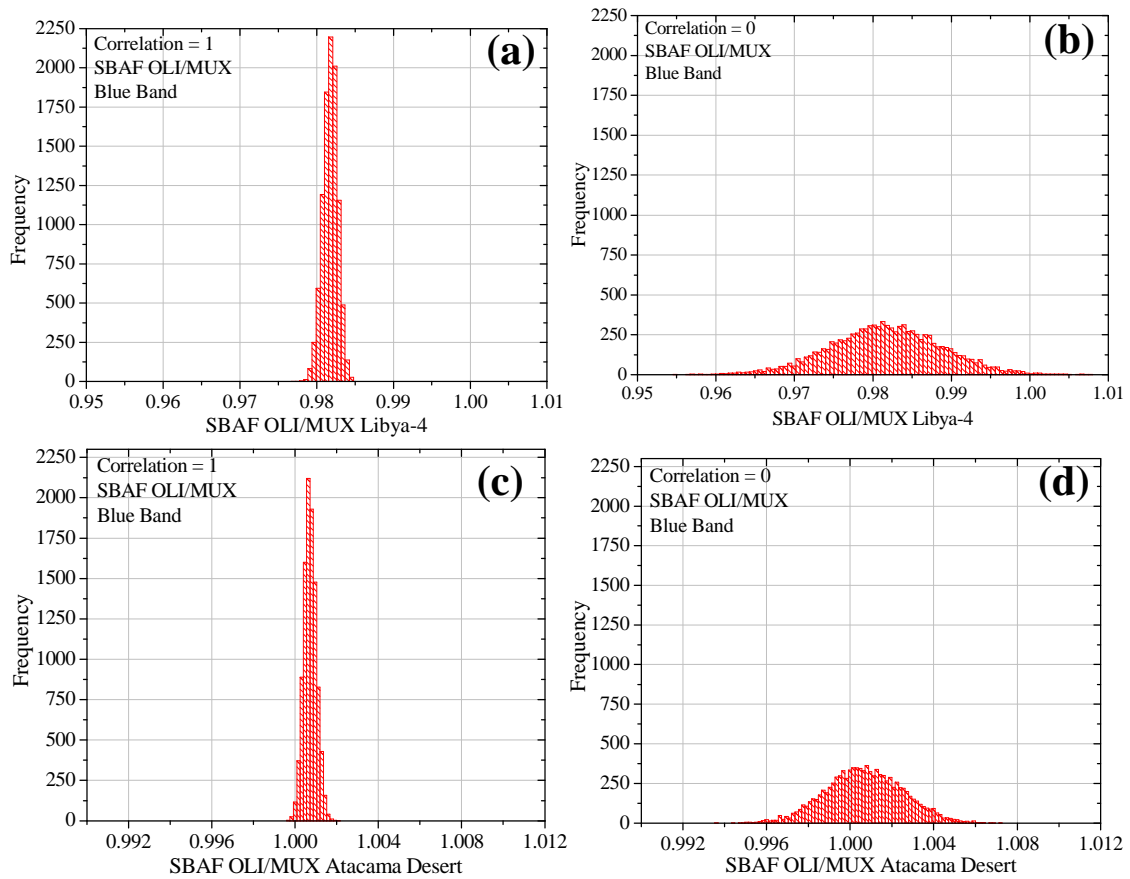


Figure 4.16. Simulated SBAF histogram used to compensate the WFI/CBERS-4 TOA reflectance to match OLI/Landsat-8 TOA reflectance. In (a) Libya-4 site with maximum correlation; (b) Libya-4 site with minimum correlation; (c) Atacama Desert site with maximum correlation; (d) Atacama Desert site with minimum correlation.

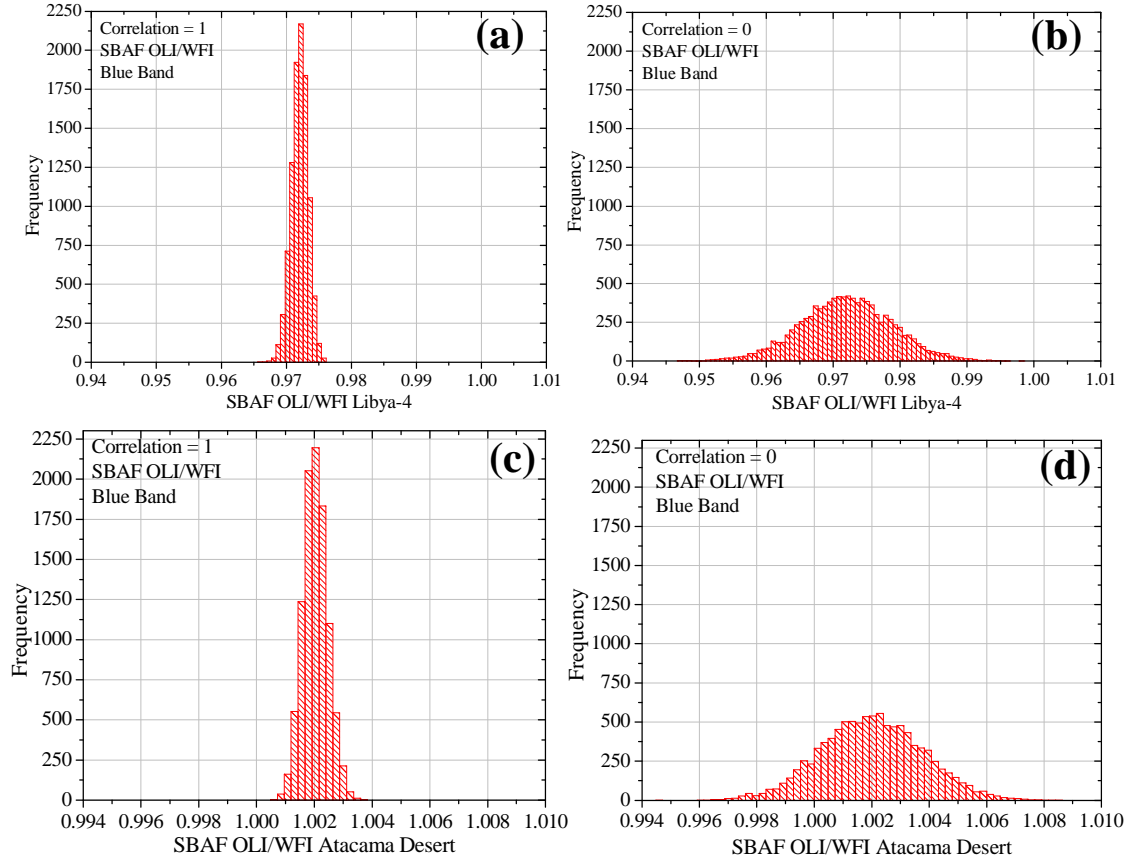


Table 4.18. SBAF and its uncertainty used to compensate the MUX/CBERS-4 TOA reflectance to match OLI/Landsat-8 TOA reflectance.

Libya-4						
#	Maximum Correlation		Intermediate Correlation		Minimum Correlation	
Band	SBAF	Uncertainty (%)	SBAF	Uncertainty (%)	SBAF	Uncertainty (%)
Blue	0.9818 ± 0.0010	0.10	0.982 ± 0.005	0.51	0.982 ± 0.007	0.73
Red	1.0083 ± 0.0006	0.06	1.008 ± 0.003	0.30	1.008 ± 0.005	0.48
Green	0.99236 ± 0.00008	0.01	0.992 ± 0.004	0.38	0.992 ± 0.007	0.66
NIR	1.108 ± 0.006	0.56	1.108 ± 0.020	1.79	1.108 ± 0.015	1.37
Atacama Desert						
#	Maximum Correlation		Intermediate Correlation		Minimum Correlation	
Band	SBAF	Uncertainty (%)	SBAF	Uncertainty (%)	SBAF	Uncertainty (%)
Blue	1.0007 ± 0.0003	0.03	1.0007 ± 0.0013	0.13	1.0007 ± 0.0018	0.18
Red	1.00112 ± 0.00016	0.02	1.0011 ± 0.0013	0.13	1.0011 ± 0.0018	0.18
Green	1.006230 ± 0.000021	0.002	1.0062 ± 0.0021	0.21	1.006 ± 0.003	0.32
NIR	1.01180 ± 0.00011	0.01	1.012 ± 0.005	0.49	1.012 ± 0.006	0.59

Table 4.19. SBAF and its uncertainty used to compensate the WFI/CBERS-4 TOA reflectance to match OLI/Landsat-8 TOA reflectance.

Libya-4						
#	Maximum Correlation		Intermediate Correlation		Minimum Correlation	
Band	SBAF	Uncertainty (%)	SBAF	Uncertainty (%)	SBAF	Uncertainty (%)
Blue	0.9721 ± 0.0013	0.13	0.972 ± 0.006	0.59	0.972 ± 0.007	0.71
Green	1.0151 ± 0.0007	0.07	1.015 ± 0.003	0.32	1.015 ± 0.005	0.48
Red	0.98622 ± 0.00006	0.01	0.986 ± 0.005	0.49	0.986 ± 0.007	0.71
NIR	1.111 ± 0.005	0.47	1.112 ± 0.021	1.88	1.111 ± 0.015	1.38
Atacama Desert						
#	Maximum Correlation		Intermediate Correlation		Minimum Correlation	
Band	SBAF	Uncertainty (%)	SBAF	Uncertainty (%)	SBAF	Uncertainty (%)
Blue	1.0020 ± 0.0004	0.04	1.002 ± 0.0014	0.14	1.0020 ± 0.0018	0.18
Green	1.00339 ± 0.00019	0.02	1.003 ± 0.0015	0.15	1.0034 ± 0.0018	0.18
Red	1.00438 ± 0.00005	0.005	1.004 ± 0.0022	0.22	1.004 ± 0.003	0.33
NIR	1.01688 ± 0.00012	0.01	1.017 ± 0.005	0.49	1.017 ± 0.006	0.61

The average TOA reflectance (**Table 4.16** and **Table 4.17**) and the average SBAF in each spectral band (**Table 4.18** and **Table 4.19**) did not change with different correlation values as expected. As in the previous results, the statistic parameter that changes with the correlation is the uncertainty. The correlation and the uncertainty of the SBAF have an inverse relationship: the higher correlation, the lowest is the SBAF uncertainty. For example, the uncertainty of the SBAF/MUX/OLI for the blue band and for the Libya-4 site was 0.10%, 0.51% and 0.73% for maximum, intermediate and minimum correlation, respectively.

Chander et al (2013a) evaluated the uncertainties inherent in the cross-calibration process, including contributions due to different spectral responses, spectral resolution, spectral filter shift, geometric misregistrations, and spatial resolutions. The authors suggested that the spectral uncertainty (spectral filter shift) is more dominant compared to other uncertainties (within 2.5%). Chander et al. (2013b) derived the SBAF using Hyperion/EO-1 lifetime data sets and their standard deviations were between 0.07-1.09%. Here, the uncertainties of the SBAFs ranged from 0.002% to 0.73%, for blue, green and red spectral bands, compatible with the values presented by Chander et al. (2013b). However, here the NIR band presented higher uncertainties (1.88%). The NIR band is the one with greatest Spectral Response Function (SRF)

difference between the MUX/CBERS-4, WFI/CBERS-4 and OLI/Landsat-8 sensors (see **Figure 2.3**). This would be the reason to present highest SBAF uncertainties.

Lastly, even for similar surface cover types the SBAFs were not identical from site to site. For Atacama Desert site and for NIR band, for example, the MUX/OLI/SBAF was equal to 1.012. However, for the same band but Libya-4 site the MUX/OLI/SBAF was equal to 1.108. This supports the concept that SBAFs depends on the spectral profile of the target. The accuracy of SBAF depends on how well the hyperspectral sensor describes the spectral signature of the target. To finalize the cross-calibration, the uncertainties considered were the intermediates (intermediate correlation). Thus, the final uncertainty is neither overestimated nor underestimated.

4.2.2. MUX/WFI/CBERS-4 Radiometric Calibration

The cross-calibration results between MUX/WFI/CBERS-4 and Landsat-8 using images acquired from Libya-4 and Atacama Desert sites can be seen in **Table 4.20** and **Table 4.21**. In order to convert the DN values of the OLI/Landsat-8 image to TOA radiance/reflectance the methodology described in **section 3.3.3** was applied. The radiance values of the MUX/CBERS-4 and WFI/CBERS-4 sensors, $L_{\lambda,MUX}$ and $L_{\lambda,WFI}$, were estimated using **Equation 3.15**, i.e. the radiance values were obtained from the OLI/Landsat-8 sensor radiance, $L_{\lambda,OLI}$.

Table 4.20. Summary of cross-calibration results for MUX/CBERS-4 using Libya-4 Dunes and Atacama Desert sites.

Band	TOA Radiance from OLI [W/(m ² ·sr·μm)]	Uncertainty [%]	Digital Number	Uncertainty [%]
Libya-4				
Blue	147 ± 9	6.1	90 ± 3	3.3
Green	183 ± 11	6.0	112 ± 4	3.6
Red	214 ± 13	6.1	131 ± 4	3.1
NIR	171 ± 11	6.4	118 ± 3	2.5
Atacama Desert (Chile)				
Blue	124 ± 7	5.6	74.0 ± 1.1	1.5
Green	122 ± 7	5.7	76.8 ± 1.2	1.6
Red	122 ± 7	5.7	78.0 ± 1.2	1.5
NIR	92 ± 5	5.4	65.8 ± 1.0	1.5

Table 4.21. Summary of cross-calibration results for WFI/CBERS-4 using Libya-4 Dunes and Atacama Desert sites.

Band	TOA Radiance from OLI [W/(m²·sr·μm)]	Uncertainty [%]	Digital Number	Uncertainty [%]
Libya-4				
Blue	149 ± 9	6.0	379 ± 12	3.2
Green	182 ± 11	6.0	373 ± 12	3.2
Red	214 ± 13	6.1	590 ± 17	2.9
NIR	173 ± 11	6.4	495 ± 13	2.6
Atacama Desert (Chile)				
Blue	124 ± 7	5.6	332 ± 4	1.2
Green	122 ± 7	5.7	274 ± 4	1.5
Red	122 ± 7	5.7	351 ± 5	1.4
NIR	93 ± 5	5.4	289 ± 4	1.4

The final uncertainty in the TOA radiance predicted by OLI/Landsat-8 sensor was lower than 6.4% and 5.7% in the four MUX/CBERS-4 and WFI/CBERS-4 spectral bands using Libya-4 and Atacama Desert sites, respectively. These are the overall total uncertainty using the cross-calibration method with each of the sites. Thereby, it can be concluded that the dominant source of uncertainty during the cross-calibration method is the uncertainty associated with the sensor chosen as reference. As mentioned earlier in the **section 3.3.5**, the OLI/Landsat-8 calibration is well defined, with 5% in terms of absolute at-aperture spectral radiance (IRONS et al., 2012; ROY et al., 2014). Thus, one of the disadvantages of cross-calibration is that the uncertainty of the sensor to be calibrated will be higher (or at least equal to) than the reference sensor.

For each calibration site (Libya-4 and Atacama Desert sites) it was calculated the radiometric calibration coefficient G (coefficient gain). In this part of the present work it was considered that the *offset* coefficient was zero (see **Equation 2.2**). This assumption can be made because the *offset* is the radiance value corresponding to the DN (digital number) equal to zero, i.e. when there is no radiance in the sensor aperture the expected value of DN is zero. The **Table 4.22** lists the coefficients G for each reference surface. Remembering, in the next section the combination of all results obtained with this technique (cross-calibration) and with the technique of reflectance-based approach (described in the previous section) was performed.

Table 4.22. Radiometric calibration coefficient G (coefficient gain) of MUX/CBERS-4 and WFI/CBERS-4 I using Libya-4 and Atacama Desert sites.

Band	G [W/(m ² ·sr·μm)]	Uncertainty [%]	G [W/(m ² ·sr·μm)]	Uncertainty [%]
Libya-4				
	MUX		WFI	
Blue	1.65 ± 0.12	7.3	0.394 ± 0.028	7.1
Green	1.63 ± 0.11	6.7	0.489 ± 0.034	7.0
Red	1.62 ± 0.11	6.8	0.363 ± 0.024	6.6
NIR	1.46 ± 0.10	6.8	0.349 ± 0.023	6.6
Atacama Desert (Chile)				
	MUX		WFI	
Blue	1.68 ± 0.10	6.0	0.375 ± 0.022	5.9
Green	1.58 ± 0.09	5.7	0.445 ± 0.026	5.8
Red	1.56 ± 0.09	5.8	0.346 ± 0.019	5.5
NIR	1.40 ± 0.08	5.7	0.322 ± 0.018	5.6

The value of the gain coefficient of each sensor should be the same (within the estimated uncertainty) for both reference surfaces and also equal to the gain determined with the reflectance-based approach, see **Table 4.15**. The uncertainties values were quoted as one-sigma (1-sigma) percentages (confidence level of 68.3 %). The gain coefficients for MUX/CBERS-4 sensor in the four spectral bands are all statistically the same considering “one-sigma”. For example, in the NIR band and using the reflectance-based approach (see **Table 4.15**) the gain coefficients was 1.37 ± 0.07 . This means the gain in this band may vary from 1.30 to 1.44 (with confidence level of 68.3%), which presents intersection with the gain values determined in this same spectral band but with cross-calibration technique. The gain using Libya-4 site was 1.46 ± 0.10 (from 1.36 to 1.56) and using Atacama Desert site was 1.40 ± 0.08 (from 1.32 to 1.48).

The gain coefficients for WFI/CBERS-4 sensor in the blue, red and NIR band are statistically the same considering “one-sigma”. However, the coefficients for WFI/CBERS-4 sensor in the green are statistically the same considering “two-sigma” (confidence level of 95,45%). For the green band and using the reflectance-based approach (see **Table 4.15**) the gain coefficients was $0.506 \pm 2 \times 0.020$ (from 0.466 to 0.546). The gain using Atacama Desert site was $0.445 \pm 2 \times 0.026$ (from 0.393 to 0.497)

and using Lybia-4 site was $0.489 \pm 2 \times 0.034$ (from 0.421 to 0.557). The coefficients estimated with each technique are statistically equal because there was intersection between the values.

Obviously, the more calibration points selected more accurate are the calibration results. In this part of the work the radiometric coefficients were estimated using only one point for the purpose of checking the individual results of each calibration site. However, in the next section the combination of all results obtained with this technique (cross-calibration) and with the reflectance-based approach was performed. This combination of the results also allowed evaluating whether the *offset* coefficients in each spectral band was compatible with zero.

4.3. Combination of techniques

The calibration coefficients, G_i and $offset_i$, for the MUX/WFI/CBERS-4 sensors were computed by linear regressing of their predicted at-sensor radiances against the measured raw counts. The measurements over Algodones Dunes, Lybia-4 and Atacama Desert were used together during the regression procedure to achieve a greater dynamic range. The regression slope provides the radiometric gains of the sensors. Two sets of calibration slopes were computed: one using the standard linear fit with an offset term, and second without an offset term, where the linear regression is forced through origin. The two sets of regression plots for the MUX/WFI/CBERS-4 bands are shown in **Figure 4.17** and **Figure 4.18**, respectively. The calibration coefficients derived from these linear regressions are listed in **Table 4.23**. The linear fitting was implemented using the Method of Least Squares as described in **section 2.4**.

Figure 4.17. Radiometric calibration of MUX/CBERS-4.

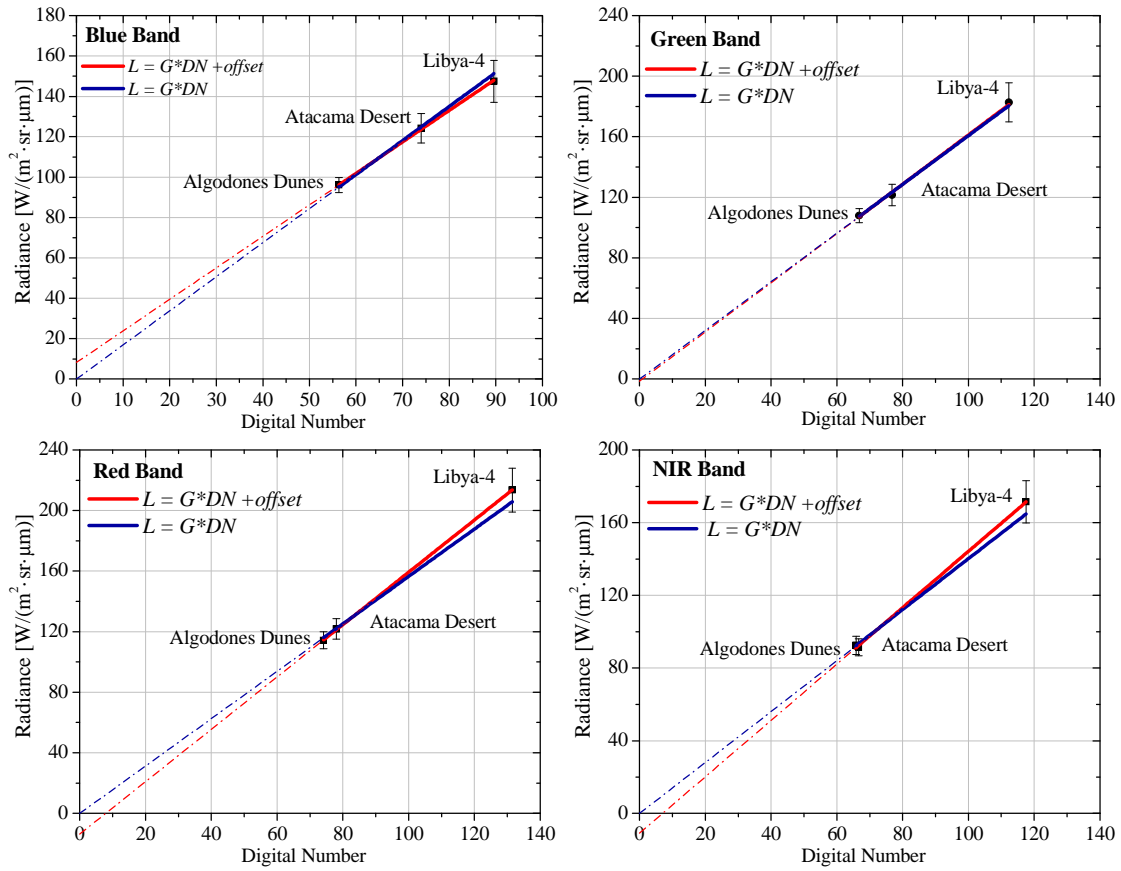


Figure 4.18. Radiometric calibration of WFI/CBERS-4.

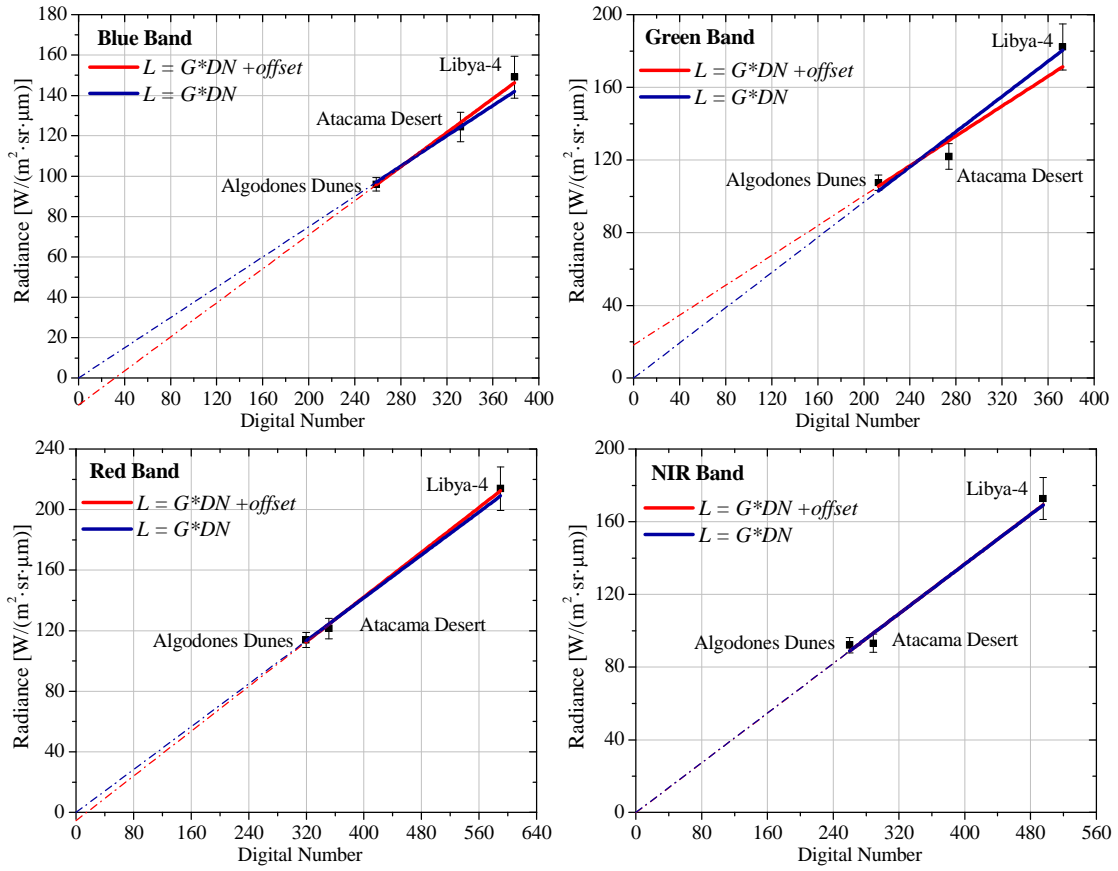


Table 4.23. Linear fits results corresponding to the plots shows in **Figure 4.17** and **Figure 4.18**.

Fit Equation: $L_i = G_i \times ND_i + offset_i$ [free intercept]					Fit Equation: $L_i = G_i \times ND_i$ [forced zero intercept]		
Band	Slope (G_i) [W/(m ² ·sr·µm)]	Intercept ($offset_i$) [W/(m ² ·sr·µm)]	R^2	χ^2_{red}	Slope (G_i) [W/(m ² ·sr·µm)]	R^2	χ^2_{red}
MUX/CBERS-4							
Blue	1.56 ± 0.29	8 ± 18	1.00	0.01	1.69 ± 0.05	0.99	0.11
Green	1.63 ± 0.30	-2 ± 22	0.99	0.11	1.61 ± 0.05	1.00	0.06
Red	1.73 ± 0.27	-14 ± 22	1.00	0.01	1.57 ± 0.05	0.99	0.19
NIR	1.55 ± 0.24	-11 ± 17	0.99	0.12	1.40 ± 0.05	0.99	0.26
WFI/CBERS-4							
Blue	0.42 ± 0.07	-13 ± 21	0.99	0.17	0.375 ± 0.010	0.98	0.28
Green	0.41 ± 0.08	18 ± 18	0.84	2.53	0.484 ± 0.014	0.89	1.76
Red	0.37 ± 0.06	-5 ± 20	0.99	0.26	0.354 ± 0.011	0.99	0.16
NIR	0.34 ± 0.05	0 ± 15	0.92	1.87	0.342 ± 0.011	0.96	0.94

It is important to emphasize that in this work the Level 1 (L1) image was used, i.e., the calibration coefficients estimated herein should be applied to L1 MUX/WFI /CBERS-4 images. Therefore, the radiometric coefficients may be invalidated if the Level 1 processing of the MUX/WFI/CBERS-4 images change.

For MUX/CBERS-4 sensor, the intercept coefficients in the fit with free intercept were (8 ± 18) , (-2 ± 22) , (-14 ± 22) and (-11 ± 17) for band blue, green, red and NIR, respectively. For WFI/CBERS-4 sensor, the intercept coefficients in the fit with free intercept were (-13 ± 21) , (18 ± 18) , (-5 ± 20) and (0 ± 15) for band blue, green, red and NIR, respectively. Then, taking into account the uncertainties, all the intercept coefficients (with free intercept) were consistent with zero, indicating that the $offset_i$ from **Equation 2.2** could be zero, i.e. there was no statistical evidence for using offsets other than zero for all spectral bands on both sensors. This result was expected, since when there is no incident energy on the sensor aperture the expected response is zero. Regarding the gain coefficients, the uncertainties ranged from 15% - 20%. Note that in this fitting, with free intercept, the degree of freedom was one.

The zero-intercept linear fits yield very good coefficients of determination, ranging from 0.89 to 1.00, in all four spectral bands of MUX/CBERS-4 and WFI/CBERS-4. The degree of freedom of the second fitting (zero-intercept) is equal two. In this case are expected values of χ_{red}^2 between 0.05 and 2.6, with a 90% confidence interval (VUOLO, 1996). All values of reduced chi-squared (**Table 4.23**) are within the range of acceptable values, indicating that the uncertainties are correctly estimated, and the function used represents well the data set.

The gain coefficients (forced zero-intercept) were 1.69, 1.61, 1.57 and 1.40 for MUX/CBERS-4 and 0.375, 0.484, 0.354 and 0.342 for WFI/CBERS-4 spectral bands blue, green, red and NIR, respectively, in units of $[W/(m^2 \cdot sr \cdot \mu m)]$. These coefficients were determined with uncertainties within 2.7% - 3.6% for all spectral bands on both sensors. In this fit, with zero-intercept, the degree of freedom is two. Furthermore, these coefficients agreed with the results obtained with each of the individual techniques (see **Table 4.15** and **Table 4.22**). To facilitate interpretation of the results in **Figure 4.19** and **Figure 4.20** is presented the graph of the gain coefficients for MUX/CBERS-4 and

WFI/CBERS-4 sensors, respectively, determined through each of the sites and also with the combination of techniques.

Figure 4.19. Gain coefficients of the MUX/CBERS-4 spectral bands.

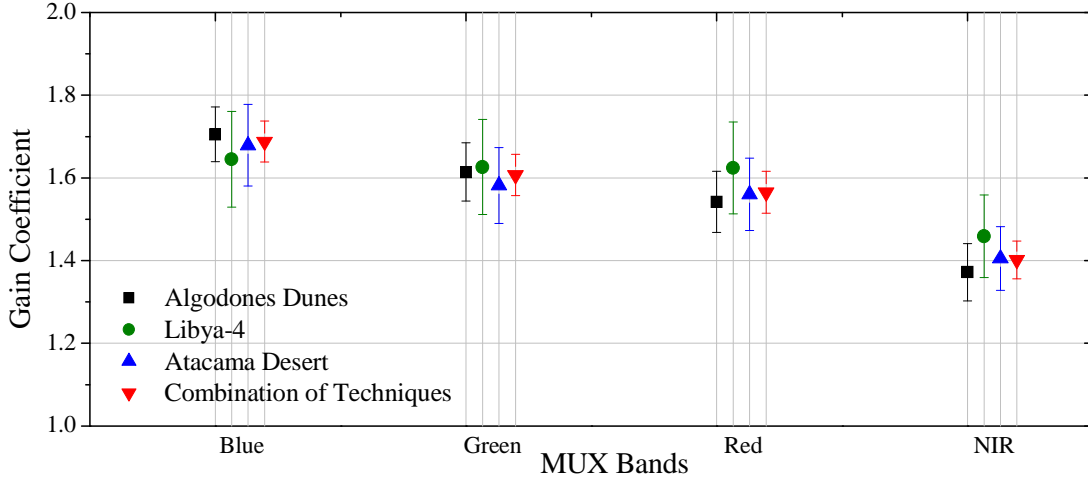
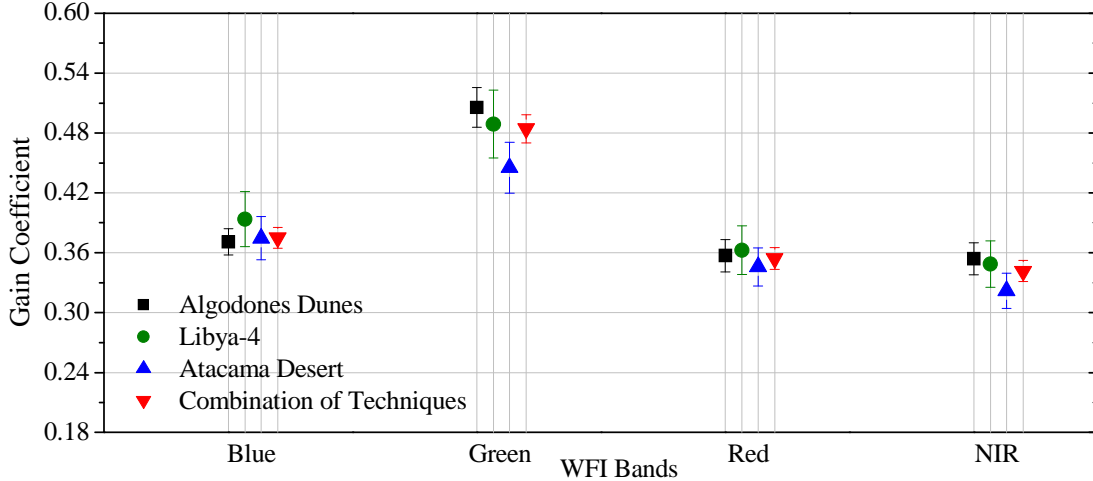


Figure 4.20. Gain coefficients of the WFI/CBERS-4 spectral bands.

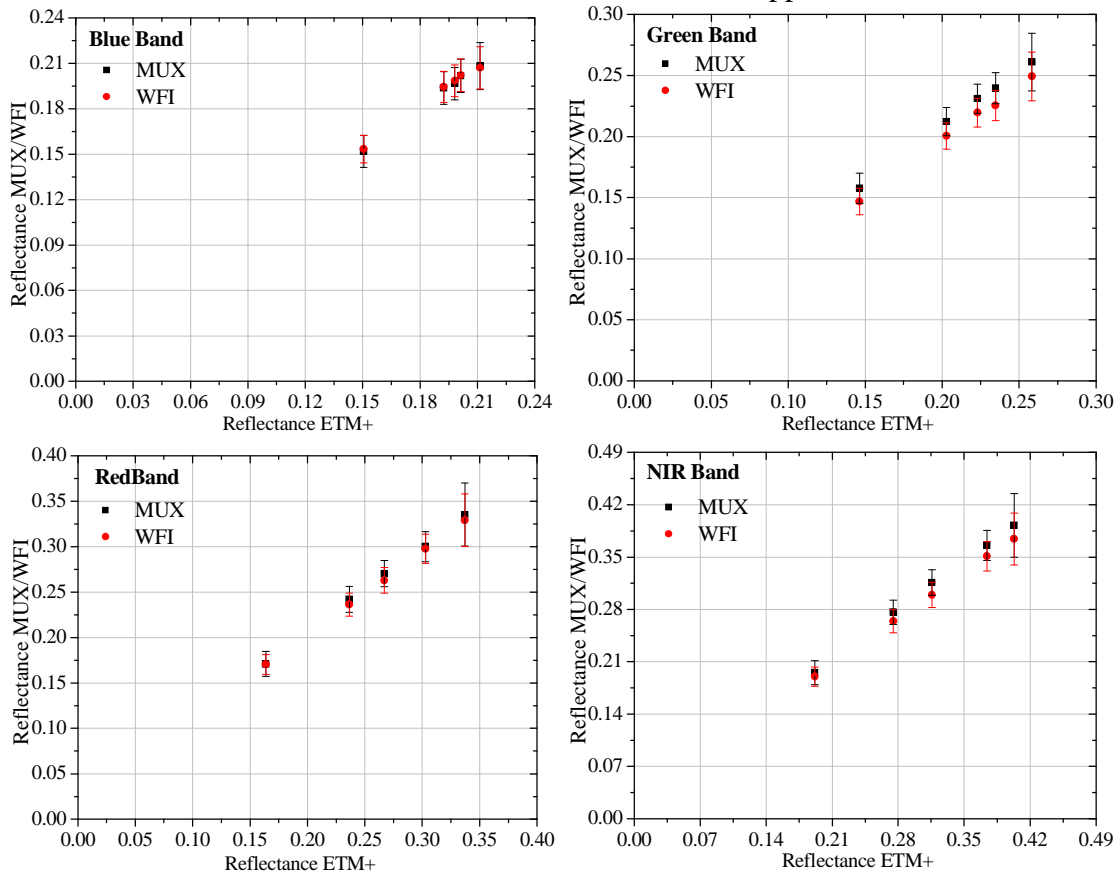


4.4. Validation of the MUX/WFI/CBERS-4 Radiometric Calibration Coefficients

As mentioned earlier, the calibration coefficient validation was performed using cross-calibration techniques. A comparison was done between ETM+/Landsat-7 and at-sensor reflectance derived from MUX/CBERS-4 and WFI/CBERS-4 measurements. To convert the DN values of the ETM+/Landsat-7 images to TOA reflectance the methodology presented in Chander et al. (2009) was applied. To determine TOA reflectance from MUX/CBERS-4 and WFI/CBERS-4 images **Equation 2.5** was

applied. The spectral radiance at the sensor's aperture was estimated by applying **Equation 2.2**, where the calibration coefficients, G_i and $offset_i$, are shown in **Table 4.23**. The solar exoatmospheric spectral irradiances for MUX/CBERS-4 and WFI/CBERS-4 bands are summarized in **Table 3.9**. **Figure 4.21** shows a graphic of ETM+/Landsat-7 TOA reflectance as a function of MUX/CBERS-4 and WFI/CBERS-4 TOA reflectance values for the five ROIs using the G_i with zero-intercept linear fits.

Figure 4.21. TOA reflectance comparison between ETM+/Landsat-7 and MUX/CBERS-4 and WFI/CBERS-4 after application of the SBAF.



As can be seen in **Figure 4.21**, the relationship between ETM+/Landsat-7 TOA reflectance and MUX/WFI/CBERS-4 TOA reflectance was linear, indicating that the sensor system (detector, amplifiers, converters, etc.) response is linear. Furthermore, the reflectance values of the three sensors (ETM+/Landsat-7, MUX/CBERS-4 and WFI/CBERS-4) are compatible within the associated uncertainty. **Table 4.24** provides the percentage differences in TOA reflectance of the five ROIs between MUX/WFI/CBERS-4 and ETM+/Landsat-7 similar bands after applied the spectral band adjustment factor. A negative sign in the difference indicates that the value

measured by the ETM+/Landsat-7 sensor band was higher than the corresponding CBERS-4 sensors bands.

Table 4.24. Landsat-7 and CBERS-4 percentage difference in TOA reflectance of the five ROIs.

Band	Diff After SBAF ETM+/MUX	Diff After SBAF ETM+/WFI	Diff After SBAF ETM+/MUX	Diff After SBAF ETM+/WFI
$L_i = G_i \times ND_i + offset_i$				
ROI 1				
Blue	4.40 %	-4.24 %	0.87 %	1.85 %
Green	6.10 %	12.84 %	7.85 %	0.43 %
Red	-7.82 %	0.65 %	4.45 %	4.15 %
NIR	-9.36 %	-1.43 %	1.95 %	-0.85 %
ROI 2				
Blue	1.73 %	-0.93 %	0.72 %	1.09 %
Green	3.76 %	3.85 %	4.69 %	-1.12 %
Red	-3.09 %	-1.24 %	2.37 %	-0.08 %
NIR	-4.31 %	-4.47 %	0.50 %	-3.91 %
ROI 3				
Blue	-1.23 %	-3.01 %	-1.51 %	-2.10 %
Green	0.55 %	-2.37 %	1.05 %	-3.50 %
Red	-1.56 %	-1.91 %	-0.55 %	-2.35 %
NIR	-2.84 %	-7.70 %	-2.66 %	-7.16 %
ROI 4				
Blue	0.81 %	-0.97 %	0.20 %	0.42 %
Green	2.96 %	1.81 %	3.70 %	-1.42 %
Red	-2.44 %	-2.03 %	1.32 %	-1.46 %
NIR	-2.85 %	-5.80 %	-0.02 %	-5.25 %
ROI 5				
Blue	0.01 %	-1.38 %	-0.77 %	0.17 %
Green	1.46 %	-1.14 %	2.12 %	-3.92 %
Red	-3.23 %	-1.69 %	-0.92 %	-1.71 %
NIR	-3.32 %	-6.69 %	-2.33 %	-6.14 %

On average the absolute difference between MUX/CBERS-4 and EMT+/Landsat-7 in the analogous bands was 3.2% and 2% when it was used the calibration coefficients determined with free intercept and when forced zero intercept, respectively. The absolute difference between WFI/CBERS-4 and EMT+/Landsat-7 was on average 3.3% and 2.5% with free intercept and forced zero intercept, respectively. This result reinforces the idea that the coefficient $offset_i$ from **Equation 2.2** is zero (as mentioned earlier), since the difference between MUX/WFI/CBERS-4 and EMT+/Landsat-7 was lower when it uses only the gain coefficient (forced zero intercept).

A convenient way to assess the consistency of these results is to compare them with the calibration uncertainties. As mentioned in **section 3.4**, the absolute calibration uncertainties in the spectral bands of the EMT+/Landsat-7 are specified to be within 5% (MARKHAM and HELDER, 2012). Furthermore, the uncertainties in the MUX/CBERS-4 and WFI/CBERS-4 gain coefficients for zero-intercept linear fits ranged from 2.7% to 3.6%, therefore, the associated uncertainties cover the differences. Thus, in all four MUX/WFI/CBERS-4 spectral bands, these results were well within the specified calibration uncertainties. Remembering that the uncertainties values were quoted with confidence level of 68.3 % (as one-sigma percentages).

5 CONCLUSIONS AND RECOMMENDATIONS

Remote sensing sensors need to be radiometric calibrated if the data generated by them are used for quantitative investigations. The absolute radiometric calibration relates the digital number to the average incident radiance in each spectral band of the sensor. The main objective of the present work was to develop a statistical methodology to evaluate the uncertainties inherent in the in-flight absolute radiometric calibration of Earth observation sensors. Several sources of uncertainties inherent in the reflectance-based approach and the cross-calibration method process have been quantified in the spectral region of the visible, near-infrared and short wave-infrared. In this section the conclusion reached are presented. Additionally, in order to improve future works on this topic some relevant recommendations were also included.

The methodology developed and tested confirms the hypothesis that the method proposed here is compatible and comparable with other methods practiced by the international science community of satellite radiometric calibration. The Monte Carlo, for example, proved to be efficient method to estimate uncertainties in some parts of the absolute radiometric calibration process. In fact, in certain parts of the calibration process, where there are correlations between the inputs variables and/or the system is nonlinear, the Monte Carlo might be more appropriate than the classical approach. In future studies it is suggested to use Monte Carlo method to assess the uncertainties taking into account all stages of a complete absolute calibration mission.

In addition, Brazil now has autonomy and reliability in the data provided by sensors of national Earth observation program.

(a) Regarding the reflectance-based approach:

- ✓ It is important to characterize in the laboratory all instruments that are used in the fieldwork to ensure reliability in the measurements acquired with them;
- ✓ The spectroradiometer instrumental uncertainties were lower than 1% in the spectral range of 350 to 2500 nm. When performing various measurements in

laboratory under exactly the same conditions the results variations obtained with the FieldSpec were minimal;

- ✓ Suitable calibration of the reference panel is required to assure valid reflectance factor data. Then, it is essential that the reference panel to be calibrated since the panels do not reflect all of the incidence radiation (the panel reflectance factor is not one or the same at the entire spectrum), and further, its reflectance can be dependent on the illumination angle. The reference panel relative uncertainties were within 0.03%-0.21% in the spectral range of 350 to 2500 nm;
- ✓ The columnar water vapor was derived from the spectral band of the solar photometer centered at 940 nm using a modified Langley approach with a relative uncertainty lower than 5%. In general, the four studied sites presented low aerosol loading and the aerosol optical depth (AOD) relative uncertainties ranged from 2-12% in Brazil, 1-5% in Chile, 1-11% in Algodones Dunes and lower than 1.2% in SDSU site. The aerosol concentration can be obtained through the AOD at 550 nm, $\tau_{Aerosol,550nm}$, with an uncertainty between 8% and 44% or through the visibility (VIS) with a uncertainty within 3-9%. The AOD uncertainties may seem high, but the most important are their impact on MODTRAN performance (discussed below);
- ✓ The main component of the reflectance-based method is the retrieved surface reflectance at the time that the sensor overpasses on the reference surface. The relative uncertainty of the Algodones Dunes and Atacama Desert reflectance factors was lower than 5%; and the relative uncertainty of the Brazil and SDSU reflectance factors ranged from 3% to 10%;
- ✓ The reflectance-based approach characterizes the atmosphere and the reference surface of a test site to use as inputs in a radiative transfer mode (MODTRAN) to predict at-sensor radiance. These two parameters collected during the fieldwork were estimated with the associated uncertainties; therefore, it is also

necessary to verify the impact of the input parameters uncertainties on MODTRAN;

- ✓ In addition to the MODTRAN uncertainty itself, five others source of uncertainty were considered: (i) the reflectance factor of the surface; (ii) the aerosol optical depth; (iii) the water vapor column abundance; (iv) the ozone; and (v) the horizontal visibility. All sources of uncertainties depend on the wavelength. The main source of uncertainty was the surface reflectance factor (reported above). The second major source of uncertainty, for the four calibration sites, was the accuracy of MODTRAN itself (2%). The uncertainty related to both the visibility and the aerosol presented similar spectral behavior. Uncertainties related to water and ozone contents, as expected, affect the spectral regions that are influenced by water vapor and ozone, respectively, and these uncertainties were less significant;
- ✓ The calibration through reflectance-based approach was much more sensitive to the surface reflectance characterization than the atmospheric characterization parameters. However, as previously mentioned, the atmospheric conditions parameters are required for accurate results;
- ✓ The final uncertainty of the TOA radiance predicted by MODTRAN in Brazil and in SDSU was lower than 10%. The final uncertainty of the TOA radiance predicted by MODTRAN in Atacama Desert and in Algodones Dunes site was lower than 5.5%. These values are the overall total uncertainty of the reflectance-based method in the spectral range of 350 to 2400 nm;
- ✓ The results demonstrated that both reference surfaces located in South America (Chile and Brazil) can be utilized as a radiometric calibration test site for optical sensors in the solar reflected spectrum. However, the Atacama Desert in Chile is more appropriate since the uncertainties were much lower than those estimated in the Brazil surface;

(b) Regarding the OLI/Landsat-8 radiometric calibration results:

- ✓ The results presented here were in the form of relative (percent) difference between radiance and reflectance values measured by OLI/Landsat-8 sensor and the prediction provided by the reflectance-based approach. The absolute differences between the reflectance values were smaller than the differences in radiance. In the case of reflectance values the agreement was less than 3.6% (except for cirrus band). The agreement of the radiance value was within 0.1% and 7.4% (except for cirrus band);

(c) Regarding the cross-calibration method:

- ✓ It is indispensable to select a well spectral characterized reference surface, since the differences in Spectral Response Function (SRF) between the sensors must be quantified. This compensation can be achieved by the use of the SBAFs. The SBAF are developed for the analogous spectral bands of the involved sensors. To estimate the SBAF the spectral signature of the target (reference surface) must to be known during the overpass time. The determination of the spectral profile of the target can be obtained from ground measurements or from an on-orbit hyperspectral sensor (Hyperion/EO-1 sensor, for example). These two approaches were used in this work;
- ✓ The SBAFs were developed for analogous OLI/Landsat-8 and MUX/WFI/CBERS-4 spectral bands. The results suggested that the uncertainty of the SBAF is dependent on the correlation between the input variables: the higher correlation, the lower the SBAF uncertainty. For maximum correlation (values equal to one throughout the correlation matrix) the uncertainties ranged from 0.002% to 0.56%. Moreover, the uncertainties were within 0.18% to 1.38% when it was considered minimum correlation (values equal to zero throughout the matrix, except for the main diagonal that contains values of 1). The accuracy of SBAF depends on how well the hyperspectral sensor defines the spectral signature of the target and also of the SRF uncertainty;

- ✓ The cross-calibration between both MUX/CBERS-4 and WFI/CBERS-4 and the OLI/Landsat-8 on-board Landsat-8 was performed using the Libya-4 and Atacama Desert sites. The uncertainty in cross-calibration (the TOA radiance estimated from OLI/Landsat-8 sensor) using the Libya-4 and Atacama Desert sites was lower than 6.4%. The dominant source of uncertainty during the cross-calibration method is the uncertainty associated with the sensor chosen as the reference. The OLI/Landsat-8 (reference sensor used here) produces calibrated data with uncertainty of less than 5% in the radiance for each of the spectral bands;

(d) Regarding the CBERS-4 radiometric calibration (combination of techniques):

- ✓ The in-flight absolute calibration coefficients for the MUX/CBERS-4 and WFI/CBERS-4 sensors were computed by linearly regressing their predicted at-sensor radiances against the measured digital number from the image. The measurements over Algodones Dunes, Libya-4 and Atacama Desert sites were used together during regression to achieve a greater dynamic range. There was no statistical evidence for using offsets other than zero for all spectral bands on both sensors;
- ✓ The gain coefficients are now available: 1.69 ± 0.05 , 1.61 ± 0.05 , 1.57 ± 0.05 and 1.40 ± 0.05 for MUX/CBERS-4 and 0.375 ± 0.010 , 0.484 ± 0.014 , 0.354 ± 0.011 and 0.342 ± 0.011 for WFI/CBERS-4 spectral bands blue, green, red and NIR, respectively, in units of $[W/(m^2 \cdot sr \cdot \mu m)]$. These coefficients were determined with relative uncertainties lower than 3.6%. It is noteworthy that this current work is the first one to present the uncertainty in the CBERS sensors series calibration. Thus, the results achieved here are considered an important progress in the calibration of the Brazilian and Chinese satellite sensors;

- ✓ It is important to emphasize the need to preserve the accuracy of the MUX/CBERS-4 and WFI/CBERS-4 absolute radiometric calibration by recalibration on-orbit regularly. It is necessary to perform evaluations of the sensor radiometry once on-orbit, as well as during its operational life time, to ensure the on-orbit radiometric stability of the instruments;
- (e) Regarding the Validation of the MUX/WFI/CBERS-4 radiometric calibration coefficients:
- ✓ It is recommended to use the reflectance measurements to validate the data acquired with the sensors instead of radiance data. Firstly, the TOA reflectance corrects for the variation in the Earth-Sun distance between data acquisition. Secondly, the TOA reflectance removes the cosine effect of different illumination angle (solar zenith angle). Lastly, the TOA reflectance compensates the different values of the exoatmospheric solar irradiance;
 - ✓ A procedure to validate the estimated coefficients was performed using cross-calibration techniques. On average the percent disagreement between the EMT+/Landsat-7 and at-sensor reflectance reported using the above mentioned coefficients calibration of MUX/CBERS-4 and WFI/CBERS-4 was, respectively, 2% and 2.5% (after application of the spectral band adjustment). These outcomes indicate good agreement with the well accepted EMT+/Landsat-7 results.

REFERENCES

- ASSOCIAÇÃO BRASILEIRA DE NORMAS TÉCNICAS (ABNT); INSTITUTO NACIONAL DE METROLOGIA (INMETRO). **Guia para a expressão da incerteza de medição**: terceira edição brasileira. 3. ed. Rio de Janeiro: ABNT, INMETRO, 2003. 120 p.
- AMBINAKUDIGE, S.; CHOI, J.; KHANAL, S. A comparative analysis of CBERS and Landsat data. In: AMERICAN SOCIETY OF PHOTOGRAMMETRY AND REMOTE SENSING (ASPRS), ANNUAL CONFERENCE, 2009, Baltimore, Maryland. **Proceedings...** 2009. Available: <<http://www.asprs.org/a/publications/proceedings/baltimore09/0005.pdf>>. Access: 10 may 2016.
- ANALYTICAL SPECTRAL DEVICES, Inc. (ASD). **Technical guide**. 3. ed. Boulder, Colorado, USA: Analytical Spectral Devices, 1999. 140 p.
- ANALYTICAL SPECTRAL DEVICES, Inc. (ASD). **User's guide**. Boulder, Colorado, USA: Analytical Spectral Devices, 2002. 136 p.
- AVELISIO, M. A.; MELO, M. C.; PINTO C. T. ; CASTRO, R. M. ; MOREIRA, R.C. ; ESPOSITO, E. S. C. Caracterização radiométrica de sensores eletroópticos. In: SEMINÁRIO DE INICIAÇÃO CIENTÍFICA DO IEAV, 1., 2007, São José dos Campos. **Livro de resumos...** São José dos Campos: IEAV, 2007, p. 27-28.
- BERK, A.; BERNSTEIN, L. S.; ANDERSON, G. P.; ACHARYA, P. K.; ROBERTSON, D. C.; CHETWYND, J. H.; ADLER-GOLDEN, S. M. MODTRAN Cloud and multiple scattering upgrades with application to AVIRIS. **Remote Sensing of Environment**, v. 65, n. 3, p. 367-375, 1998.
- BERK, A.; ANDERSON, G. P.; ACHARYA, P. K.; SHETTLE, E. P. **MODTRAN 5.2.1 user's manual**. Spectral Sciences Inc., Air Force Research Laboratory: Burlington, MA, USA and Hanscom AFB, MA, USA, 2011, 69 p.
- BEVINGTON, P. R.; ROBINSON, D. K. **Data reduction and error analysis**: for the physical sciences. 3. ed. New York, USA: McGraw-Hill Higher Education, 2003. 320p.
- BIGGAR, S. F.; SLATER, P. N.; GELLMAN, D. I. Uncertainties in the in-flight calibration of sensors with reference to measured ground sites in the 0.4-1.1 mm range. **Remote Sensing of Environment**, v. 48, n. 2, p. 245-252, 1994.
- BIGGAR, S.F.; THOME, K.J.; WISNIEWSKI, W. Vicarious radiometric calibration of EO-1 sensors by reference to high-reflectance ground targets. **IEEE Transactions on Geoscience and Remote Sensing**, v. 41, n. 6, p. 1174-1179, 2003.
- CASSETTE, P.; BOCHUD, F.; KEIGHTLEY, J. Example of Monte Carlo uncertainty assessment in the field of radionuclide metrology. **Metrologia**, v. 52, n. 3, p. S42-S50, 2015.

- CHANDER, G.; MEYER, D. J.; HELDER, D. L. Cross calibration of the Landsat-7 ETM+ and EO-1 ALI sensor. **IEEE Transactions on Geoscience and Remote Sensing**, v. 42, n. 12, p. 2821–2831, 2004.
- CHANDER, G.; MARKHAM, B. L.; HELDER, D. L. Summary of current radiometric calibration coefficients for Landsat MSS, TM, ETM+, and EO-1 ALI sensors. **Remote Sensing of Environment**, v.113, n.5, p. 893-903, 2009.
- CHANDER, G.; HELDER, D. L.; AARON, D.; MISHRA, N.; SHRESTHA , A. K. Assessment of spectral, misregistration, and spatial uncertainties inherent in the cross-calibration study. **IEEE Transactions on Geoscience and Remote sensing**, v.51, n.13, p. 1282-1296, 2013a.
- CHANDER, G.; MISHRA, N.; HELDER, D. L.; AARON, D. B.; ANGAL, A; CHOI, T.; XIONG, X.; DOELLING, D. R. Applications of Spectral Band Adjustment Factors (SBAF) for cross-calibration. **IEEE Transactions on Geoscience and Remote sensing**, v.51, n.13, p. 1267-1281, 2013b.
- CHANDER, G.; HEWISON, T.J.; FOX, N.; WU, X.; XIONG, X.; BLACKWELL, W. Overview of intercalibration of satellite instruments. **IEEE Transactions on Geoscience and Remote sensing**, v.51, n.3, p. 1056-1080, 2013c.
- CHEN, H. S. **Remote sensing calibration systems: an introduction**. Hampton, Virginia, USA: A. Deepak Publishing, 1997. 238 p.
- CHEN, W.; ZHAO, H.; LI, Z.; JING, X.; YAN, L. uncertainty evaluation of an in-flight absolute radiometric calibration using a statistical Monte Carlo Method. **IEEE Transactions on Geoscience and Remote Sensing**, v. 53, n. 5, p. 2925-2924, 2015.
- COMMITTEE ON EARTH OBSERVATION SATELLITES (CEOS) WORKING GROUP ON CALIBRATION AND VALIDATION (WGCV). 2016. Available: <<http://ceos.org/ourwork/workinggroups/wgcv/>>. Access: 10 may 2016.
- COSNEFROY, H.; LEROY, M.; BRIOTTET, X. Selection and characterization of Saharan and Arabian Desert sites for the calibration of optical satellite sensors. **Remote Sensing of Environment**, v. 58, p.101-114, 1996.
- CZAPLA-MYERS, J.; MCCORKEL, J.; ANDERSON, N.; THOME, K.; BIGGAR, S.; HELDER, D.; AARON, D.; LEIGH, L.; MISHRA, N. The ground-based absolute radiometric calibration of Landsat 8 OLI, **Remote Sensing**, v. 7, n. 1, p. 600-626, 2015.
- DINGUIRARD, M.; SLATER, P. N. Calibration of space-multispectral imaging sensors: a review. **Remote Sensing of Environment**, v.68, n.3, p.194-205, 1999.
- DROSG, M. **Dealing with uncertainties: a guide to error analysis**. Wien, Austria: Springer, 2007. 190 p.

DUAN, Y.; YAN, L.; YANG, B.; JING, X; CHEN, W. Outdoor relative radiometric calibration method using gray scale targets. **Science China Technological Sciences**, v. 56, n. 7, p. 1825-1834, 2013.

ECHER, E.; SOUZA, M. P.; SCHUCH, N. J. A lei de Beer aplicada na atmosfera terrestre. **Revista Brasileira de Ensino de Física**, v. 23, n. 3, p. 276-283, 2001.

EHSANI, A. R.; REAGAN, J. A.; ERXLEBEN, W. H. Design and performance analysis of an automated 10-channel solar radiometer instrument. **Journal of Atmospheric and Oceanic Technology**, v. 15, n. 3, p. 697-707, 1998.

EPIPHANIO, J. C. N. CBERS: Estado atual e futuro. In: SIMPOSIO BRASILEIRO DE SENSORIAMENTO REMOTO, 2009, Natal, RN. **Anais...** São José dos Campos: INPE, 2009. p. 2001-2008. Available: <<http://marte.sid.inpe.br/col/dpi.inpe.br/sbsr@80/2008/11.18.12.46/doc/2001-2008.pdf>>. Access: 10 may 2016.

EPIPHANIO, J. C. N. CBERS-3/4: características e potencialidades. In: SIMPOSIO BRASILEIRO DE SENSORIAMENTO REMOTO, 15. (SBSR), 2011, Curitiba. **Anais...** São José dos Campos: INPE, 2011. p. 9009-9016. DVD, Internet. ISBN 978-85-17-00056-0 (Internet), 978-85-17-00057-7 (DVD). Available: <<http://urlib.net/3ERPFQRTRW/3A4A6C5>>. Access: 10 may 2016.

FONSECA, L. M. G.; EPIPHANIO, J. C. N.; VALERIANO, D. M.; SOARES, J. V.; D'ALGE, J. C. L.; SANTOS, M. A. Earth observation applications in Brazil with focus on the CBERS program. **IEEE Geoscience and Remote Sensing Magazine**, v. June, 2014. doi: <2168-6831/14©2014IEEE>.

FOX, N. QA4EO - Quality assurance framework for earth observation. Group on *Earth Observations (GEO)*. **A guide to expression of uncertainty of measurements**. QA4EO-QAEO-GEN-DQK-006, 2010. 11 p. Available: <http://qa4eo.org/docs/QA4EO-QAEO-GEN-DQK-006_v4.0.pdf>. Access: 10 may 2016.

GRO, S.; ESSELBORN, M.; WIRTH, M.; FIX, A.; MINIKIN, A. Airborne high spectral resolution lidar observation of pollution aerosol during EUCAARI-LONGREX. **Atmospheric Chemistry and Physics**, v. 13, n. 5, p. 2435-2444, 2013.

HALTHORE, R.N.; ECK, T.F.; HOLBEN B.N.; MARKHAM, B.L. Sun photometric measurements of atmospheric water vapor column abundance in the 940-nm band. **Journal of Geophysical Research**, v. 102, n. D4, p. 4343-4352, 1997.

HELDER, D. L.; MARKHAM, B. L.; THOME, K. J.; BARSÍ, J. A., CHANDER, G.; MALLA, R. Updated radiometric calibration for the Landsat-5 Thematic Mapper Reflective Bands. **IEEE Transactions on Geoscience and Remote Sensing**, v. 46, n. 10, p. 3309-3325, 2008.

HELDER, D. L.; BIKASH, B.; DANIEL, L. M. Optimized identification of worldwide radiometric pseudo-invariant calibration sites. **Canadian Journal of Remote Sensing**, v. 36, n.5, p.527-539, 2010.

HELDER, D. L.; THOME, K.; AARON, D.; LEIGH, L.; CZAPLA-MYERS, J.; LEISSO, N.; BIGGAR, S.; ANDERSON, N. Recent surface reflectance measurement campaigns with emphasis on best practices, SI traceability and uncertainty estimation, **Metrologia**, v. 49, n.2, p. S21-S28, 2012.

HELDER, D.; THOME, K. J.; MISHRA, N.; CHANDER, G.; XIONG, X.; ANGAL, A.; CHOI, T. Absolute radiometric calibration of Landsat using a pseudo invariant calibration site. **IEEE Transactions on Geoscience and Remote Sensing**, v. 51, v. 3, p. 1360-1369, 2013.

HELENE, O. A. M.; VANIN, V.R. **Tratamento estatístico de dados: em física experimental**. São Paulo: Edgard Blücher, 1981. 105 p.

HÖPE, A.; HAUER, K. O. Three-dimensional appearance characterization of diffuse standard reflection materials. **Metrologia**, v. 47, n.3, p. 295-304, 2010.

HOUSTON J.; HARTLEY, A. J. The central Andean west-slope rainshadow and its potential contribution to the origin of hyper-aridity in the Atacama Desert, **International Journal of Climatology**, v. 23, n.12, p. 1453-1464, 2003.

IENILUCCI, E. J. **Using MODTRAN predicting sensor-reaching radiance**. Chester F. Carlson Center for Imaging Science and Rochester Institute of Technology, 2007, 10 p. Available: <https://www.cis.rit.edu/class/simg762/Modtran_lab.pdf>. Access: 10 may 2016.

INSTITUTO NACIONAL DE METEOROLOGIA (INMET). **Monitoramento das estações automáticas**. 2016. Available: <<http://www.inmet.gov.br/sonabra/maps/automaticas.php>>. Access: 10 may 2016.

INSTITUTO NACIONAL DE PESQUISAS ESPACIAIS (INPE). **Catálogo CBERS-4**. São José dos Campos, 2016. Catálogo. Available: <<http://www2.dgi.inpe.br/CDSR>>. Access: 10 may 2016.

IRONS, J. R.; DWYER, J. L.; BARSİ, J. A. The next Landsat satellite: The Landsat data continuity mission. **Remote Sensing of Environment**, v.122, p.11-21, 2012.

JACKSON, R. D.; CLARKE, T.R.; MORAN, M.S. Bidirectional calibration results for 11 spectralon and 16 BaSO₄ reference reflectance panels. **Remote Sensing of Environment**, v. 40, n.3, p.231-239, 1992.

JOINT COMMITTEE FOR GUIDES IN METROLOGY (JCGM). BUREAU INTERNATIONAL DES POIDS ET MESURES (BIPM). **Evaluation of measurement data** — guide to the expression of uncertainty in measurement. JCGM 100:2008. 1. ed. 2008a, 134 p. Available: <http://www.bipm.org/utils/common/documents/jcgm/JCGM_100_2008_E.pdf>. Access: 10 may 2016.

JOINT COMMITTEE FOR GUIDES IN METROLOGY (JCGM). BUREAU INTERNATIONAL DES POIDS ET MESURES (BIPM). **Evaluation of measurement data** – supplement 1 to the “guide to the expression of uncertainty in measurement” – propagation of distributions using a monte carlo method. JCGM 101:2008. 1. ed. 2008b. Available:

<http://www.bipm.org/utils/common/documents/jcgm/JCGM_101_2008_E.pdf>. Access: 10 may 2016.

JENSEN, J. R. **Sensoriamento remoto do ambiente: uma perspectiva em recursos terrestres**. 2. ed. São José dos Campos: Parêntese, 2009. 598 p. Tradução.

LABSPHERE. **USS-2000 integrating sphere manual**. North Sutton, NH, 2005.

LABSPHERE. **Setting the standard in light measurement: product Guide**. 2008. Sutton, New Hampshire, USA.

LABSPHERE. **Calibration certificate**. Sutton, New Hampshire, USA: Labsphere. Serial Number: 99AA04-1112-5237. Date of Calibration: November 13, 2012.

LABSPHERE. **Technical guide: Integrating Sphere Theory and Applications**. North Sutton, New Hampshire, USA: Labsphere. 2016. Available: <<https://www.labsphere.com/site/assets/files/2551/a-guide-to-integrating-sphere-theory-and-applications.pdf>>. Access: 10 may 2016.

LAMPARELLI, R. A. C.; PONZONI, F. J.; ZULLO JR., J.; PELLEGRINO, G. Q.; ARNAUD, Y. Characterization of the salar de uyuni for in-orbit satellite calibration. **IEEE Transactions on Geoscience and Remote Sensing**, v. 41, n. 6, p. 1461-1468, 2003.

MARKHAM, B.L.; BARKER, J.L.; KAITA, E.; BARSİ, J.A.; HELDER, D.L.; PALLUCONI, F.D.; SCHOTT, J.R.; THOME, K.J.; MORFITT, R.; SCARAMUZZA, P. Landsat-7 ETM+ Radiometric calibration: two years on-orbit. In: **IEEE INTERNATIONAL GEOSCIENCE AND REMOTE SENSING SYMPOSIUM, (IGARSS)**, 2001, Sydney, Australia. **Proceedings...** Piscataway, New Jersey, USA: IEEE Publications, 2001, p. 518-520.

MARKHAM, B.; THOME, K. J.; BARSİ, J. A.; KAITA, E.; HELDER, D. L.; BARKER, J. L. ; SCARAMUZZA, P. L. Landsat-7 ETM+ on-orbit reflective-band radiometric stability and absolute calibration, **IEEE Transactions on Geoscience and Remote Sensing**, v. 42, n. 12, p. 2810-2820, 2004.

MARKHAM, B. L.; HAQUE, MD. O.; BARSİ, J. A.; MICIJEVIC, E.; HELDER, D. L.; THOME, K. J.; AARON, D.; CZAPLA-MYERS, J. S. Landsat-7 ETM+: 12 Years On-Orbit Reflective-Band Radiometric Performance. **IEEE Transactions on Geoscience and Remote Sensing**, v. 50, n. 5, p. 2056-2062, 2012.

MARKHAM, B. L.; HELDER, D. L. Forty-year calibrated record of earth-reflected radiance from Landsat: a review. **Remote Sensing of Environment**, v. 122, p. 30-40, 2012.

MCCORKEL, J.; THOME, K.; ONG, L. Vicarious calibration of EO-1 HYPERION 2013. **IEEE Journal of Selected Topics in Applied Earth Observations and Remote Sensing**, v. 6, n. 2, p. 400-4007, 2013.

MENDES, A.; ROSÁRIO, P. P. **Metrologia e incerteza de medição**. São Paulo, SP: Editora EPSE, 2005. 128 p.

MILTON, E.J. Principles of field spectroscopy. **International Journal of Remote Sensing**, v. 8, n.12, p.1807-1827, 1987.

MISHRA, N.; HAQUE, M. O.; LEIGH, L.; AARON, D.; HELDER, D.; MARKHAM, B. Radiometric cross calibration of Landsat 8 Operational Land Imager (OLI) and Landsat 7 Enhanced Thematic Mapper Plus (ETM+). **Remote Sensing**, v. 6, n. 12, p. 12619-12638, 2014a.

MISHRA, N.; HELDER, D. L.; ANGAL, A.; CHOI, J.; XIONG, X. Absolute calibration of optical satellite sensors using libya 4 pseudo invariant calibration site. **Remote Sensing**, v. 6, n. 2, p. 1327-1346, 2014b.

NATIONAL WEATHER SERVICE (NWS). **National Oceanic and Atmospheric Administration**. 2016. Available: <<http://www.weather.gov/>>. Access: 10 may 2016.

OSTERWALD, C. R; EMERY, K. A. Spectroradiometric sun photometry. **Journal of Atmospheric and Oceanic Technology**, v. 17, n. 9, p.1171-1188, 2000.

PINTO, C. T.; SILVA, M. L.; MELO, M. C.; ANDRADE, L. L.; CASTRO, R. M. Caracterização espectral parcial do sensor SISIMI. In: SIMPÓSIO BRASILEIRO DE SENSORIAMENTO REMOTO, 14. (SBSR), 2009, Natal. **Anais...** São José dos Campos: INPE, 2009. p. 7639-7646. DVD, On-line. ISBN 978-85-17-00044-7. Available: <<http://urlib.net/dpi.inpe.br/sbsr@80/2008/11.17.18.32>>. Access: 10 may 2016.

PINTO, C. T. **Avaliação das incertezas na caracterização de superfícies de referência para calibração absoluta de sensores eletroópticos**. 2011. 167 p. (sid.inpe.br/mtcm19/2011/03.30.18.09-TDI). Dissertação (Mestrado em Sensoriamento Remoto) - Instituto Nacional de Pesquisas Espaciais, São Jose dos Campos, 2011. Available: <<http://urlib.net/8JMKD3MGP7W/39E3LH2>>. Access: 10 may 2016.

PINTO, C.T; PONZONI, F. J.; CASTRO, R. M.; GRIFFITH, D. J. Spectral uniformity evaluation of reference surfaces for airborne and orbital sensors absolute calibration. **Brazilian Journal of Geophysics**, v.30, n.3, p.263-275, 2012.

PINTO, C. T.; PONZONI, F. J.; CASTRO, R. M. **Calibração cruzada de sensores de observação da terra**. São José dos Campos: INPE, 2013a. 29 p. (sid.inpe.br/mtcm19/2013/08.13.15.47-RPQ). Available: <<http://urlib.net/8JMKD3MGP7W/3EL22DE>>. Access: 10 may 2016.

PINTO, C. T.; PONZONI, F. J.; FONSECA, L. M. G.; CASTRO, R. M. Simulação de Monte Carlo na avaliação das incertezas em parte do processo de calibração de sensores. In: SIMPÓSIO BRASILEIRO DE SENSORIAMENTO REMOTO, 16.

(SBSR), 2013b, Foz do Iguaçu. **Anais...** São José dos Campos: INPE, 2013b. p. 9131-9137. DVD, Internet. ISBN 978-85-17-00066-9 (Internet), 978-85-17-00065-2 (DVD). Available: <<http://urlib.net/3ERPFQRTRW34M/3E7GD3T>>. Access: 10 may 2016.

PINTO, C. T.; PONZONI, F. J.; BARRIENTOS, C.; MATTAR, C.; SANTAMARÍA-ARTIGAS, A.; CASTRO, R. M. Spectral and atmospheric characterization of a site at Atacama Desert for Earth observation sensors calibration, **IEEE Geoscience and Remote Sensing Letters**, v. 12, n. 11, p. 2227-2231, 2015.

PINTO, C. T.; PONZONI, F. J.; CASTRO, R. M.; LEIGH, L. ; MISHRA, N.; AARON, D.; HELDER, D. First in-flight radiometric calibration of MUX and WFI on-Board CBERS-4. **Remote Sensing**, v.8, n.5, p. 1-22, 2016a.

PINTO, C. T.; PONZONI, F. J.; CASTRO, R. M.; LEIGH, L.; KAEWMANEE, M.; AARON, D.; HELDER, D. Evaluation of the uncertainty in the Spectral Band Adjustment Factor (SBAF) for cross-calibration using Monte Carlo simulation. **Remote Sensing Letters**, v. 7, n. 9, p. 837-846, 2016b.

PONZONI, F. J.; ZULLO JR., J.; LAMPARELLI, R. A. C. In-flight absolute calibration of the CBERS-2 IRMSS sensor data. **International Journal of Remote Sensing**, v. 27, n. 4, p. 799-804, 2006.

PONZONI, F. J.; ZULLO JUNIOR, J.; LAMPARELLI, R. A. C. In-flight absolute calibration of the CBERS-2 CCD sensor data. **Anais da Academia Brasileira de Ciências**, v. 80, n. 2, p. 373-380, 2008. Available: <<http://urlib.net/sid.inpe.br/mtc-m17@80/2008/06.03.18.31>>. Access: 10 may 2016.

PONZONI, F. J.; PINTO, C. T.; LAMPARELLI, R. A. C.; ZULLO J.R, J.; ANTUNES, M. A. H. **Calibração de sensores orbitais**. 2 ed. São José dos Campos: Parêntese, 2015. v. 1, 64 p. ISBN 978-85-60507-01-6.

RED AGROCLIMÁTICA NACIONAL, AGROMET. 2016. Available: <<http://agromet.inia.cl/>>. Access: 10 may 2016.

RICHARDS, J. A. **Remote sensing digital image analysis: an introduction**. 5. ed. Springer-Verlag. Berlin Heidelberg, 2013, 494 p. ISBN 978-3-642-30061-5.

ROLLIN, E. M. **An introduction to the use of sun-photometer for the atmospheric correction of airborne sensor data**, 2000. Available: <<http://www.ncaveo.ac.uk/site-resources/pdf/cimel.pdf>>. Access: 10 may 2016.

ROY, D.P.; WULDER, M.A.; LOVELAND, T.R.; WOODCOCK , C.E.; ALLEN, R.G.; ANDERSON, M.C.; HELDER, D.; IRONS,J.R.; JOHNSON, D.M.; KENNEDY, R.; SCAMBOS , T.A.; SCHAAF, C.B.; SCHOTT , J.R.; SHENG ,Y.; VERMOTE , E.F.; BELWARD,A.S.; BINDSCHADLER, R.; COHEN,W.B.; GAO, F.; HIPPLE, J.D.; HOSTERT,P.; HUNTINGTON , J.; JUSTICE , C.O.; KILIC, A.; KOVALSKYY, V.; LEE, Z.P.; LYMBURNER , L.; MASEK, J.G.; MCCORKEL, J.; SHUAI, Y.; TREZZA, R.; VOGELMANN,J.; WYNNE, R.H.; ZHU, Z. Landsat-8: science and

product vision for terrestrial global change research. **Remote Sensing of Environment**, v. 145, n.5, p. 154-172, 2014.

SCHMID, B.; WEHRLI, C. Comparison of Sun photometer calibration by use of the Langley technique and the standard lamp. **Applied Optics**, v. 34, n.21, p. 4500-4512, 1995.

SCOTT, K. P.; THOME, K. J.; BRONWLEE, M. R. Evaluation of the Railroad Valley Playa for use in vicarious calibration. **Proceedings of SPIE Conference**, v.2818, p.158-166, 1996.

SCHAEPMAN-STRUB, G.; SCHAPMAN, M.E.; PAINTER, T.H.; DANGEL, S.; MARTONCHIK, J. V. Reflectance quantities in optical remote sensing – definitions and case studies. **Remote Sensing of Environment**, v.103, n.1, p. 27-42, 2006.

SLATER, P.N.; BIGGAR, S.F.; HOLM, R.G.; JACKSON, R.D.; MAO, Y.; MORAN, M.S.; PALMER, J.M.; YUAN, B. Reflectance-and radiance-based methods for the in-flight absolute calibration of multispectral sensors. **Remote Sensing of Environment**, v.22, n.1, p.11-37, 1987.

TEILLET, P. M.; BARKER, J. L.; MARKHAM, B. L.; IRISH, R. R.; FEDOSEJEVS, G.; STOREY, J. C. Radiometric cross-calibration of the Landsat-7 ETM+ and Landsat-5 TM sensors based on tandem data sets. **Remote Sensing of Environment**, v.78, n.1-2, p.39-54, 2001.

TEILLET, P.M.; MARKHAM, B.L.; IRISH, R. R. Landsat cross-calibration based on near simultaneous imaging of common ground targets. **Remote Sensing of Environment**, v.102, n.3-4, p.264-270, 2006.

TEILLET, P.M.; FEDOSEJEVS, G.; THOME, K. J; BARKER, J. L. Impacts of spectral band difference effects on radiometric cross-calibration between satellite sensors in the solar-reflective spectral domain. **Remote Sensing of Environment**, v. 110, n.3, p.393-409, 2007.

THOME, K. J.; MARKHAM, B.L.; BARKER, J.L.; SLATER, P.N.; BIGGAR, S. F. Radiometric calibration of Landsat. **Photogrammetric Engineering and Remote Sensing**, v.63, n.7, p.853-858, 1997.

THOME, K.; ARAI, K.; HOOK, S.; KIEFFER, H.; LANG, H.; MATSUNAGA, T.; ONO, A.; PALLUCONI, F.; SAKUMA, H.; SLATER, P.; TAKASHIMA, T.; TONOOKA, H.; TSUCHIDA, S.; WELCH, R. M.; ZALEWSKI, E. ASTER Preflight and inflight calibration and the validation of level 2 products. **IEEE Transactions on Geoscience and Remote Sensing**, v. 36, n. 4, p. 1161-1172, 1998.

THOME, K. J. Absolute radiometric calibration of Landsat-7 ETM+ using the reflectance-based method. **Remote Sensing of Environment**, v. 78, n.1-2, p.27-38, 2001.

THOME, K. J.; BIGGAR, S. F.; WISNIEWSKI, W. Cross comparison of EO-1 sensors and other earth resources sensors to Landsat-7 ETM+ Using Railroad Valley Playa.

IEEE Transactions on Geoscience and Remote sensing, v.41, n.6, p. 1180-1188, 2003.

THOME, K. J.; HELDER, D. L.; AARON, D.; DEWALD, J. D. Landsat-5 TM and Landsat-7 ETM+ absolute radiometric calibration using the reflectance-based method. **IEEE Transactions on Geoscience and Remote sensing**, v.42, n.12, p. 2777–2785, 2004.

THOME, K. J.; ARAI, K.; TSUCHIDA, S.; BIGGAR S. F. Vicarious calibration of ASTER via the reflectance-based approach. **IEEE Transactions on Geoscience and Remote Sensing**, v. 46, n. 10, p. 3285-3295, 2008.

UNGAR, S. G.; MIDDLETON, E. M.; ONG, L.; CAMPBELL, P.K.E. EO -1 Hyperion onboard performance over eight years: Hyperion calibration. In: EUROPEAN ASSOCIATION OF REMOTE SENSING LABORATORIES SIG IS WORKSHOP (EARSeL), 6., 2009, Tel-Aviv, Israel. **Proceedings...** Tel-Aviv: Tel- Aviv University, 2009. p. 1-6.

VERMOTE, E. F.; TANRE, D.; DEUZÉ, J. L.; HERMAN, M.; MORCRETTE, J. Second simulation of the satellite signal in the solar spectrum, 6S: an overview. **IEEE Transactions on Geoscience and Remote Sensing**, v. 35, n. 3, p. 675-686,1997.

VERMOTE, E.; TANRÉ, D.; DEUZÉ, J. L.; HERMAN, M.; MORCRETTE, J. J.; KOTCHENOVA, S. Y. **Second simulation of a satellite signal in the solar spectrum - Vector (6SV)**. 6S user guide version 3, 2006. Available: <http://6s.ltdri.org/files/tutorial/6S_Manual_Part_1.pdf>. Access: 10 may 2016.

VESILIND, P. J. the driest place on Earth. **National Geographic**, v. 204, n.2, p.46-71, 2003.

VUOLO, J. H. **Fundamentos da teoria de Erros**. São Paulo: Edgard Blücher, 1996, 2 ed, 249 p.

XIONG, X.; SUN, J.; BARNES, W.; SALOMONSON, V.; ESPOSITO, J.; ERIVES, H.; GUENTHER, B. Multiyear on-orbit calibration and performance of Terra MODIS reflective solar bands. **IEEE Transactions on Geoscience and Remote Sensing**, v. 45, n. 4, p. 879-889, 2007.

YULIANG, Q.; SHANGMIN, Z.; ZHEN, L.; BEI, J. Application of China–Brazil Earth resources satellite in China. **Advances in Space Research**, v. 43, n. 6, p. 917-922, 2009.

ZULLO JUNIOR, J.; GU, X.; GUYOT, G.; PINTO, H. S.; HAMADA, E.; ALMEIDA, C. A. S.; PELLEGRINO, G. Q. Estimativa do conteúdo de vapor d'água a partir da radiação solar direta. In: SIMPÓSIO BRASILEIRO DE SENSORIAMENTO REMOTO, 8. (SBSR), 1996, Salvador. **Anais...** São José dos Campos: INPE, 1996. p. 979-980. CD-ROM. ISBN 85-17-00014-5. Available: <<http://urlib.net/sid.inpe.br/deise/1999/02.02.11.32>>. Access: 10 may 2016.